PHASE BEHAVIOR OF DIBLOCK COPOLYMER IN THIN FILMS AND MEMBRANES

Dissertation
zur Erlangung des Grades
„Doktor der Naturwissenschaften“
am Fachbereich Physik, Mathematik und Informatik
der Johannes Gutenberg-Universität Mainz

GIANG THI VU

born in Nam Dinh, Vietnam

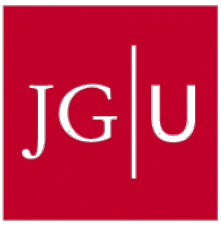

JOHANNES GUTENBERG UNIVERSITÄT MAINZ

Mainz, 15.08.2018

PUBLICATIONS

Some parts of this thesis have appeared in the following:

- A. A. Abate, G. T. Vu, A. D. Pezzutti, N. A. García, R. L. Davis, F. Schmid, R. A. Register, D. A. Vega. Shear-aligned block copolymer monolayers as seeds to control the orientational order in cylinder-forming block copolymer thin films, *Macromolecules*, **49**, 7588 - 7596 (2016).
- G. T. Vu, A. A. Abate, L. R. Gómez, A. D. Pezzutti, R. A. Register, D. A. Vega, F. Schmid. Curvature as a guiding field for patterns in thin block copolymer films, *Phys. Rev. Lett.*, **121**, 087801 (2018).
- A. A. Abate, G. T. Vu, M. Piqueras, L. R. Gómez, M. C. del Barrio, F. Schmid, D. A. Vega. Block copolymer thin film instabilities induced by supercritical carbon dioxide, **preparing** (2018).

ABSTRACT

Thin films of block copolymers have attracted intensive research interest because these materials can self-assemble into a variety of well-ordered nanostructures. These systems have been employed in numerous applications in nanotechnology, including photonic crystals, magnetic storage media, etc.. However, one of the problems with self-assembled block copolymers is the lack of long-range order due to the presence of topological defects.

In this thesis, we perform a theoretical study to investigate the morphologies in thin diblock copolymer films using self-consistent field theory (SCFT). We focus on the stability and orientation of the cylindrical phase formed by AB diblock copolymers when confined within substrates of different geometries.

Firstly, we apply the SCFT method to study AB diblock copolymers confined between two planar surfaces. We determine minima in the free energy landscape and the optimum thickness of multilayer cylindrical films to analyze the stability of films. For the thin film systems investigated in this work, we show that the global equilibrium state of these films is the one where a monolayer film coexists with the islands of thicker multilayer films. Additionally, the coupling mechanism between the bottom and upper layers is investigated as well. We show that the first aligned layer can help to order the upper layers, and then to propagate order in thicker thin films.

In general, when the surface fields attract the majority block sufficiently strongly, the cylindrical phase formed by the diblock copolymers will orient parallel to the film plane ($C_{||}$). However, their orientation can switch to perpendicular ($C_{\perp}$) or new morphologies can be found under certain conditions. Our SCFT results indicate that there is an orientational phase transition, $C_{||} \rightarrow C_{\perp}$, when the film thickness is reduced below the natural size of the monolayer of parallel cylinders. Furthermore, we also find the formation of the perforated lamellae (PL) and lamella (L) phases in the region in which the thickness is about half the optimal thickness of a single layer of parallel cylinders. When the thickness is very small, the films become unstable and dewet from the substrate.

We also study the diblock copolymers confined in curved substrate (coaxial cylindrical surfaces). We consider two types of model systems: free-standing membranes and curved supported thin films. We calculate the bending constant of the free-standing membranes. The results imply that the local orientation of patterns has a strong coupling with the geometry of confinement. Namely, the block copolymer cylinders tend to align along the direction of curvature at high curvatures. Moreover, at low curvatures, there is a transition $C_{\perp} \rightarrow C_{||}$ in supported films, which is absent in the free-standing membranes. Therefore, the mean curvature not only acts as a guiding field to produce well ordered patterns but also generates defects at specific regions in space. The stability of the thin films against curvature-induced dewetting is also analyzed.

ZUSAMMENFASSUNG

Dünne Schichten aus Blockcopolymeren haben ein intensives Forschungsinteresse geweckt, da sich diese Materialien zu einer Vielzahl von geordneten Nanostrukturen zusammenfügen können. Diese Systeme wurden in zahlreichen Anwendungen in der Nanotechnologie, darunter photonische Kristalle, magnetische Speichermedien, etc. eingesetzt. Eines der Probleme bei selbst zusammengesetzten Blockcopolymeren ist jedoch das Fehlen einer langreichweitigen Ordnung aufgrund von topologischen Defekten.

In dieser Arbeit führen wir eine theoretische Studie zur Untersuchung der Morphologien in dünnen Diblockcopolymer-Filmen mithilfe der Self-Consistent Field Theory (SCFT) durch. Wir konzentrieren uns auf die Stabilität und Orientierung der zylindrischen Phase, die durch AB-Diblockcopolymere gebildet wird, wenn sie zwischen Substraten mit unterschiedlichen Geometrien eingeschlossen wird.

Zuerst wenden wir die SCFT-Methode an, um AB-Diblockcopolymere zu untersuchen, die zwischen zwei planaren Oberflächen eingeschlossen sind. Wir bestimmen die Minima in der freien Energielandschaft und die optimale Dicke von mehrschichtigen zylindrischen Filmen, um die Stabilität von Filmen zu analysieren. Für die in dieser Arbeit betrachteten Systeme aus dünnen Schichten zeigen wir, dass der Zustand des globalen Gleichgewichts derjenige ist, bei dem eine einzelne Monoschicht mit Inseln dickerer Multischichten koexistiert. Des Weiteren wird auch der Kopplungsmechanismus zwischen der untersten Schicht und oberen Schichten beleuchtet. Wir zeigen, dass die erste orientierte Schicht helfen kann, die oberen Schichten zu ordnen und dann die Ordnung in dickeren Dünnschichten zu propagieren.

Wenn die Oberflächenfelder den Mehrheitsblock ausreichend stark anziehen, orientiert sich die von den Diblockcopolymeren gebildete zylindrische Phase parallel zur Filmebene ($C_{||}$). Unter bestimmten Bedingungen kann ihre Orientierung jedoch auf eine senkrechte Orientierung ($C_{\perp}$) wechseln oder es kann eine neue Morphologie gebildet werden. Unsere SCFT-Ergebnisse deuten darauf hin, dass es einen Orientierungsphasenübergang von $C_{||} \rightarrow C_{\perp}$ gibt, wenn die Filmdicke unter die natürliche Größe der Monoschicht der parallelen Zylinder reduziert wird. Darüber hinaus beobachten wir auch die Bildung der perforierten Lamellen (PL) und Lamellen (L) in dem Bereich, in dem die Dicke etwa die Hälfte der optimalen Dicke einer einzelnen Schicht von parallelen Zylindern beträgt. Bei sehr geringer Dicke werden die Filme instabil und entnetzen vom Substrat.

Weiterhin untersuchen wir Diblockcopolymere, welche in gekrümmten Substraten bestehend aus koaxialen zylindrischen Oberflächen eingeschlossen werden. Wir betrachten zwei Arten von Modellsystemen: freistehende Membranen und gebogene, gestützte dünne Schichten. Wir berechnen die Biegekonstante der freistehenden Membranen. Die Ergebnisse deuten darauf hin, dass die lokale Orientierung der Pattern eine starke Kopplung mit der Geometrie des

Confinements hat. Die Blockcopolymer-Zylinder orientieren sich nämlich bei hohen Krümmungen entlang der Krümmungsrichtung. Außerdem gibt es bei niedrigen Krümmungen einen Übergang $C_{\perp} \rightarrow C_{||}$ in gestützten Filmen, der in den freistehenden Membranen nicht auftritt. Die mittlere Krümmung dient daher nicht nur als leitendes Feld zur Erzeugung geordneter Pattern, sondern erzeugt auch Defekte an bestimmten Stellen im Raum. Die Stabilität der dünnen Filme gegen krümmungsinduzierte Entnetzung wird ebenfalls analysiert.

CONTENTS

Part I

INTRODUCTION AND THEORY

1 INTRODUCTION

Many soft materials, such as polymers, colloids and membranes self-assemble into well-defined periodic nanostructures [1]. The self-assembly of complex materials attracts tremendous interest, not only because of the intriguing morphologies they form but also because of their importance in material industry and biological applications. Self-assembly satisfies the key requirement of many technologies. It is a typically low cost, fast and efficient method in nanofabrication [1–4]. Among a wide variety of self-assembling materials, block copolymer thin films provide an excellent alternative because they can be synthesized with different architectures to produce patterns with a diversity of symmetries [5]. More importantly, they can create high resolution patterns on small length scales, for example sub-100 nm, while the limit of traditional optical lithographic techniques is 100 nm [6].

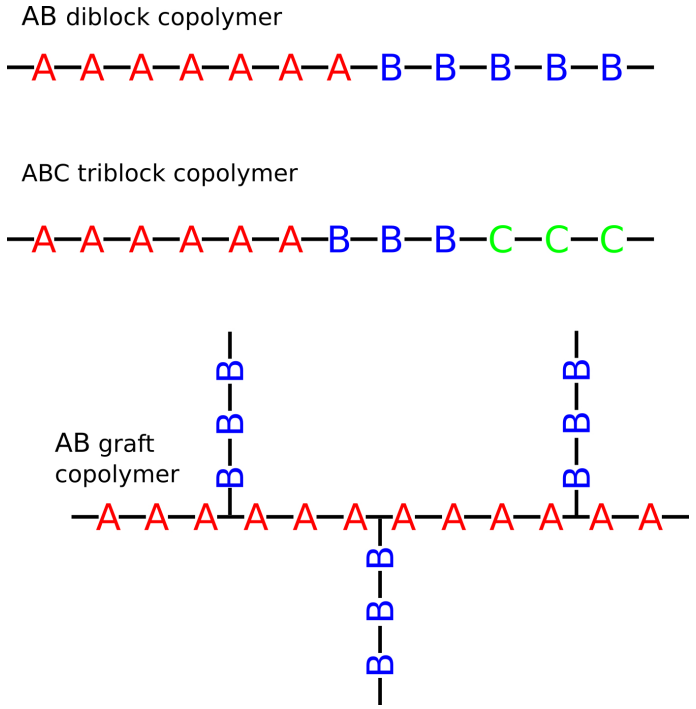

Figure 1.1: Examples of some common copolymer architectures

Block copolymers are made of two or more polymeric blocks. Each block is a sequence of identical monomers which are attached by covalent bonds [7–9]. The number of monomers in one chain is often called the degree of polymerization. It can be small, such as about 300 monomers, a typical number of amino acids in a protein, or very large as polystyrene containing $\sim 10^5$ monomers [10]. The simplest form of a block copolymer is a diblock, in which two sequential species (simply denoted as A and B) occupy a given fraction of a single backbone. Block copolymers can have more intricate and complex archi-

tectures, such as ABC triblock copolymer, graft copolymers or even ABABA pentablock architectures. Figure 1.1 depicts some common copolymer architectures.

During the last decades, it has been found that at a low enough temperature, the incompatibility between different blocks leads to microphase separation. In this case, the copolymer self-assembles into an ordered morphology. For example, lamellae, hexagonally packed cylinders, body centered cubic arrays of spheres, and gyroid phases have been observed in AB diblock copolymers. The symmetry of these phases is mainly controlled by the volume fraction f of one of the blocks, as shown in figure 1.2. In addition to these typical four microphase structures, many more ordered phases with more complex polymer architectures have been seen [5]. The extraordinary variety of possible morphologies and their molecular size $(5-10\,\mathrm{nm})$ make block copolymers an ideal material to produce self-assembled nanostructures. Block copolymers form periodic microdomain structures that can be used as nanolithographic etch masks to produce dot or stripe patterns [7, 11, 12]. There are many applications of block copolymer self-assembly, including the creation of nanopore arrays [13], nanowire polarizer grids [14, 15], high-density magnetic storage devices [16], nanoporous materials as a template to incorporate nanoparticles [17] or biomolecules [18, 19], etc..

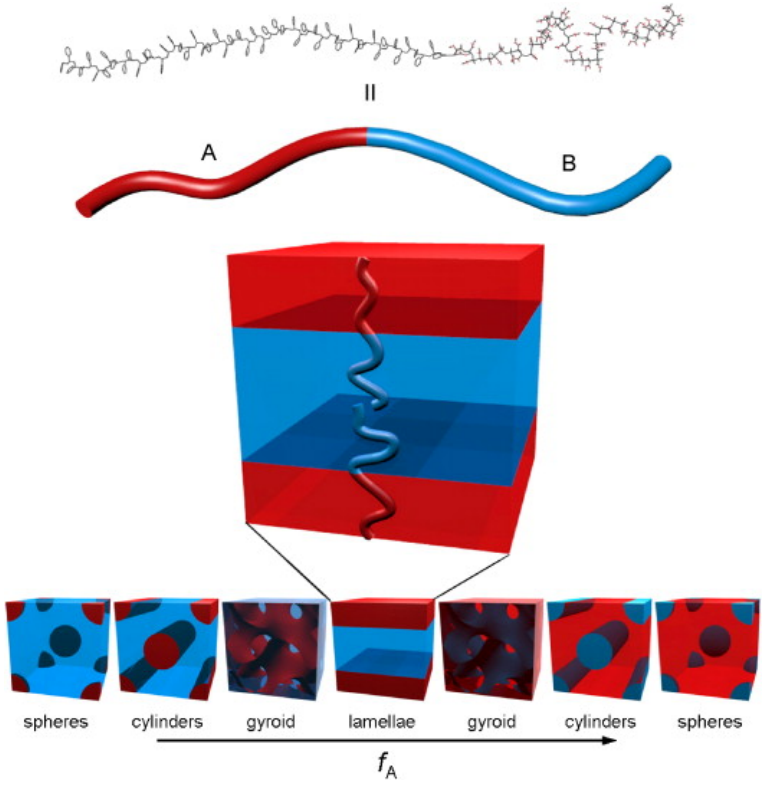

Figure 1.2: Schematics of thermodynamicically stable AB diblock copolymer phases as a function of increasing diblock fraction f_A [9].

There are many studies, both in experiment and in theory, that describe the self-assembly of block copolymers. One of the theoretical methods, the so-called self-consistent field theory, is one of the most successful theories for modelling soft condensed matter systems in general [20] and describing the equilibrium structures of block copolymers in particular [21–24]. For instance, it has been found that the phase diagram for a diblock copolymer (figures 1.3 and 1.4) depends on the volume fraction f of one block and χN, where N is the degree of polymerization and χ is the Flory-Huggins interaction parameter describing the segregation strength between the blocks.

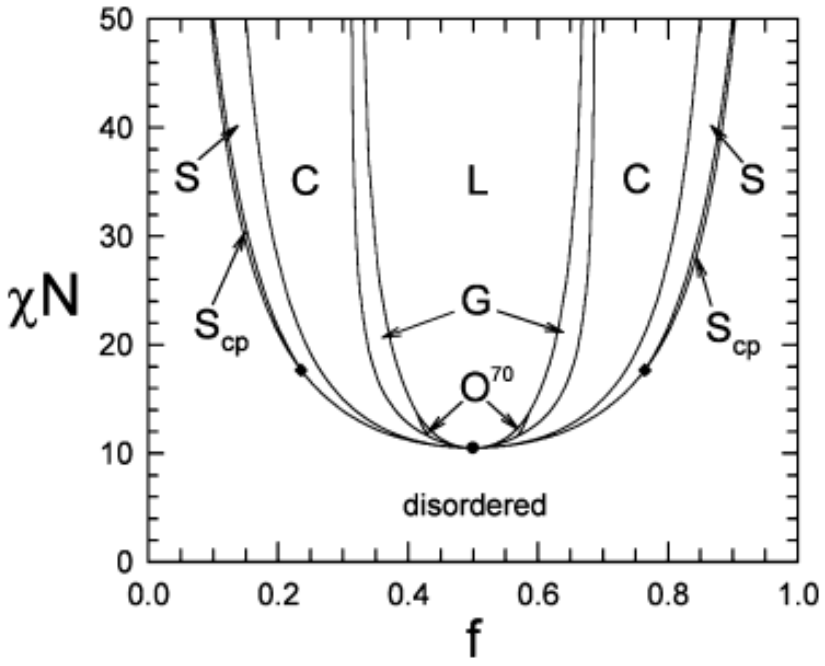

Figure 1.3: Theoretical equilibrium phase diagram for melts of AB diblock copolymers as a function of the volume fraction f of one block and segregation strength χN [24]. Here L corresponds to the lamellar phase, C corresponds to the cylindrical phase, S to the spherical phase, G corresponds to the gyroid phase, O^{70} denotes the Fddd phase and S_{cp} a phase in which spheres occur on a close-packed lattice.

When block copolymers are confined in a thin film at the nano-scale, their morphologies can significantly deviate from those observed in the bulk [4, 29, 30] due to the confining surfaces and the affinity of each block to the interfaces, or more new and interesting complex structures can appear. In these confined systems, the morphologies are determined by a complex interplay of different factors: surface energy, entropic and enthalpic free energy contributions [31]. The microdomain structure here has to adjust to the interfaces and a given thickness. For example, there are some studies that investigated the cylinder-forming of block copolymer confined in thin film indicating that the equilibrium phase behavior is more complex [32–34]. Besides the cylinderical phase, additional phases, such as perforated lamellae (PL) and lamellae (L) were observed. This phase behavior is controlled by the interplay between the

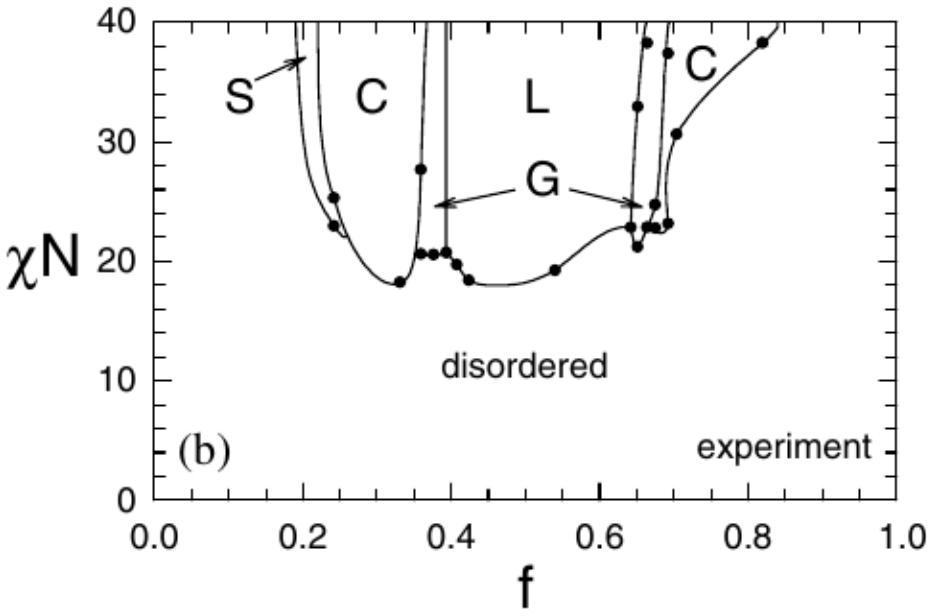

Figure 1.4: Experimental equilibrium phase diagram for melts of polystyrene-polyisoprene diblock copolymers as a function of block fraction f and segregation strength χN [25]. It is analogous to that in figure 1.3, but there are no O^{70} (Fddd) or S_{CP} phases. Most recently, the Fddd phase was observed in an experiment [26, 27]. This figure is adapted from [28].

degree of the preference of surfaces to each block and the mismatch between the film thickness and the periodicity of the microdomain.

The self-assembly of block copolymers has many promising applications. However, one of the main drawbacks of the self-assembly strategy in block copolymer systems is the lack of long-range order due to the presence of defects [35–37]. Figure 1.5 diplays four classical topological defects which are common to various materials including block copolymers. The topological defects, like disclinations, dislocations and grain boundaries disturb the ordered states and consequently prevent applications for devices where order is crucial. In physical systems, these defects appear spontaneously due to a symmetry breaking process [38] and their appearance at the interfaces are unavoidable [6]. In the case of block copolymer thin films developing smectic order. The most common defects are $+1/2$ disclinations and dislocations as shown in figure 1.6. These defects destroy the orientational and/or transitional order.

There has been significant effort to tackle the topological defect problem and to promote long-range order and to produce well-defined periodic structures in block copolymer thin films. For example, it was shown that thin films of cylinder-forming or sphere-forming block copolymers can be well-aligned by using a shearing technique [42–44]. Moreover, other methods such as, graphoepitaxy, electric fields [45–47], curvature of the substrates [41] and zone annealing [48, 49] have been employed to obtain well-defined orientational structures.

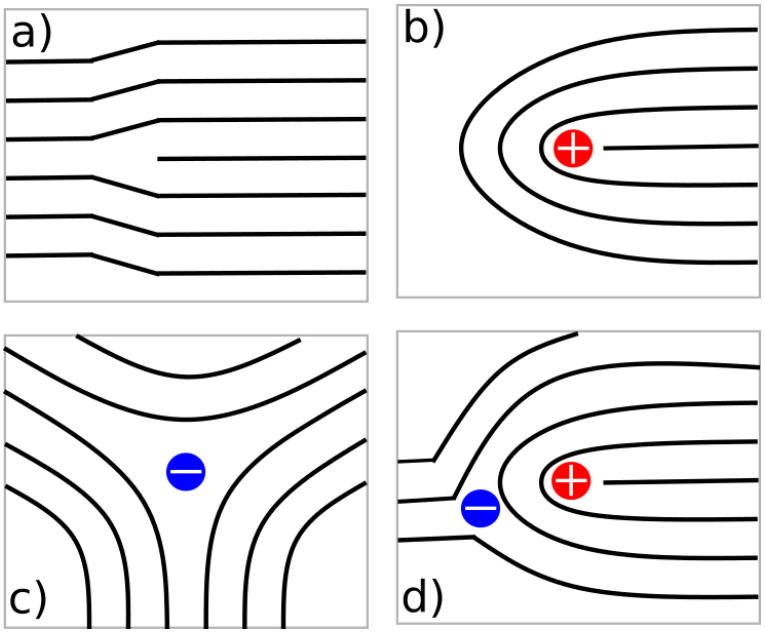

Figure 1.5: Schematic representation of typical topological defect configurations that disrupt order in smectic system. Panel a) shows a edge dislocation which is a less energetic defect. Panel b) and c) are positive and negative 1/2 disclinations, respectively [39, 40]. Panel d) is a paired $\pm 1/2$ disclinations.

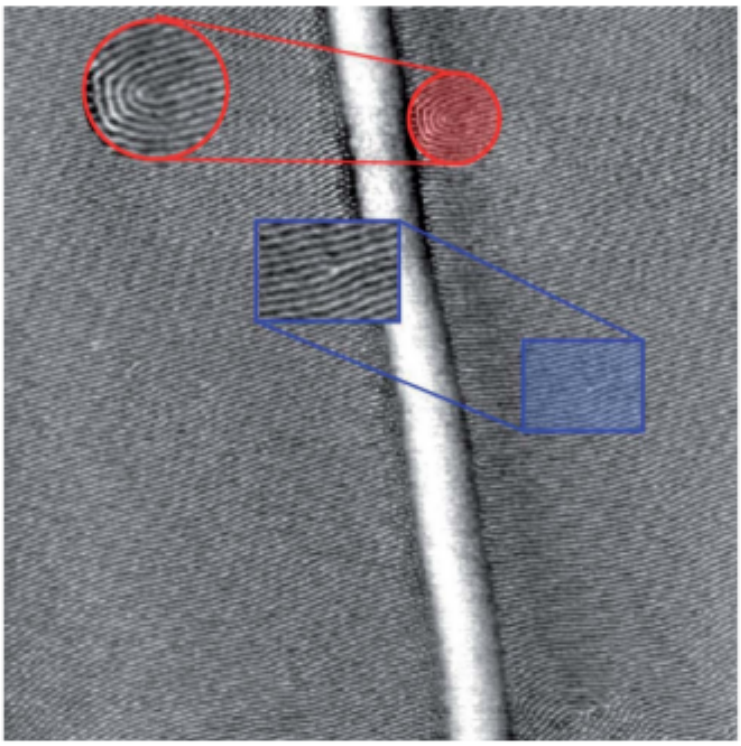

Figure 1.6: Experimental atomic force microscopy (AFM) phase field image of a block copolymer thin film that shows the topological defects: A red circle is a positive disclination, a blue rectangle is a dislocation [41].

This thesis deals with the problem of block copolymers confined in thin film and free-standing membrane systems using self-consistent field theory (SCFT). The systems studied in this thesis are very similar to the experimental systems investigated by Professor Vega's group. In addition to the SCFT free energy, we also consider the contribution of long-range van der Waals (vdW) interaction between the copolymer film and the surfaces to the free energy of the system. The vdW interaction plays an essential role in all phenomena involving intermolecular force, for instance, the wetting or dewetting properties of polymer films. It can stabilize thin PS films against height fluctuations on the substrates [50].

Chapter 2 reviews the theoretical framework of the self-consistent field theory applied to AB diblock copolymer systems. The theory is developed in both the canonical and grand canonical essemble. Chapter 3 presents the approximation and the numerical methods used in this thesis. The central task is to solve the modified diffusion equations. The Crank-Nicolson method is employed here; therefore, it is discussed in detail.

In chapter 4 and 5, we present the results of SCF calculations in Euclidean geometry with periodic boundary conditions of cylinder-forming of diblock copolymers confined between two flat surfaces. Chapter 4 studies multilayers of diblock copolymer in thin films. We investigate the global equilibrium state of thin films and the coupling mechanism between bottom and upper layers. Chapter 5 covers the phase behaviour of cylinder-forming diblock copolymers in thin films due to the mismatch between the natural size of a monolayer of cylinders and the film thickness and the surface fields.

Finally, we extend the method to diblock copolymers confined in thin films with curved substrates (two coaxial cylindrical surfaces) in chapter 6. We investigate how the mean curvature of the substrates influences the local orientation of the copolymer patterns. However, up to now, little is known about the interplay between the block copolymer self-assemply and the curvature. We also analyze the stability of the films against curvature-induced dewetting.

In chapter 7, we summarize the main results of this thesis and give some perspectives in this research area.

2

SELF-CONSISTENT FIELD THEORY

Self-consistent field theory (SCFT) was introduced by Edwards several decades ago [51]. It is one of the most powerful methods to study the self-assembly of complex systems, such as polymer fluids and other soft condensed matter systems in general. It was first extended to block copolymers by Helfand in 1975 [52, 53]. The idea of SCFT is replacing the many-body problem by the problem of an ideal Gaussian chain in an effective mean field potential which is created by the other chains. It is illustrated in figure 2.1. The theory allows exact mean-field calculation for block copolymers and blends using a coarse-grained model. It has been remarkably improved so far with tremendous successes. In the case of block copolymers, SCFT provides a description of a rich variety of phases and a prediction of new morphologies as well. There are several review papers about SCFT [22, 28, 54] with more details. In this chapter, we present a brief introduction into SCFT focusing on block copolymer thin films.

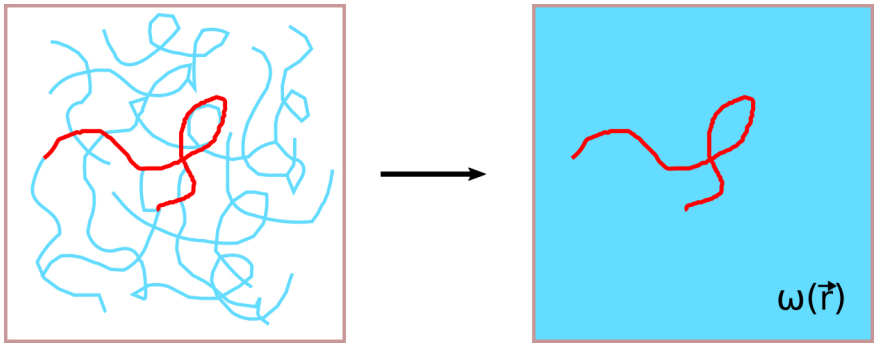

Figure 2.1: An illustration of the mean field approximation. In a system of identical chains, we focus on one chain (the red one), and study the problem of one chain under the influence of the mean field generated by the other chains (right panel). The mean field depends on the local concentration of the monomers.

We consider a melt of n identical AB diblock copolymer molecules confined in a volume V, each consisting of N segments of which a fraction f forms the A block. Then the number of A segments is $N_A = fN$ and for the B segments it is $N_B = (1-f)N$. Here we assume that A and B segments have equal statistical segment length b; however they can have different statistical length in general. Each molecule is parameterized by a variable s which increases continuously from 0 to 1 along its length as shown in figure 2.2. Here s represents a parameterization of the polymer chain. At the A-monomer end, $s = 0$, at the junction point between A and B blocks, $s = f$, and at the other end $s = 1$. The configuration of the αth block ($\alpha = A, B$) is then represented by a mathematical space curve, $\mathbf{r}_\alpha(s)$.

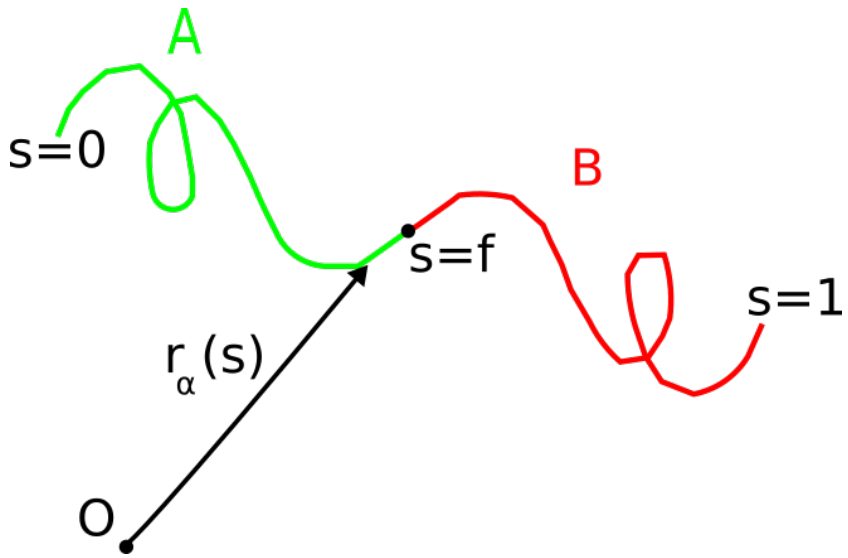

Figure 2.2: Cartoon of a continuous chain of an AB diblock copolymer with the space curve $\mathbf{r}_\alpha(s)$, where $s \in [0,1]$ is a contour parameter and α denots for A or B block. f is a parameter indicating the ratio of the A block to the total chain.

The microscopic concentration operators of A and B segments at a given point $\mathbf{r}$ are defined as:

$$\hat{\phi}_A(\mathbf{r}) = \frac{N}{\rho_0}\sum_{j=1}^{n}\int_0^f ds\,\delta(\mathbf{r}-\mathbf{r}_j(s)) \tag{2.1}$$

$$\hat{\phi}_B(\mathbf{r}) = \frac{N}{\rho_0}\sum_{j=1}^{n}\int_f^1 ds\,\delta(\mathbf{r}-\mathbf{r}_j(s)) \tag{2.2}$$

These concentrations are made dimensionless by dividing by the average segment density ρ_0 ($\rho_0 = \frac{nN}{V}$). The segments here are assumed to have the same monomer volume ρ_0^{-1}.

The interaction potential of the melt takes the form:

$$\mathcal{H}_J = k_B T\rho_0\chi\int d\mathbf{r}\,\hat{\phi}_A(\mathbf{r})\hat{\phi}_B(\mathbf{r}) + k_B T\rho_0\frac{\kappa}{2}\int d\mathbf{r}\left[\hat{\phi}_A(\mathbf{r})+\hat{\phi}_B(\mathbf{r})-1\right]^2 \tag{2.3}$$

where χ is the Flory-Huggins parameter, that varies with the temperature, specifying the incompatibility between A and B segments; κ is the inverse isothermal compressibility or Helfand parameter. It is the proper measure of the tendency to attract copolymers into regions with $\hat{\phi}_A(\mathbf{r})+\hat{\phi}_B(\mathbf{r}) < 1$, and repel copolymers when the total density is greater than 1. When $\kappa \to \infty$, we approach the incompressibility limit. For simplicity, most studies consider incompressible diblock copolymer melts, where the total density of A and B-block is always a constant $\Phi_A + \Phi_B = 1$. In this case, the last term in equation 2.3 is zero. However, this approximation fails under certain conditions. For instance, when a copolymer melt is confined between two surfaces, the Dirichlet boundary conditions are incompatible with the incompressibility constraint at the surfaces. One way to solve this incompatibility is allowing the variation of

the total density of copolymers near the surfaces [55]. The thermal energy $k_B T$ and average segment density ρ_0 are included to make χ and κ dimensionless. We shall consider $k_B T = 1$, as a convention.

The canonical partition function is written as the functional integral

$$\begin{aligned} Z_C &= \frac{1}{n!}\int\left(\prod_{j=1}^{n}\mathscr{D}\{\mathbf{r}_j\}\right) P[\mathbf{r}_j;0,1]\, e^{-F_C/k_B T} \\ &= \frac{1}{n!}\int\left(\prod_{j=1}^{n}\mathscr{D}\{\mathbf{r}_j\}\right) P[\mathbf{r}_j;0,1]\, \exp\left[-\rho_0\chi\int d\mathbf{r}\hat{\phi}_A(\mathbf{r})\hat{\phi}_B(\mathbf{r})\right] \\ &\quad \exp\left[-\rho_0\frac{\kappa}{2}\int d\mathbf{r}\,(\hat{\phi}_A(\mathbf{r})+\hat{\phi}_B(\mathbf{r})-1)^2\right] \end{aligned} \tag{2.4}$$

where the functional integral is taken over all configurations of the melt system. We assume flexible Gaussian chain polymers [20]; therefore, the probability distribution for individual configuration can be expressed as

$$P[\mathbf{r}_j;0,1] = \mathcal{N}\exp\left[\frac{-3}{2Nb^2}\int_0^f ds\,\left|\frac{d}{ds}\mathbf{r}_A(s)\right|^2 - \frac{3}{2Nb^2}\int_f^1 ds\,\left|\frac{d}{ds}\mathbf{r}_B(s)\right|^2\right] \tag{2.5}$$

where $d\mathbf{r}_\alpha(s)/ds$ is the derivative of the space curve $\mathbf{r}_\alpha(s)$ at contour position s ($\alpha = A, B$), b is the statistical segment length and $\mathcal{N}$ is the normalization factor. The probability distribution $P[\mathbf{r}_j;0,1]$ accounts for the internal stretching energy of the chain.

To make the expression for the partition function more compact, we insert the identity $\int\mathscr{D}\phi_\alpha\delta(\phi_\alpha-\hat{\phi}_\alpha)$ permitting the replacement of operators $\hat{\phi}_\alpha$ in equation (2.4) by the functions ϕ_α ($\alpha = A, B$).

$$\begin{aligned} 1 &= \int\mathscr{D}\{\phi_\alpha\}\,\delta(\phi_\alpha-\hat{\phi}_\alpha) \\ &= \int\mathscr{D}\{\phi_\alpha\}\int_{i\infty}\mathscr{D}\{w_\alpha\}\,\exp\left[\rho_0\int d\mathbf{r}\;w_\alpha(\phi_\alpha-\hat{\phi}_\alpha)\right] \end{aligned} \tag{2.6}$$

We denote

$$\int\mathscr{D}\{.\} = \frac{1}{n!}\int\left(\prod_{j=1}^{n}\mathscr{D}\{\mathbf{r}_j\}\right) P[\mathbf{r}_j;0,1] \tag{2.7}$$

Thus, we have the canonical partition function as below:

$$\begin{aligned} Z_C &= \int\mathscr{D}\{.\}\int\mathscr{D}\{\phi_A\}\int_{i\infty}\mathscr{D}\{w_A\}\int\mathscr{D}\{\phi_B\}\int_{i\infty}\mathscr{D}\{w_B\}\,\exp\left[-\rho_0\chi\int d\mathbf{r}\,\phi_A\phi_B\right] \\ &\quad \exp\left[-\rho_0\frac{\kappa}{2}\int d\mathbf{r}\,(\phi_A+\phi_B-1)^2\right]\exp\left[\sum_{\alpha=A,B}\rho_0\int d\mathbf{r}\;w_\alpha(\phi_\alpha-\hat{\phi}_\alpha)\right] \\ &= \int\mathscr{D}\{\phi_A\}\int_{i\infty}\mathscr{D}\{w_A\}\int\mathscr{D}\{\phi_B\}\int_{i\infty}\mathscr{D}\{w_B\}\,\exp\left[-\rho_0\int d\mathbf{r}\,\left(\chi\phi_A\phi_B+\frac{\kappa}{2}(\phi_A+\phi_B-1)^2\right)\right] \\ &\quad \exp\left[\sum_{\alpha=A,B}\rho_0\int d\mathbf{r}\;w_\alpha\phi_\alpha\right]\int\mathscr{D}\{.\}\,\exp\left[\sum_{\alpha=A,B}\rho_0\int d\mathbf{r}\;w_\alpha\hat{\phi}_\alpha\right] \\ &= \int\mathscr{D}\{\phi_A\}\int_{i\infty}\mathscr{D}\{w_A\}\int\mathscr{D}\{\phi_B\}\int_{i\infty}\mathscr{D}\{w_B\}\,e^{-F_C} \end{aligned} \tag{2.8}$$

Therefore, the corresponding free energy of the system results

$$\begin{aligned} F_C &= \rho_0 \int d\mathbf{r}\, \left[\chi\phi_A(\mathbf{r})\phi_B(\mathbf{r}) + \frac{\kappa}{2}\left(\phi_A(\mathbf{r}) + \phi_B(\mathbf{r}) - 1\right)^2\right] \\ &\quad -\rho_0 \int d\mathbf{r}\, \left[w_A(\mathbf{r})\phi_A(\mathbf{r}) + w_B(\mathbf{r})\phi_B(\mathbf{r})\right] \\ &\quad -\ln\left\{\int \mathscr{D}\{.\}\, \exp\left[-\phi_0 \int d\mathbf{r}\, \left(w_A(\mathbf{r})\hat{\phi}_A(\mathbf{r}) + w_B(\mathbf{r})\hat{\phi}_B(\mathbf{r})\right)\right]\right\} \end{aligned} \tag{2.9}$$

We redefine the fields by including the factor N, $Nw_\alpha(\mathbf{r}) \to \omega_\alpha(\mathbf{r})$. After this manipulation, we get the result

$$\begin{aligned} F_C &= \rho_0 \int d\mathbf{r}\, \left[\chi\phi_A(\mathbf{r})\phi_B(\mathbf{r}) + \frac{\kappa}{2}\left(\phi_A(\mathbf{r}) + \phi_B(\mathbf{r}) - 1\right)^2\right] \\ &\quad -\frac{\rho_0}{N} \int d\mathbf{r}\, \left[\omega_A(\mathbf{r})\phi_A(\mathbf{r}) + \omega_B(\mathbf{r})\phi_B(\mathbf{r})\right] \\ &\quad -\ln\left\{\int \mathscr{D}\{.\}\, \exp\left[\frac{-\rho_0}{N} \int d\mathbf{r}\, \left(\omega_A(\mathbf{r})\hat{\phi}_A(\mathbf{r}) + \omega_B(\mathbf{r})\hat{\phi}_B(\mathbf{r})\right)\right]\right\} \end{aligned} \tag{2.10}$$

where

$$\begin{aligned} &\int \mathscr{D}\{.\}\, \exp\left[\frac{-\rho_0}{N} \int d\mathbf{r}\, \left(\omega_A(\mathbf{r})\hat{\phi}_A(\mathbf{r}) + \omega_B(\mathbf{r})\hat{\phi}_B(\mathbf{r})\right)\right] \\ &= \int \mathscr{D}\{.\}\, \exp\left[\frac{-\rho_0}{N} \int d\mathbf{r}\, \omega_A(\mathbf{r}) \frac{N}{\rho_0} \sum_{j=1}^{n} \int_0^f ds\, (\mathbf{r} - \mathbf{r}'(s))\right] \\ &\quad \exp\left[-\frac{\rho_0}{N} \int d\mathbf{r}\, \omega_B(\mathbf{r}) \frac{N}{\rho_0} \sum_{j=1}^{n} \int_f^1 ds\, (\mathbf{r} - \mathbf{r}'(s))\right] \\ &= \int \mathscr{D}\{.\}\, \exp\left[-\sum_{j=1}^{n} \int_0^f ds\, \omega_A(\mathbf{r}(\mathbf{s})) - \sum_{j=1}^{n} \int_f^1 ds\, \omega_B(\mathbf{r}(\mathbf{s}))\right] \\ &= \frac{1}{n!} \int \left(\prod_{j=1}^{n} \mathscr{D}\{\mathbf{r}_j\}\right) P[\mathbf{r}_j; 0, 1] \exp\left[-\sum_{j=1}^{n} \int_0^f ds\, \omega_A(\mathbf{r}(\mathbf{s})) - \sum_{j=1}^{n} \int_f^1 ds\, \omega_B(\mathbf{r}(\mathbf{s}))\right] \\ &= \frac{1}{n!} Q^n \end{aligned} \tag{2.11}$$

with

$$\begin{aligned} Q[\omega] &= \int \mathscr{D}\{\mathbf{r}_j\} P[\mathbf{r}_j; 0, 1] \exp\left[-\int_0^f ds\, \omega_A(\mathbf{r}(\mathbf{s})) - \int_f^1 ds\, \omega_B(\mathbf{r}(\mathbf{s}))\right] \\ &= \int \mathscr{D}_j\{.\}\, \exp\left[-\int_0^f ds\, \omega_A(\mathbf{r}(\mathbf{s})) - \int_f^1 ds\, \omega_B(\mathbf{r}(\mathbf{s}))\right] \end{aligned} \tag{2.12}$$

Here $Q[\omega]$ is the partition function of a single non-interacting polymer chain subjected to external fields $\omega_\alpha(\mathbf{r})$. The square brackets on $Q[\omega]$ denote that it

is a functional that depends on the fields $\omega_\alpha(\mathbf{r})$.
Then the free energy can be rewritten as,

$$\begin{aligned} F_C &= \rho_0 \int d\mathbf{r} \left[\chi\phi_A(\mathbf{r})\phi_B(\mathbf{r}) + \frac{\kappa}{2}\left(\phi_A(\mathbf{r}) + \phi_B(\mathbf{r}) - 1\right)^2\right] \qquad (2.13) \\ &\quad -\frac{\rho_0}{N}\int d\mathbf{r}\ [\omega_A(\mathbf{r})\phi_A(\mathbf{r}) + \omega_B(\mathbf{r})\phi_B(\mathbf{r})] - \ln\left(\frac{Q^n}{n!}\right) \\ &\approx -n\ln Q + \rho_0\chi\int d\mathbf{r}\,\phi_A(\mathbf{r})\phi_B(\mathbf{r}) + \rho_0\frac{\kappa}{2}\int d\mathbf{r}\ \left(\phi_A(\mathbf{r}) + \phi_B(\mathbf{r}) - 1\right)^2 \\ &\quad -\frac{\rho_0}{N}\int d\mathbf{r}\ [\omega_A(\mathbf{r})\phi_A(\mathbf{r}) + \omega_B(\mathbf{r})\phi_B(\mathbf{r})] \qquad (2.14) \end{aligned}$$

where the Stirling approximation was used

$$\ln\left(\frac{Q^n}{n!}\right) \approx n\ln\left(\frac{Q}{n}\right) + \text{const} = n\ln Q + \text{const} \qquad (2.15)$$

Note that the entropic free energy or equivalently the entropy according to standard statistical mechanics is $f_e = -T\,S$. Therefore, the entropic energy of the diblock copolymer melt is

$$\frac{f_e}{k_B T} = -n\ln Q - \frac{\rho_0}{N}\int d\mathbf{r}\ [\omega_A(\mathbf{r})\phi_A(\mathbf{r}) + \omega_B(\mathbf{r})\phi_B(\mathbf{r})] \qquad (2.16)$$

The product of n chains and the logarithm of the single chain partition function $Q[\omega]$ gives the total free energy of the n diblock copolymers in the mean field approximation, while the integral of the product of fields and densities removes the average internal energy gained from the fields.

In SCFT, the free energy of the melt is approximated by $F_C[\phi_A, \phi_B, \omega_A, \omega_B]$, where the functions ϕ_α and ω_α correspond to a saddle point obtained by equating the functional derivatives of equation 2.14 to zero. Thus the self-consistent equations can be obtained by extremizing the free energy with respect to the fields $\omega_\alpha(\mathbf{r})$ and average segment densities $\phi_\alpha(\mathbf{r})$

$$\begin{aligned} \omega_A(\mathbf{r}) &= N\chi\phi_B(\mathbf{r}) + N\kappa\left[\phi_A(\mathbf{r}) + \phi_B(\mathbf{r}) - 1\right] \qquad (2.17) \\ \omega_B(\mathbf{r}) &= N\chi\phi_A(\mathbf{r}) + N\kappa\left[\phi_A(\mathbf{r}) + \phi_B(\mathbf{r}) - 1\right] \qquad (2.18) \\ \phi_A(\mathbf{r}) &= \frac{-nN}{\rho_0 Q}\frac{\delta Q}{\delta\omega_A(\mathbf{r})} \qquad (2.19) \\ \phi_B(\mathbf{r}) &= \frac{-nN}{\rho_0 Q}\frac{\delta Q}{\delta\omega_B(\mathbf{r})} \qquad (2.20) \end{aligned}$$

$$\begin{aligned} \frac{\delta Q}{\delta\omega_A(\mathbf{x})} &= -\int_0^f ds\ q(\mathbf{r}, s)q^\dagger(\mathbf{r}, 1-s) \qquad (2.21) \\ \frac{\delta Q}{\delta\omega_B(\mathbf{x})} &= -\int_f^1 ds\ q(\mathbf{r}, s)q^\dagger(\mathbf{r}, 1-s) \qquad (2.22) \end{aligned}$$

The two equations (2.19) and (2.20) identify $\phi_A(\mathbf{r})$ and $\phi_B(\mathbf{r})$ as the average segment densities of A and B blocks at position $\mathbf{r}$ as calculated in an ensemble

of non-interacting polymers subject to the fields, $\omega_A(\mathbf{r})$ and $\omega_B(\mathbf{r})$, which act on A and B blocks, respectively.

Here the two propagators q and $q^\dagger$ are defined as

$$q(\mathbf{r},s) = \begin{cases} \int \mathscr{D}_j\{.\}\,\delta(\mathbf{r}(s)-\mathbf{x})\exp\left[-\int_0^s d\tau\,\omega_A(\mathbf{r}(\tau))\right] & 0<s<f \\ \int \mathscr{D}_j\{.\}\,\delta(\mathbf{r}(s)-\mathbf{x})\exp\left[-\int_0^f d\tau\,\omega_A(\mathbf{r}(\tau))-\int_f^s d\tau\,\omega_B(\mathbf{r}(\tau))\right] & f<s<1 \end{cases} \tag{2.23}$$

$$q^\dagger(\mathbf{r},1-s) = \begin{cases} \int \mathscr{D}_j\{.\}\,\delta(\mathbf{r}(s)-\mathbf{x})\exp\left[-\int_s^f d\tau\,\omega_A(\mathbf{r}(\tau))-\int_f^1 d\tau\,\omega_B(\mathbf{r}(\tau))\right] & 0<s<f \\ \int \mathscr{D}_j\{.\}\,\delta(\mathbf{r}(s)-\mathbf{x})\exp\left[-\int_s^1 d\tau\,\omega_B(\mathbf{r}(\tau))\right] & f<s<1 \end{cases} \tag{2.24}$$

The physical meaning of these propagators $q(\mathbf{r},s)$ and $q^\dagger(\mathbf{r},1-s)$ are the probability of finding the end of a chain fragment containing the segments $[0:f]$ and $[1:f]$, respectively. The propagators are referred to as forward and backward propagators [56], also as end-segment distribution functions [57, 58]. Then the single chain partition function is related to the integral of the two end-segment distribution functions as follows:

$$Q[\omega] = \int d\mathbf{r}\, q(\mathbf{r},s)\, q^\dagger(\mathbf{r},1-s) \tag{2.25}$$

Furthermore, the end-segment distribution functions satisfy the equations below, which are normally referred to as the modified diffusion equations (MDEs) in the community of polymer scientists:

$$\frac{\partial q(\mathbf{r},s)}{\partial s} = \frac{Nb^2}{6}\nabla^2 q(\mathbf{r},s) - \omega_\alpha(\mathbf{r})q(\mathbf{r},s) \tag{2.26}$$

Length in the system is expressed in units of the unperturbed radius gyration R_g, which is given by $R_g^2 = \frac{Nb^2}{6}$, the diffusion equation becomes

$$\frac{\partial q(\mathbf{r},s)}{\partial s} = \nabla^2 q(\mathbf{r},s) - \omega_\alpha(\mathbf{r})q(\mathbf{r},s) \tag{2.27}$$

with

$$\omega_\alpha(\mathbf{r},s) = \begin{cases} \omega_A(\mathbf{r}) & \text{for } 0<s<f \\ \omega_B(\mathbf{r}) & \text{for } f<s<1 \end{cases} \tag{2.28}$$

and the initial condition $q(\mathbf{r},0)=1$.

The diffusion equation for the propagator $q^\dagger(\mathbf{r},1-s)$ is similar, with initial condition $q^\dagger(\mathbf{r},1)=1$.

The self-consistent equations are finally written as:

$$\omega_A(\mathbf{r}) = N\chi\phi_B(\mathbf{r}) + N\kappa\left[\phi_A(\mathbf{r})+\phi_B(\mathbf{r})-1\right] \tag{2.29}$$

$$\omega_B(\mathbf{r}) = N\chi\phi_A(\mathbf{r}) + N\kappa\left[\phi_A(\mathbf{r})+\phi_B(\mathbf{r})-1\right] \tag{2.30}$$

$$\phi_A(\mathbf{r}) = \frac{V}{Q}\int_0^f ds\, q(\mathbf{r},s)q^\dagger(\mathbf{r},1-s) \tag{2.31}$$

$$\phi_B(\mathbf{r}) = \frac{V}{Q}\int_f^1 ds\, q(\mathbf{r},s)q^\dagger(\mathbf{r},1-s) \tag{2.32}$$

Sometimes, it is more convenient to work in grand canonical ensemble. The grand canonical partition function has form

$$\begin{aligned} Z_{GC} &= \sum_{n=0}^{\infty} \frac{e^{\mu n/k_B T}}{n!} \int \left(\prod_{j=1}^{n} \mathscr{D}\{\mathbf{r}_j\} \right) P[\mathbf{r}_j; 0, 1] e^{-F_{GC}/k_B T} \\ &= \sum_{n=0}^{\infty} \frac{e^{\mu n}}{n!} \int \left(\prod_{j=1}^{n} \mathscr{D}\{\mathbf{r}_j\} \right) P[\mathbf{r}_j; 0, 1] \exp\left[-\rho_0 \chi \int d\mathbf{r} \hat{\phi}_A(\mathbf{r}) \hat{\phi}_B(\mathbf{r}) \right] \\ &\quad \exp\left[-\rho_0 \frac{\kappa}{2} \int d\mathbf{r} \left(\hat{\phi}_A(\mathbf{r}) + \hat{\phi}_B(\mathbf{r}) - 1 \right)^2 \right] \end{aligned} \tag{2.33}$$

where μ is the chemical potential of diblock copolymers. After having the partition function Z_{GC} in hand, we apply the completely analogous way as for canonical ensemble. We then obtain the grand canonical free energy:

$$\begin{aligned} F_{GC} &= -e^{\mu} Q + \rho_0 \int d\mathbf{r} \left[\chi \phi_A(\mathbf{r}) \phi_B(\mathbf{r}) + \frac{\kappa}{2} \left(\phi_A(\mathbf{r}) + \phi_B(\mathbf{r}) - 1 \right)^2 \right] \\ &\quad - \frac{\rho_0}{N} \int d\mathbf{r} \left[\omega_A(\mathbf{r}) \phi_A(\mathbf{r}) + \omega_B(\mathbf{r}) \phi_B(\mathbf{r}) \right] \end{aligned} \tag{2.34}$$

The self-consistent equations for grand canonical ensemble are:

$$\omega_A(\mathbf{r}) = N\chi\phi_B(\mathbf{r}) + N\kappa\left[\phi_A(\mathbf{r}) + \phi_B(\mathbf{r}) - 1\right] \tag{2.35}$$

$$\omega_B(\mathbf{r}) = N\chi\phi_A(\mathbf{r}) + N\kappa\left[\phi_A(\mathbf{r}) + \phi_B(\mathbf{r}) - 1\right] \tag{2.36}$$

$$\phi_A(\mathbf{r}) = e^{\mu} \int_0^f ds\, q(\mathbf{r}, s) q^{\dagger}(\mathbf{r}, 1-s) \tag{2.37}$$

$$\phi_B(\mathbf{r}) = e^{\mu} \int_f^1 ds\, q(\mathbf{r}, s) q^{\dagger}(\mathbf{r}, 1-s) \tag{2.38}$$

We will discuss approximations and numerical methods used to solve these modified diffusion equations in the next chapter.

3

METHODS

In the previous chapter we derived self-consistent equations by employing the mean field approximation and the exact expressions for the partition function and propagators of a single chain in external potentials. It is not easy to get exact analytical solutions of these equations. There are several approximation methods to derive an analytical expression for partition function and propagators of a single chain, including the ground state dominance approximation [10, 59], Semenov's strong segregation theory [60], and the weak segregation theory of Leibler [61]. Unfortunately, these analytical methods are limited in applicability, and thus a more general method is desirable. In this chapter we will discuss the ground state dominance approximation and the numerical methods used to solve the modified equations (the main task), which is the most time-consuming part, of this thesis.

3.1 GROUND STATE DOMINANCE

One of the important ways to analyze the modified diffusion equations (2.27) for continuous chain models is to employ eigenfunction expansions. These expansions are familiar methods in quantum mechanics [62]. It is called the ground state dominance approximation and is suitable when polymers of high molecular weight are constrained to a region of characteristic size smaller than to their radius of gyration R_g [20]. To illustrate the method for the continuous Gaussian chain approximation, it is useful to write the modified diffusion equations (see equations 2.27) as:

$$\frac{\partial q(\mathbf{r}, s)}{\partial s} = \mathcal{L} q(\mathbf{r}, s) \tag{3.1}$$

where $\mathcal{L}$ is defined by

$$\mathcal{L} = \nabla^2 - \omega_\alpha(\mathbf{r}) \tag{3.2}$$

With the real fields $\omega_\alpha(\mathbf{r})$ and suitable boundary conditions, the operator $\mathcal{L}$ has real eigenvalues λ_k and eigenfunctions $\Psi_k(\mathbf{r})$ that are orthogonal and complete. Then we have an equation to describe the property of $\mathcal{L}$

$$\mathcal{L}\Psi_k(\mathbf{r}) = -\lambda_k \Psi_k(\mathbf{r}), \qquad k = 0, 1, 2, \ldots, \infty \tag{3.3}$$

where the index k is chosen such that λ_0 is the smallest eigenvalue, which we call the ground state eigenvalue. The eigenfunctions are assumed to be normalized. The properties of orthogonality and completeness are described via the following equations

$$\int d\mathbf{r}\, \Psi_i(\mathbf{r})\, \Psi_j(\mathbf{r}) = \delta_{ij} \tag{3.4}$$

$$\sum_{k=0}^{\infty} \Psi_k(\mathbf{r}')\, \Psi_k(\mathbf{r}) = \delta(\mathbf{r}-\mathbf{r}') \tag{3.5}$$

The solution of equation 3.1 can be expressed in terms of the eigenfuctions $\Psi_k(\mathbf{r})$ of operator $\mathcal{L}$ according to

$$q(\mathbf{r}, s) = \sum_{k=0}^{\infty} C_k\, \Psi_k(\mathbf{r})\, e^{-s\lambda_k} \tag{3.6}$$

Using the initial conditions $q(\mathbf{r}, 0) = 1$, we get

$$1 = \sum_{k=0}^{\infty} C_k\, \Psi_k(\mathbf{r}) \tag{3.7}$$

After applying the orthonormal property of the eigenfunctions we obtain the expression for the coefficients C_k

$$C_k = \int d\mathbf{r}\, \Psi_k(\mathbf{r}) \tag{3.8}$$

However, the eigenfunction expansion has restrictions due to our ability to solve equation 3.3 for a given boundary conditions and summing the infinite series. In most realistic cases in polymer physics, we cannot find analytical expression for eigenvalues and eigenfunction or sum over infinite series such as equation 3.6. The ground state dominance approximation applies when the eigenfunction expansion is truncated after the leading $k = 0$ term, that is

$$q(\mathbf{r}, s) \approx C_0\, \Psi_0(\mathbf{r})\, e^{-s\lambda_0} \tag{3.9}$$

$$C_0 = \int d\mathbf{r}\, \Psi_0(\mathbf{r}) \tag{3.10}$$

In this case, then the partition function will be

$$\begin{aligned} Q[\omega] &= \frac{1}{V}\int d\mathbf{r}\, q(\mathbf{r}, N) = \frac{1}{V}\sum_{k=0}^{\infty} C_k^2 e^{-N\lambda_k} \\ &\approx \frac{C_0^2}{V} e^{-N\lambda_0} \end{aligned} \tag{3.11}$$

and the density is

$$\begin{aligned} \phi(\mathbf{r}) &= -\frac{\delta \ln Q[\omega]}{\delta\omega(\mathbf{r})} = \frac{1}{V\,Q}\int_0^1 ds\, q(\mathbf{r}, s)\, q^{\dagger}(\mathbf{r}, 1-s) \\ &\approx \frac{N C_0^2}{V\,Q}[\Psi_0]^2\, e^{-N\lambda_0} = N[\Psi_0]^2 \end{aligned} \tag{3.12}$$

The normalized condition 3.4 ensures that the dimensionless density in the ground state approximation has the correct normalization

$$\int d\mathbf{r}\, \phi(\mathbf{r}) = N \tag{3.13}$$

The ground state approximation is evidently the leading term in an asymptotic expansion for $N \to \infty$. However, the validity of the truncation after the leading term is limited. There are two conditions for the approximation to be valid

- The eigenvalues must be discrete since the polymer is localized by the potential to finite regions of space.
- The eigenvalue space and the chain length should be large enough to make the ground state dominant, so that the relative contribution of the first term compared to the leading term can be neglected. This means that

$$e^{-N(\lambda_1-\lambda_0)} \ll 1 \tag{3.14}$$

The above conditions are common in problems where polymers are absorbed at surfaces or interfaces. When the ground state replaces the full eigenfunction expansion we have

$$\mathcal{L}\Psi_0(\mathbf{r}) = \nabla^2\Psi_0(\mathbf{r}) - \omega(\mathbf{r})\Psi_0(\mathbf{r}) = -\lambda_0\Psi_0(\mathbf{r}) \tag{3.15}$$

By solving this equation, we obtain $\Psi_0(\mathbf{r})$ and then the propagator $q(\mathbf{r}, s)$ ($q^\dagger(\mathbf{r}, 1-s)$).

3.2 NUMERICAL METHOD

3.2.1 *Numerical Algorithm*

The solution of the mean field equations is not trivial since the modified diffusion equations are self-consistent, and they can only be solved by an iterative procedure. The general scheme of the numerical algorithm to solve self-consistent equations is described in the following flowchart.

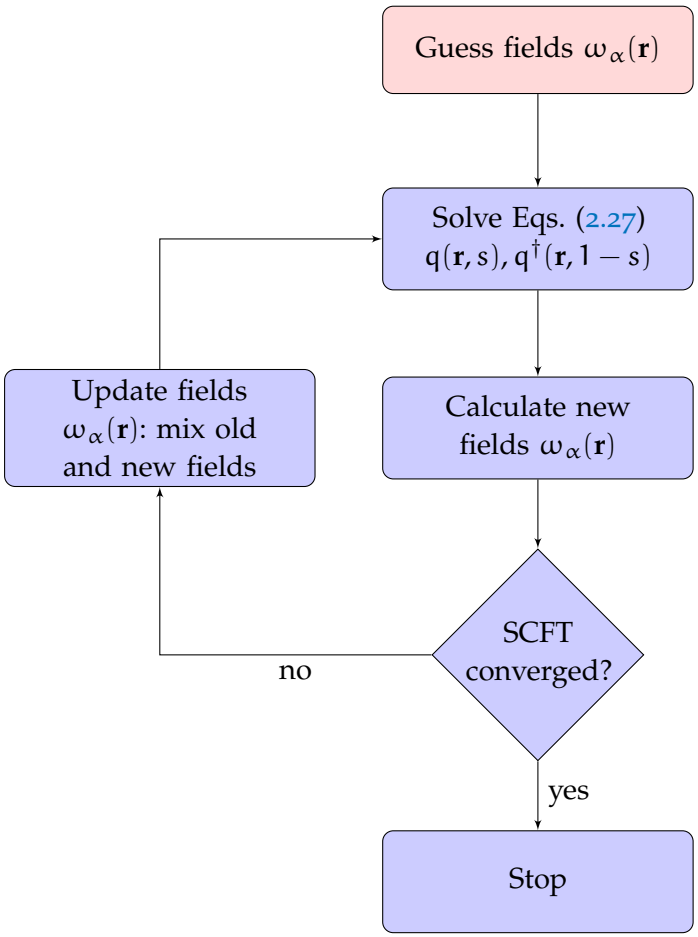

The flowchart describes the steps involved in the numerical algorithm which is used to solve the SCFT equations. The first step of the algorithm is making a guess for the initial values for the fields. We can choose reasonable ones which are close to equilibrium (if we foresee them) or even random fields. Using these initial fields, the MDEs (2.27) are solved to obtain the propagators $q(\mathbf{r}, s)$ and $q^\dagger(\mathbf{r}, 1-s)$. Solving MDEs is a numerical challenge. One needs a fast method to do it. The monomer volume fractions are calculated by integrating the propagators along the chain contour via equations (2.31) and (2.32) for the canonical ensemble and equations (2.37) and (2.38) for the grand canonical ensemble. After that we can compute the new fields and then compare it to the SCFT convergence condition. If the convergence condition is not reached then we update the fields using an appropriate iteration scheme, such as, Anderson

mixing, simple mixing, or alpha mixing. The updated fields are then used as input for the modified diffusion equations (MDEs) (2.27), and the whole procedure is repeated until the SCFT convergence condition is reached. Once the final solutions of equations (2.27) are obtained, the free energy of the system is calculated through equation (2.14) for the canonical ensemble and (2.34) for the grand canonical ensemble.

From the general scheme, we know that the main task is to solve the modified diffusion equations (2.27). We can solve them by spectral (Fourier space), pseudo-spectral or real space methods. Each of these methods have different advantages and drawbacks.

The spectral method has been pioneered by Matsen and Schick, and involves calculating the field functions in a Fourier basis. This Fourier basis consists of functions which must satisfy two requirements [23]: the functions are the eigenfunctions of the Laplacian operator and they must have the same symmetries as the phase of the fluid at the saddle point. It is the most efficient numerical method so far when dealing with periodic morphologies in bulk materials [63]. However, the spectral method is not efficient when applied to complex systems without these symmetries. In these cases, the pseudo-spectral method becomes more efficient [64].

It is worth going into details of the real space method since it is used in this thesis. The algorithm, used here to solve modified diffusion equations in real space, is Crank-Nicolson. We will discuss the algorithm in detail below.

3.2.1.1 *The Crank-Nicolson Algorithm For The One Dimensional Problem*

We use the Crank-Nicolson scheme [65] to descretize the MDEs (2.27). It is a finite difference method for solving partial differential equations. Let us consider the one dimensional problem

$$\frac{\partial q(x,s)}{\partial s} = \frac{\partial^2 q(x,s)}{\partial x^2} - \omega(x,s)q(x,s) \tag{3.16}$$

then the descretized modified equation is

$$\frac{q_j^{n+1} - q_j^n}{\Delta s} = \frac{q_{j-1}^n - 2q_j^n + q_{j+1}^n}{2\Delta x^2} + \frac{q_{j-1}^{n+1} - 2q_j^{n+1} + q_{j+1}^{n+1}}{2\Delta x^2} - \omega_j \frac{q_j^n + q_j^{n+1}}{2} \tag{3.17}$$

where $j = \{1, N_x\}$ are grid points in x-variable, $n = \{1, N_s\}$ represents the steps in contour variable s, $\Delta x = L_x/(N_x - 1)$ is the interval size in real space, and $\Delta s = 1/N_s$ is the contour step size. We can write this equation in a shorter form with the help of $\delta_x^2 q_j = q_{j-1} - 2q_j + q_{j+1}$:

$$\frac{q_j^{n+1} - q_j^n}{\Delta s} = \left(\frac{\delta_x^2}{2\Delta x^2} - \frac{\omega_j}{2}\right)\left(q_j^n + q_j^{n+1}\right) \tag{3.18}$$

This scheme is unconditionally stable for any size of contour variable Δs and it has second-order accuracy in variable s. After some mathematical manipulation, we obtain

$$-\frac{\Delta s}{2\Delta x^2} q_{j-1}^{n+1} + \left(1 + \frac{\Delta s}{\Delta x^2} + \frac{\Delta s}{2}\omega_j\right) q_j^{n+1} - \frac{\Delta s}{2\Delta x^2} q_{j+1}^{n+1} = \frac{\Delta s}{2\Delta x^2} q_{j-1}^{n} + \left(1 - \frac{\Delta s}{\Delta x^2} - \frac{\Delta s}{2}\omega_j\right) q_j^{n} + \frac{\Delta s}{2\Delta x^2} q_{j+1}^{n} \tag{3.19}$$

Knowing the propagator $q_{\{j\}}^n$ at step n, we can calculate the propagator $q_{\{j\}}^{n+1}$ at step $(n+1)$ according to equation (3.19). Actually, (3.19) is a matrix equation and can be written symbolically as $\mathbf{A}\,\mathbf{x} = \mathbf{D}$, where $\mathbf{A}$ is a $(N_x \times N_x)$ matrix, $\mathbf{x}$ and $\mathbf{D}$ are (N_x) matrices. This implies that the computational cost is expensive when N_x or N_s is large. Equation (3.19) can be solved by Gaussian elimination [65] with the initial conditions $q_{\{j\}}^1 = 1$ and the boundary conditions depending on the system. The same procedure can be applied to calculate $q^\dagger(x_j, s_n)$.

3.2.1.2 *The Crank-Nicolson Algorithm For The Two Dimensional Problem*

Now we consider the two dimensional modified diffusion equation:

$$\frac{\partial q(x,z,s)}{\partial s} = \left(\frac{\partial_x^2}{\partial x^2} + \frac{\partial_z^2}{\partial z^2}\right) q(x,z,s) - \omega(x,z,s) q(x,z,s) \tag{3.20}$$

Then, we apply the Crank-Nicolson scheme in two dimensions (2d) in a slightly different way of generalizing the Crank-Nicolson scheme. This is called alternating direction implicit method (ADI). The idea of this method is dividing each contour variable step into two steps of size $\Delta s/2$. Therefore, the 2d ADI scheme is

$$\frac{q_{ik}^{n+1/2} - q_{ik}^n}{\Delta s/2} = \frac{\delta_x^2}{\Delta x^2} q_{ik}^{n+1/2} + \frac{\delta_z^2}{\Delta z^2} q_{ik}^n - \frac{1}{2}\omega_{ik}\left(q_{ik}^{n+1/2} + q_{ik}^n\right) \tag{3.21}$$

$$\frac{q_{ik}^{n+1} - q_{ik}^{n+1/2}}{\Delta s/2} = \frac{\delta_x^2}{\Delta x^2} q_{ik}^{n+1/2} + \frac{\delta_z^2}{\Delta z^2} q_{ik}^{n+1} - \frac{1}{2}\omega_{ik}\left(q_{ik}^{n+1/2} + q_{ik}^{n+1}\right) \tag{3.22}$$

where $i = \{1, N_x\}$ are grid points in x-direction, $k = \{1, N_z\}$ are grid points in z-direction, and $\Delta x, \Delta z$ are the interval sizes in space. After some calculations, we obtain

$$\frac{-\Delta s}{2\Delta x^2} q_{i-1,k}^{n+1/2} + \left(1 + \frac{\Delta s}{\Delta x^2} + \frac{\Delta s\,\omega_{ik}}{4}\right) q_{ik}^{n+1/2} - \frac{\Delta s}{2\Delta x^2} q_{i+1,k}^{n+1/2} = \frac{\Delta s}{2\Delta z^2} q_{i,k-1}^{n} + \left(1 - \frac{\Delta s}{\Delta z^2} - \frac{\Delta s\,\omega_{ik}}{4}\right) q_{ik}^{n} + \frac{\Delta s}{2\Delta z^2} q_{i,k+1}^{n} \tag{3.23}$$

and

$$\frac{-\Delta s}{2\Delta z^2} q_{i,k-1}^{n+1} + \left(1 + \frac{\Delta s}{\Delta z^2} + \frac{\Delta s\,\omega_{ik}}{4}\right) q_{i,k}^{n+1} - \frac{\Delta s}{2\Delta z^2} q_{i,k+1}^{n+1} = \frac{\Delta s}{2\Delta x^2} q_{i-1,k}^{n+1/2} + \left(1 - \frac{\Delta s}{\Delta x^2} - \frac{\Delta s\,\omega_{ik}}{4}\right) q_{i,k}^{n+1/2} + \frac{\Delta s}{2\Delta x^2} q_{i+1,k}^{n+1/2} \tag{3.24}$$

These two equations are tridiagonal and can be solved as equation (3.19) with the initial and boundary conditions from the system. We use the 2d ADI method for two dimensional thin films in this thesis.

3.2.1.3 *The Crank-Nicolson Algorithm For The Three Dimensional Problem*

We now consider the three dimensional modified diffusion equation:

$$\frac{\partial q(\mathbf{r},s)}{\partial s} = \left(\frac{\partial_x^2}{\partial x^2} + \frac{\partial_y^2}{\partial y^2} + \frac{\partial_z^2}{\partial z^2}\right) q(\mathbf{r},s) - \omega(\mathbf{r},s) q(\mathbf{r},s) \tag{3.25}$$

We can apply the Crank-Nicolson scheme for equation (3.25) directly. However, it results in that we will have to solve seven diagonal matrices, which is time consuming. Therefore, we will apply the Crank-Nicolson scheme in a slightly different way compared to the 2d ADI method. We introduce two intermediate variables q^* and q^{**}. Then the descretization of equation (3.25) leads to:

$$\begin{aligned}
\frac{q^*_{i,j,k} - q^n_{i,j,k}}{\Delta s} &= \frac{1}{2}\left(\frac{\delta_x^2}{\Delta x^2} - \frac{\omega_{i,j,k}}{3}\right)(q^*_{i,j,k} + q^n_{i,j,k}) \\
&\quad + \left(\frac{\delta_y^2}{\Delta y^2} + \frac{\delta_z^2}{\Delta z^2} - 2\frac{\omega_{i,j,k}}{3}\right) q^n_{i,j,k} \qquad (3.26) \\
\frac{q^{**}_{i,j,k} - q^n_{i,j,k}}{\Delta s} &= \frac{1}{2}\left(\frac{\delta_x^2}{\Delta x^2} - \frac{\omega_{i,j,k}}{3}\right)(q^*_{i,j,k} + q^n_{i,j,k}) \\
&\quad + \frac{1}{2}\left(\frac{\delta_y^2}{\Delta y^2} - \frac{\omega_{i,j,k}}{3}\right)(q^{**}_{i,j,k} + q^n_{i,j,k}) \\
&\quad + \left(\frac{\delta_z^2}{\Delta z^2} - \frac{\omega_{i,j,k}}{3}\right) q^n_{i,j,k} \qquad (3.27) \\
\frac{q^{n+1}_{i,j,k} - q^n_{i,j,k}}{\Delta s} &= \frac{1}{2}\left(\frac{\delta_x^2}{\Delta x^2} - \frac{\omega_{i,j,k}}{3}\right)(q^*_{i,j,k} + q^n_{i,j,k}) \\
&\quad + \frac{1}{2}\left(\frac{\delta_y^2}{\Delta y^2} - \frac{\omega_{i,j,k}}{3}\right)(q^{**}_{i,j,k} + q^n_{i,j,k}) \\
&\quad + \frac{1}{2}\left(\frac{\delta_z^2}{\Delta z^2} - \frac{\omega_{i,j,k}}{3}\right)(q^{n+1}_{i,j,k} + q^n_{i,j,k}) \qquad (3.28)
\end{aligned}$$

where $i = \{1, N_x\}$ denotes grid points in x-direction, $j = \{1, N_y\}$ denotes grid points in y-direction, and $k = \{1, N_z\}$ denotes grid points in z-direction. Δx, Δy, and Δz are interval sizes in space. After some mathematical calculations, we can obtain the three following equations

$$\begin{aligned}
&\frac{-\Delta s}{2\Delta x^2} q^*_{i-1,j,k} + \left(1 + \frac{\Delta s}{\Delta x^2} + \frac{\Delta s\, \omega_{i,j,k}}{6}\right) q^*_{i,j,k} - \frac{\Delta s}{2\Delta x^2} q^*_{i+1,j,k} \\
&= \frac{\Delta s}{2\Delta x^2} q^n_{i-1,j,k} + \frac{\Delta s}{\Delta y^2} q^n_{i,j-1,k} + \frac{\Delta s}{\Delta z^2} q^n_{i,j,k-1} \\
&\quad + \frac{\Delta s}{2\Delta x^2} q^n_{i+1,j,k} + \frac{\Delta s}{\Delta y^2} q^n_{i,j+1,k} + \frac{\Delta s}{\Delta z^2} q^n_{i,j,k+1} \\
&\quad + \left(1 - \frac{\Delta s}{\Delta x^2} - \frac{2\Delta s}{\Delta y^2} - \frac{2\Delta s}{\Delta z^2} - \frac{5\Delta s\, \omega_{i,j,k}}{6}\right) q^n_{i,j,k} \qquad (3.29)
\end{aligned}$$

$$\begin{aligned}
&\frac{-\Delta s}{2\Delta y^2} q^{**}_{i,j-1,k} + \left(1 + \frac{\Delta s}{\Delta y^2} + \frac{\Delta s\, \omega_{i,j,k}}{6}\right) q^{**}_{i,j,k} - \frac{\Delta s}{2\Delta y^2} q^{**}_{i,j+1,k} \\
&= \frac{-\Delta s}{2\Delta y^2} q^n_{i,j-1,k} + q^*_{i,j,k} + \left(\frac{\Delta s}{\Delta y^2} + \frac{\Delta s\, \omega_{i,j,k}}{6}\right) q^n_{i,j,k} - \frac{\Delta s}{2\Delta y^2} q^n_{i,j+1,k} \qquad (3.30)
\end{aligned}$$

$$\frac{-\Delta s}{2\Delta z^2} q^{n+1}_{i,j,k-1} + \left(1 + \frac{\Delta s}{\Delta z^2} + \frac{\Delta s\, \omega_{i,j,k}}{6}\right) q^{n+1}_{i,j,k} - \frac{\Delta s}{2\Delta z^2} q^{n+1}_{i,j,k+1}$$
$$= \frac{-\Delta s}{2\Delta z^2} q^{n}_{i,j,k-1} + q^{**}_{i,j,k} + \left(\frac{\Delta s}{\Delta z^2} + \frac{\Delta s\, \omega_{i,j,k}}{6}\right) q^{n}_{i,j,k} - \frac{\Delta s}{2\Delta z^2} q^{n}_{i,j,k+1} \quad (3.31)$$

These three equations are tridiagonal matrix equations and can be solved by different methods, such as Gaussian elimination with the initial and boundary conditions depending on the system. We applied this algorithm to investigate three dimensional thin film systems in different coordinate systems, for example, Cartesian coordinates for planar thin films and cylindrical coordinates for curved supported thin films. All the above calculations were done in Cartesian coordinates, I will briefly present the Crank Nicolson method applied for the cylindrical coordinates.

3.2.1.4 *The Crank-Nicolson Algorithm For The Cylindrical Coordinates Problem*

a) The Two Dimensional Cylindrical Coordinates, (r, θ)

The modified diffusion equation in the 2-dimensional cylindrical coordinates (r, θ) takes the form:

$$\frac{\partial q(r,\theta,s)}{\partial s} = \left(\frac{\partial_r^2}{\partial r^2} + \frac{1}{r}\frac{\partial_r}{\partial r} + \frac{1}{r^2}\frac{\partial_\theta^2}{\partial \theta^2}\right) q(r,\theta,s) - \omega(r,\theta,s) q(r,\theta,s) \quad (3.32)$$

We apply the Crank Nicolson method for equation (3.32) similarly as we did for the two dimensional problem in Cartesian coordinates in 3.2.1.2. The discretization of equation (3.32) results in:

$$\frac{q^{n+1/2}_{i,j} - q^{n}_{i,j}}{\Delta s/2} = \frac{\delta_r^2}{\Delta r^2} q^{n+1/2}_{i,j} + \frac{1}{r_i \cdot 2\Delta r}\delta_r q^{n+1/2}_{i,j} + \frac{1}{r_i^2}\frac{\delta_\theta^2}{\Delta\theta^2} q^{n}_{i,j}$$
$$-\frac{1}{2}\omega_{ij}\left(q^{n+1/2}_{i,j} + q^{n}_{i,j}\right) \quad (3.33)$$
$$\frac{q^{n+1}_{i,j} - q^{n+1/2}_{i,j}}{\Delta s/2} = \frac{\delta_r^2}{\Delta r^2} q^{n+1/2}_{i,j} + \frac{1}{r_i \cdot 2\Delta r}\delta_r q^{n+1/2}_{i,j} + \frac{1}{r_i^2}\frac{\delta_\theta^2}{\Delta\theta^2} q^{n+1}_{i,j}$$
$$-\frac{1}{2}\omega_{ij}\left(q^{n+1}_{i,j} + q^{n+1/2}_{i,j}\right) \quad (3.34)$$

where $i = \{1, N_r\}$ denotes grid points in r-direction, $j = \{1, N_\theta\}$ denotes grid points in θ-direction, and Δr, $\Delta\theta$ are the interval sizes in space. δ_r^2, δ_r and δ_θ^2 are defined as:

$$\delta_r^2 q^n = q^n_{i-1,j} - 2q^n_{i,j} + q^n_{i+1,j} \quad (3.35)$$
$$\delta_r q^n = q^n_{i+1} - q^n_{i-1} \quad (3.36)$$
$$\delta_\theta^2 q^n = q^n_{i,j-1} - 2q^n_{i,j} + q^n_{i,j+1} \quad (3.37)$$

After some mathematical manipulation, we obtain the two equations below:

$$\left(\frac{-\Delta s}{2\Delta r^2} + \frac{\Delta s}{4 r_i \Delta r}\right) q^{n+1/2}_{i-1,j} + \left(1 + \frac{\Delta s}{\Delta r^2} + \frac{\Delta s}{4}\omega_{i,j}\right) q^{n+1/2}_{i,j} + \left(\frac{-\Delta s}{2\Delta r^2} - \frac{\Delta s}{4 r_i \Delta r}\right) q^{n+1/2}_{i+1,j}$$
$$= \frac{\Delta s}{2\Delta\theta^2\, r_i^2} q^n_{i,j-1} + \left(1 - \frac{\Delta s}{\Delta\theta^2\, r_i^2} - \frac{\Delta s}{4}\omega_{i,j}\right) q^n_{i,j} + \frac{\Delta s}{2\Delta\theta^2\, r_i^2} q^n_{i,j+1} \quad (3.38)$$

$$\begin{aligned}
&\frac{-\Delta s}{2\Delta\theta^2\, r_i^2} q_{i,j-1}^{n+1} + \left(1 + \frac{\Delta s}{\Delta\theta^2\, r_i^2} + \frac{\Delta s}{4}\omega_{i,j}\right) q_{i,j}^{n+1} - \frac{\Delta s}{2\Delta\theta^2\, r_i^2} q_{i,j+1}^{n+1} \\
&= \left(\frac{\Delta s}{2\Delta r^2} - \frac{\Delta s}{4 r_i \Delta r}\right) q_{i-1,j}^{n+1/2} + \left(1 - \frac{\Delta s}{\Delta r^2} - \frac{\Delta s}{4}\omega_{i,j}\right) q_{i,j}^{n+1/2} \\
&\quad + \left(\frac{\Delta s}{2\Delta r^2} + \frac{\Delta s}{4 r_i\, \Delta r}\right) q_{i+1,j}^{n+1/2}
\end{aligned} \tag{3.39}$$

b) The Two Dimensional Cylindrical Coordinates, (r, z)

Similarly, the modified diffusion equation in the 2-dimensional cylindrical coordinates (r, z) takes the form:

$$\frac{\partial q(r,z,s)}{\partial s} = \left(\frac{\partial_r^2}{\partial r^2} + \frac{1}{r}\frac{\partial_r}{\partial r} + \frac{\partial_z^2}{\partial z^2}\right) q(r,z,s) - \omega(r,z,s) q(r,z,s) \tag{3.40}$$

Applying the Crank Nicolson scheme for equation (3.40), we get the following results:

$$\begin{aligned}
\frac{q_{i,j}^{n+1/2} - q_{i,j}^{n}}{\Delta s/2} &= \frac{\delta_r^2}{\Delta r^2} q_{i,j}^{n+1/2} + \frac{1}{r_i \cdot 2\Delta r}\delta_r q_{i,j}^{n+1/2} + \frac{\delta_z^2}{\Delta z^2} q_{i,j}^{n} \\
&\quad -\frac{1}{2}\omega_{ij}\left(q_{i,j}^{n+1/2} + q_{i,j}^{n}\right)
\end{aligned} \tag{3.41}$$

$$\begin{aligned}
\frac{q_{i,j}^{n+1} - q_{i,j}^{n+1/2}}{\Delta s/2} &= \frac{\delta_r^2}{\Delta r^2} q_{i,j}^{n+1/2} + \frac{1}{r_i \cdot 2\Delta r}\delta_r q_{i,j}^{n+1/2} + \frac{\delta_z^2}{\Delta z^2} q_{i,j}^{n+1} \\
&\quad -\frac{1}{2}\omega_{ij}\left(q_{i,j}^{n+1} + q_{i,j}^{n+1/2}\right)
\end{aligned} \tag{3.42}$$

After some mathematical calculation, we obtain:

$$\begin{aligned}
&\left(\frac{-\Delta s}{2\Delta r^2} + \frac{\Delta s}{4 r_i\, \Delta r}\right) q_{i,j-1}^{n+1/2} + \left(1 + \frac{\Delta s}{\Delta r^2} + \frac{\Delta s}{4}\omega_{i,j}\right) q_{i,j}^{n+1/2} + \left(\frac{-\Delta s}{2\Delta r^2} - \frac{\Delta s}{4 r_i\, \Delta r}\right) q_{i,j+1}^{n+1/2} \\
&= \frac{\Delta s}{2\Delta z^2} q_{i-1,j}^{n} + \left(1 - \frac{\Delta s}{\Delta z^2} - \frac{\Delta s}{4}\omega_{i,j}\right) q_{i,j}^{n} + \frac{\Delta s}{2\Delta z^2} q_{i+1,j}^{n}
\end{aligned} \tag{3.43}$$

$$\begin{aligned}
&\frac{-\Delta s}{2\Delta z^2} q_{i-1,j}^{n+1} + \left(1 + \frac{\Delta s}{\Delta z^2} + \frac{\Delta s}{4}\omega_{i,j}\right) q_{i,j}^{n+1} - \frac{\Delta s}{2\Delta z^2} q_{i+1,j}^{n+1} \\
&= \left(\frac{\Delta s}{2\Delta r^2} - \frac{\Delta s}{4 r_i\, \Delta r}\right) q_{i,j-1}^{n+1/2} + \left(1 - \frac{\Delta s}{\Delta r^2} - \frac{\Delta s}{4}\omega_{i,j}\right) q_{i,j}^{n+1/2} \\
&\quad + \left(\frac{\Delta s}{2\Delta r^2} + \frac{\Delta r}{4 r_i\, \Delta r}\right) q_{i,j+1}^{n+1/2}
\end{aligned} \tag{3.44}$$

The equations (3.38), (3.39), (3.43) and (3.44) are tridiagonal and can be solved as equation (3.19) with the boundary conditions depending on the system. Particularly, in this thesis we apply the Dirichlet boundary conditions in the r-direction and the periodic boundary conditions in the two in-plane directions θ- and z-directions.

3.2.2 *Mixing Methods*

The iteration scheme can be processed with different mixing methods, such as simple mixing, lambda mixing [66] and Anderson mixing [67, 68]. The "simple mixing" method is a very simple technique, where the fields at $(n+1)$th iteration step are updated from the field at nth iteration step according to:

$$\omega_{n+1}^{in} = \omega_n^{in} + \lambda\,(\omega_n^{out} - \omega_n^{in}) = \omega_n^{in} + \lambda\,\Delta\omega_n \tag{3.45}$$

where ω_n^{in} is the input value for the nth iteration step, ω_n^{out} is the resultant field, and ω_{n+1}^{in} is input value for the $(n+1)$th iteration step. $\Delta\omega_n = (\omega_n^{out} - \omega_n^{in})$ is the difference between the output and input values of the field at the nth step. λ is a parameter chosen appropriately to ensure stability (typical value is $\leqslant 0.1$). However, the simple mixing method is sometimes slow and requires many iteration steps for the equations to converge, or even is unstable. An alternative to improve the simple mixing is to determine a new value for λ_n at every iteration step [66]. This method is called "lambda mixing" method. Then the mixing parameter λ_n is determined as the following

$$\begin{aligned} \lambda_n &= \sqrt{\frac{(\omega_n^{in} - \omega_{n-1}^{out})^2}{(\omega_n^{out} - \omega_n^{in} - \omega_{n-1}^{out} + \omega_{n-1}^{in})^2}} \\ &= \sqrt{\frac{(\omega_n^{in} - \omega_{n-1}^{out})^2}{(\Delta\omega_n - \Delta\omega_{n-1})^2}} \end{aligned} \tag{3.46}$$

In this thesis we use the lambda mixing method.

3.2.3 *Discretization Error*

As we discussed before, the Crank-Nicolson algorithm is unconditionally stable, and does not depend on the contour variable step Δs or the space interval size Δx $(\Delta y, \Delta z)$. However, when we apply the surface interaction on thin films (it will be discussed in more detail in later chapters) we realize that the discretization of the modified diffusion equations, specifically the discretization in the direction orthogonal to the film, has important effects on the accuracy of the free energy in the end. The degree of the discretization error depends on the strength of surface interactions as well. It could not be neglected. Especially, it is important to determine the stable morphologies. In order to quantify the effect of the discretization Δz on the accuracy of the free energy, we vary Δz and carefully calculate the shift of the free energy ΔF with different film thicknesses as a function of discretization. We apply the same procedure for every parameter set of surface interactions. Furthermore, for the thin films with curved substrates we vary not only the thickness but also the curvature. Then we use a third order polynomial to fit the shift energy as a function of the discretization Δz. Figure 3.1 presents an example of the shift free energy ΔF as a function of Δz for different thicknesses with certain surface interactions in flat films

This correction for discretization effects will be applied to the SCF data. We note that the fit is very good in the range of Δz from 0 to 0.016. In all

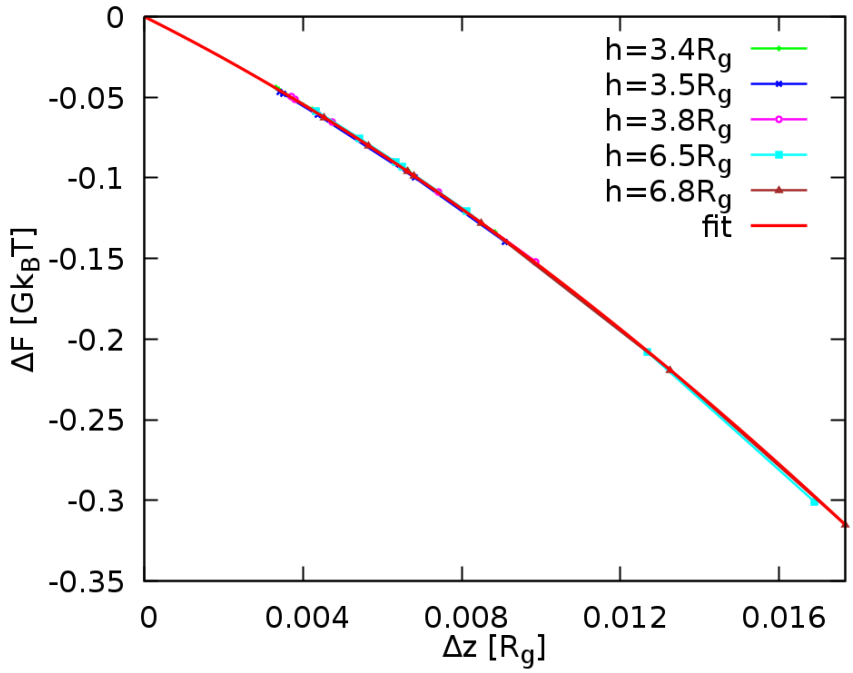

Figure 3.1: Shifted energy ΔF as a function of discretization Δz for different film thicknesses h. The solid line corresponds to the fitting function $\Delta F(\Delta z) = -12.27\,\Delta z - 341\,\Delta z^2 + 1447\,\Delta z^3$.

simulations in this thesis, the discretization in the direction orthogonal to the film surfaces is fixed to values of $\Delta z < 0.015$.

Part II

RESULTS

4

MULTILAYERS OF CYLINDER-FORMING DIBLOCK COPOLYMER THIN FILMS

The self-assembly of block copolymers in thin films has attracted increasing interest in the area of science and nanotechnology due to their capicity to self-assemble into periodic nanostructures [12, 16, 35, 69–72]. Thus, an in-depth understanding of structure formation of the block copolymer films is important to exploit the potential applications of these materials. As a part of this thesis, we study multilayers of cylinder-forming diblock copolymers. We investigate how the first-layer block copolymer acts as a periodic external field that guides and stabilizes the orientation of subsequent layers. In order to analyze the stability of the block copolymer thin film system against the formation of holes and islands and the coupling between layers, we performed SCFT to calculate the free energy and to seek for the minima in the free energy landscape. It allows us to extract structral information, for instance, to determine the optimum thickness of multilayers of cylinder-forming block copolymer systems. We also study the behavior of the average lateral spacing between near neighbor cylinders as a function of the film thickness.

Part of the work presented in this chapter was published in: "Shear-aligned block copolymer monolayers as seeds to control the orientation order in cylinder-forming block copolymer thin films", *Macromolecules*, **49**, 7588-7596, 2016.

4.1 MODEL

We consider a melt of asymmetric AB diblock copolymers confined between two surfaces, which are hard and flat. We assume symmetric boundary wetting conditions where the two surfaces preferentially attract the A-segments of the majority block. The confined film of thickness h is constrained between the two surfaces located at $z = 0$ and $z = h$ (a schematic of the thin film is illustrated in figure 4.1). The two surfaces are identical, which means that the interaction strengths to blocks are the same at the two surfaces. Therefore, the interaction potential of the melt takes the form

$$\begin{aligned}\mathcal{H}_J &= k_B T \rho_0 \chi \int d\mathbf{r} \hat{\phi}_A(\mathbf{r}) \hat{\phi}_B(\mathbf{r}) + k_B T \rho_0 \frac{\kappa}{2} \int d\mathbf{r} \left[\hat{\phi}_A(\mathbf{r}) + \hat{\phi}_B(\mathbf{r}) - 1\right]^2 \\ &\quad + k_B T \rho_0 \int d\mathbf{r} H(\mathbf{r}) \left[\Lambda_A \hat{\phi}_A(\mathbf{r}) + \Lambda_B \hat{\phi}_B(\mathbf{r})\right] \qquad (4.1)\end{aligned}$$

where Λ_A, Λ_B are the strength of the interaction between the A-block and B-block and the surfaces, respectively. $H(\mathbf{r})$ is surface field and we choose the form of surface fields as:

$$H(\mathbf{r}) = \begin{cases} (1+\cos(\pi z/\epsilon)) & 0 \leqslant z \leqslant \epsilon \\ 0 & \epsilon \leqslant z \leqslant h-\epsilon \\ (1+\cos(\pi(h-z)/\epsilon)) & h-\epsilon \leqslant z \leqslant h \end{cases} \tag{4.2}$$

with z being the coordinate perpendicular to the film and ϵ being the distance from the walls, inside which the diblock copolymers will interact with the surfaces. The value of ϵ is small enough relative to the thickness of thin film so that its finite size does not effect the phase behavior significantly. In this thesis, we always choose $\epsilon = 0.2R_g$.

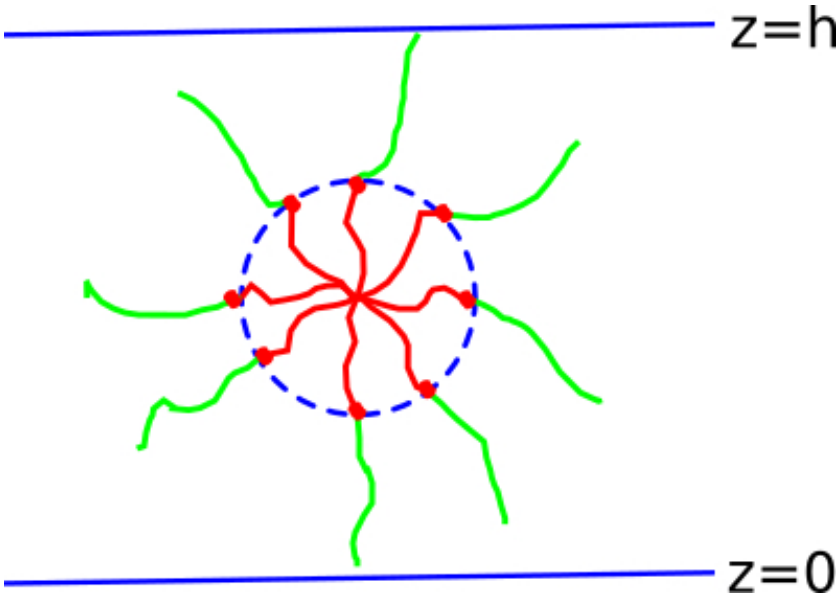

Figure 4.1: Scheme of diblock copolymers confined between two flat sufaces located at $z = 0$ and $z = h$. The block copolymers form cylindrical domains of the minority block.

Our calculations are performed in the grand canonical ensemble. Within the framework of SCFT, the free energy of such a system takes the form

$$\begin{aligned} \frac{N F_{GC}}{\rho_0 k_B T} &= -e^{\mu} Q + \int d\mathbf{r} \left[\chi N \phi_A(\mathbf{r})\phi_B(\mathbf{r}) + \frac{\kappa N}{2}(\phi_A(\mathbf{r}) + \phi_B(\mathbf{r}) - 1)^2\right] \\ &\quad - \int d\mathbf{r} \left[\omega_A(\mathbf{r})\phi_A(\mathbf{r}) + \omega_B(\mathbf{r})\phi_B(\mathbf{r})\right] \\ &\quad + \int d\mathbf{r}\, H(\mathbf{r}) \left[\Lambda_A N\, \phi_A(\mathbf{r}) + \Lambda_B N\, \phi_B(\mathbf{r})\right] \end{aligned} \tag{4.3}$$

So the free energy will be given in units of Gk_BT, where $G = \frac{\rho_0}{N} R_g^3 = \rho_c R_g^3$ is a dimensionless Ginzburg parameter ($\rho_c = \frac{\rho_0}{N} = \frac{n}{V}$ is the average density of the copolymer chain). The Ginzburg parameter thus corresponds to the average number of polymer chains that permeate the volume R_g^3 occupied by

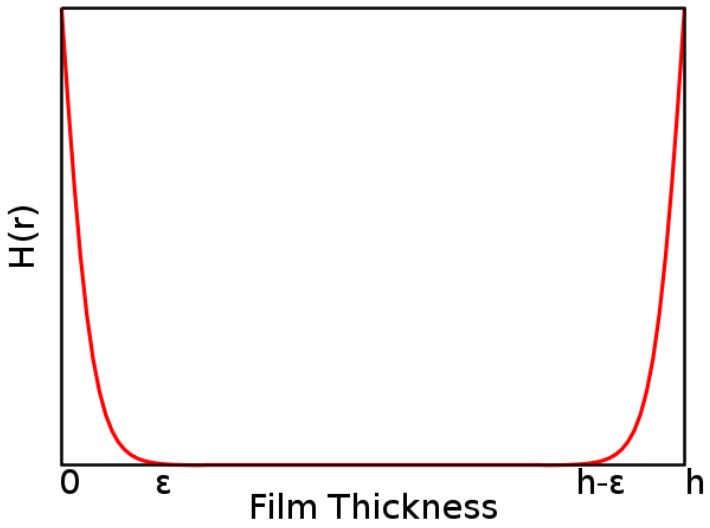

Figure 4.2: Surface interaction fields between the two walls and diblock copolymers, where ϵ is the cutoff distance for the surface interaction.

one chain of interest. This can be very large for concentrated solutions or melts of polymers of high molecular weight [20].
Then by minimizing the free energy with respect to the mono-densities $\phi_{A,B}(\mathbf{r})$ and the fields $\omega_{A,B}(\mathbf{r})$, we obtain the set of self-consistent equations

$$\omega_A(\mathbf{r}) = N\chi\phi_B(\mathbf{r}) + N\kappa\left[\phi_A(\mathbf{r}) + \phi_B(\mathbf{r}) - 1\right] + N\Lambda_A H(\mathbf{r}) \tag{4.4}$$

$$\omega_B(\mathbf{r}) = N\chi\phi_A(\mathbf{r}) + N\kappa\left[\phi_A(\mathbf{r}) + \phi_B(\mathbf{r}) - 1\right] + N\Lambda_B H(\mathbf{r}) \tag{4.5}$$

$$\phi_A(\mathbf{r}) = e^{\mu}\int_0^f ds\, q(\mathbf{r}, s)q^{\dagger}(\mathbf{r}, 1-s) \tag{4.6}$$

$$\phi_B(\mathbf{r}) = e^{\mu}\int_f^1 ds\, q(\mathbf{r}, s)q^{\dagger}(\mathbf{r}, 1-s) \tag{4.7}$$

As discussed in chapter 2, propagators $q(\mathbf{r}, s)$ and $q^{\dagger}(\mathbf{r}, s)$ satisfy the modified diffusion equations (2.27). Here, the surfaces of the two dimensional thin films are planar. Therefore, the Laplace operator has the following form

$$\Delta = \frac{\partial^2}{\partial x^2} + \frac{\partial^2}{\partial z^2} \tag{4.8}$$

Thus the modified diffusion equations are written as:

$$\frac{\partial q(x, z, s)}{\partial s} = \left(\frac{\partial^2}{\partial x^2} + \frac{\partial^2}{\partial z^2}\right) q(x, z, s) - \omega_\alpha q(x, z, s) \tag{4.9}$$

We solve the modified diffusion equations 4.9 by the Crank-Nicolson algorithm. Periodic boundary conditions are imposed in the unconfined directions (x-direction). We consider the same strength of interaction between the blocks and both surfaces. Although a more systematic study is required in order to explore the effect of the polymer/substrate and polymer/air interfaces in detail,

the SCFT calculations considered here allow a rough estimation of the equilibrium configuration for this system. The incompatibility between the blocks is characterized by the product χN, of the Flory-Huggins parameter χ and the number of segments N. Here, we consider an asymmetric diblock copolymer thin film with intermediate segregation strength $\chi N = 20$ and $f = 0.7$, f being the volume fraction of the A-block. We consider the inverse compressibility $\kappa N = 25$ mostly for numerical reasons [52, 73, 74]. The values of the surface interaction parameters are chosen as $\Lambda_A N = -120$, and $\Lambda_B N = -115$ at both surfaces. Then we calculate the free energy per unit of area as a function of the film thickness for each number of cylinder layers. It helps us to find the equilibrium densities corresponding to a given parameter set of thickness h and lateral space λ of the thin film. We know that the free energy of the thin film not only depends on the thickness but also depends on the lateral distance (or characteristic wavelength λ). The comparison of the lateral spacing to that in the bulk gives us information about the direction in which the cylinder stretches, i.e., perpendicular or horizontal to the plane of the film. Therefore, we also minimize the free energy with respect to the lateral spacing for each thickness to obtain the optimal value of the inter-cylinder periodicity in lateral direction.

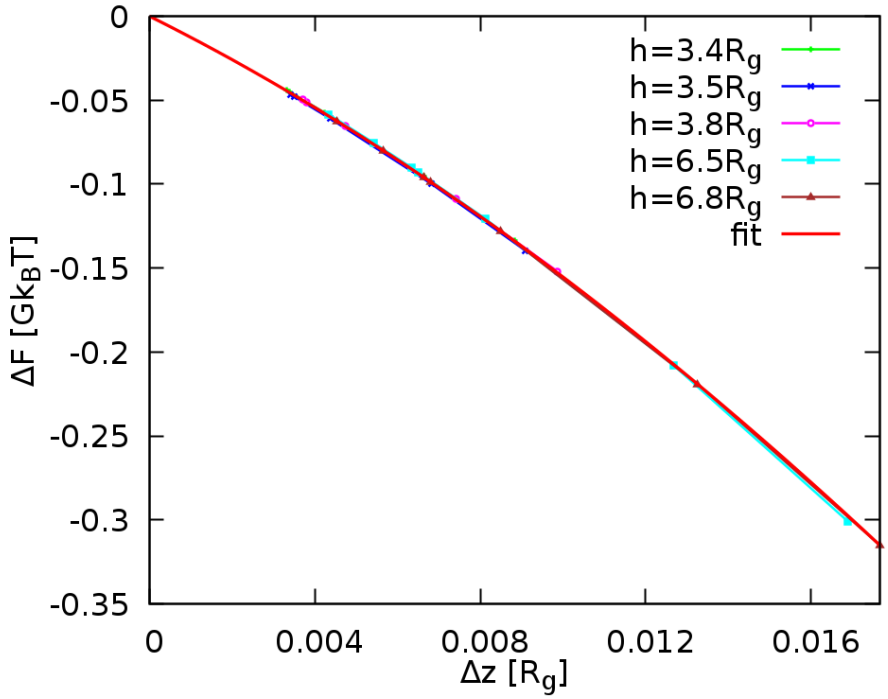

Figure 4.3: Shifted energy ΔF as a function of discretization Δz for different film thicknesses h with surface interactions $\Lambda_A N = -120$, $\Lambda_B N = -115$ and the chemical potential $\mu = (2.5 + \ln G) k_B T$. The solid line corresponds to the fit function $\Delta F(\Delta z) = -12.27\,\Delta z - 341\,\Delta z^2 + 1447\,\Delta z^3$.

The discretization in lateral and perpendicular direction with respect to the film (x and z, respectively), are chosen as $\Delta x \approx 0.05\,R_g$ and $\Delta z \leqslant 0.015\,R_g$ and the contour parameter s is discretized in steps of $\Delta s = 0.0001$ which is high

compared to other SCFT studies [75, 76]. Whereas most of these choices are not critical, we find that the discretization in the z direction has a significant influence on the resulting free energies, and even discretization errors could not be neglected. On the other hand, we also find that they lead to an energy shift ΔF which only depends on the discretization in the direction perpendicular to the plane of the thin film Δz and does not depend on the film thickness or the number of layers of cylinders in the film. Therefore, we studied the dependence of ΔF on Δz systematically for five different values of the film thickness. We calculate the shifted energy ΔF at different Δz which has a range from $\Delta z = 0.0033\, R_g$ to $\Delta z = 0.017\, R_g$. Afterwards, we fit the results to a third order polynomial, resulting in the estimate $\Delta F(\Delta z) = -12.27\,\Delta z - 341\,\Delta z^2 + 1447\,\Delta z^3$ and $\Delta F(\Delta z) = -12.41\,\Delta z - 318.5\,\Delta z^2 - 381\,\Delta z^3$, for the chemical potential $\mu = (2.5 + \ln G) k_B T$ and $\mu = (2.512 + \ln G) k_B T$, respectively. The energy shifts ΔF are presented in the figures 4.3 and 4.4. The fit functions describe adequately the regime of discretization $\Delta z \leqslant 0.015\, R_g$ explored here. These corrections are then applied to the SCF data shown in figures 4.7 and 4.8.

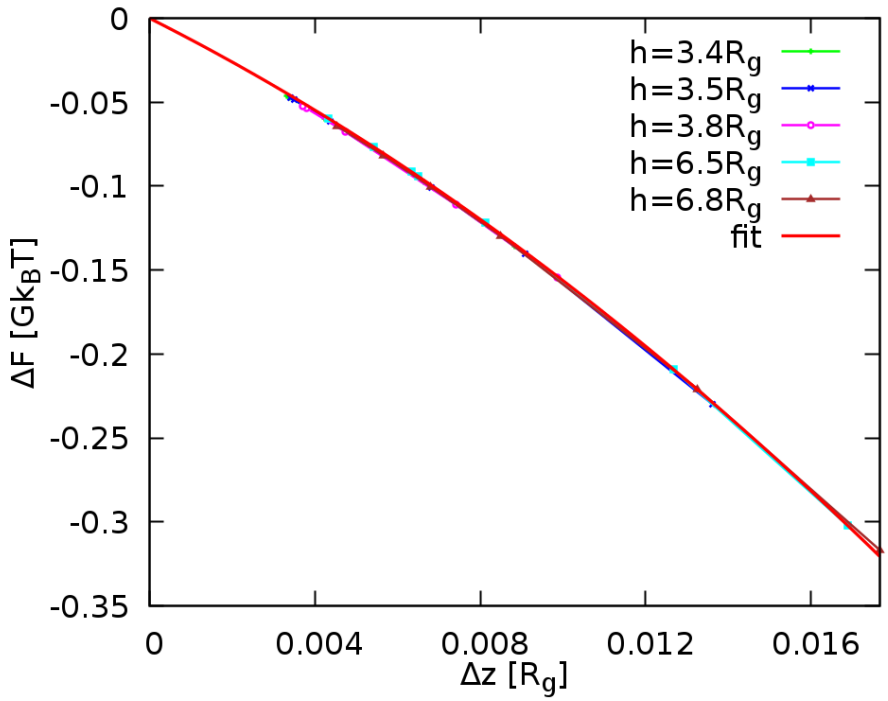

Figure 4.4: Shifted energy ΔF as a function of discretization Δz for different film thicknesses h with surface interactions $\Lambda_A N = -120$, $\Lambda_B N = -115$ and the chemical potential $\mu = (2.512 + \ln G) k_B T$. The solid line corresponds to the fit function $\Delta F(\Delta z) = -12.41\,\Delta z - 318.5\,\Delta z^2 - 381\,\Delta z^3$.

As discussed in the chapter 3, the pseudo-spectral method is usually more efficient to solve the modified diffusion equation when the block copolymers are confined in flat geometries. In the pseudo-spectral method, we have to switch back and forth between the real and Fourier spaces. For a given iteration step, though such a scheme takes longer computing time than the Crank-Nicolson method, yet it is highly accurate. We can choose larger values for discretiza-

tion in the contour variable s to compute the propagators $q(\mathbf{r}, s)$ with a given numerical accuracy. However, even with pseudo-spectral method, there are systematic discretization errors arising due to the strong surface field. This is shown in figure 4.5. This makes pseudo-spectral method less advantageous in the current context, as we cannot choose higher discretization in the space and contour variables.

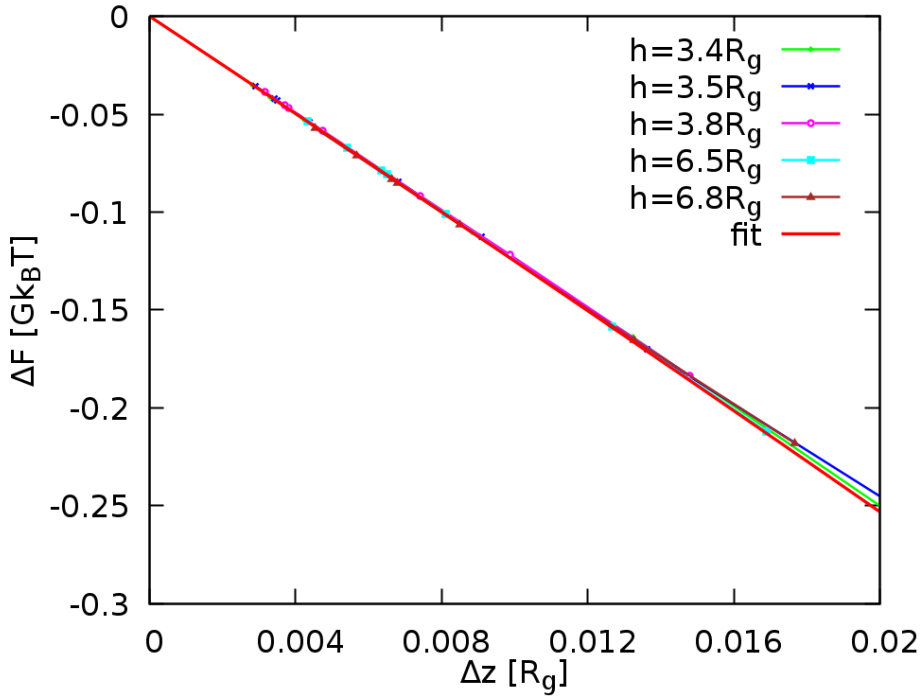

Figure 4.5: Shifted energy ΔF (using the pseudo-spectral method) as a function of discretization Δz for different film thicknesses h with surface interactions $\chi_A N = -120$, $\chi_B N = -115$ and the chemical potential $\mu = (2.5 + \ln G) k_B T$. The solid line corresponds to the fit function $\Delta F(\Delta z) = -12.38\,\Delta z - 11.4\,\Delta z^2 - 112\,\Delta z^3$.

Besides the free energy shift due to discretization errors, we also consider the effect of van der Waals (vdW) interaction on the free energy of the diblock copolymer films. We account for the vdW interaction through the Hamaker approach [77]. The vdW interaction energy per unit area takes the form:

$$W = \frac{-A}{12\pi h^2} \tag{4.10}$$

where h in equation 4.10 is the thickness of the diblock copolymer films, and A is nonretarded Hamaker constant which can be identified by the Lifshitz theory [77]. For example, we have a system consisting of three components as shown in figure 4.6. The Hamaker constant of the whole system is determined as:

$$A_{132} \approx (\sqrt{A_{11}} - \sqrt{A_{33}})(\sqrt{A_{22}} - \sqrt{A_{33}}) \tag{4.11}$$

The value of the Hamaker constant depends on the material of the systems. Typical values for the Hamaker constants of condensed phases are about

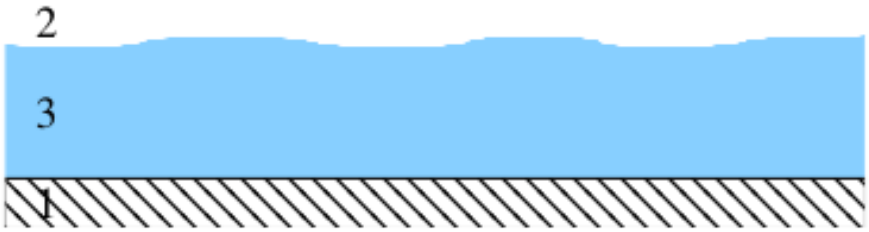

Figure 4.6: Sketch of a 3-component system characterized by a Hamaker constant A_{132}, for example copolymer (3) confined between substrate (1) and air interface (2).

10^{-19}J for interactions across vacuum [77]. The system studied in this thesis is similar to the experimental system investigated by Vega et al. [78], where they studied cylinder-forming of diblock copolymer PS-PHMA. The copolymer was deposited on the Si substrate and the air interface. Therefore, the Hamaker constant is chosen as $A \approx -4.87 \cdot 10^{-20}$ J, which is adapted from the work of Meli et al. [79]. Since the free energy obtained from the SCFT calculations is expressed in the units of Gk_BT, we convert the Hamaker constant as well into the units of Gk_BT. At room temperature, $1\,k_BT = 0.414 \cdot 10^{-20}$ J, then the Hamaker constant $A = -4.87 \cdot 10^{-20}J = -11.7\,k_BT$. To convert the Hamaker constant into the units of Gk_BT, we need to calculate the value of G, the Ginzburg parameter. We have

$$G = \frac{\rho_0}{N} R_g^3 \tag{4.12}$$

Matching the value of the spacing distance between cylinders from the SCFT calculation and the experimental results, we can identify $R_g \approx 5.8$ nm [80, 81]. We assume an average copolymer density of $\rho_m \approx 0.861$ g/cm^3 and the molecular weight of diblock copolymer PS-PEP, $M = 17500$g/mol. Thus the value of the Ginzburg parameter is:

$$G = \frac{\rho_0}{N} R_g^3 = \frac{\rho_m}{M} \cdot (6.02 \cdot 10^{23}) R_g^3 \approx 5.77 \tag{4.13}$$

Then the Hamaker constant of the diblock copolymer films is $A = -2.03\,Gk_BT$. This value of A results in the vdW interactions which are about $0.0005 - 0.004\,Gk_BT$ for multilayer thin films considered in this chapter. Such value of the vdW interaction is very small when compared to the other contributions to the SCFT free energy. Hence, it can safely be neglected.

4.2 RESULTS

The calculations are done in the grand canonical ensemble, i.e., the chemical potential μ of the copolymers is kept fixed and their number adjusts to the film thickness. The film thickness here is in the range of $[2-12]R_g$. In order to analyze the stability of the cylinder-forming multilayer films, we examine the free energy landscape of the films. SCFT calculations help us to seek minima in the free energy landscape of multilayer thin films that are physically realizable. Figure 4.7 shows an example of a Gibbs free energy landscape as a function of the film thickness h. At each value of the film thickness, the free energy per area is the one at the preferred value of the lateral distance λ, or in other words, it was already minimized with respect to the λ. The free energy landscape exhibits a series of minima, corresponding to monolayer, bilayer, and trilayer of cylinder mesostructures. The free energy per area at the minima depends on the value of the chemical potential μ. Here, the value of the chemical potential is fixed at, $\mu = (2.5 + \ln G)k_BT$ (G is the dimensionless Ginzburg parameter), was chosen slightly below the value where the film becomes macroscopically thick $\mu^* = (2.56 + \ln G)k_BT$ (figure 4.9). It is observed that the minimum corresponding to the monolayer state is a global minimum. Therefore, the monolayer of cylinders is globally stable, whereas the bilayer and trilayer of cylinders are the metastable states since their free energy minima are local minima.

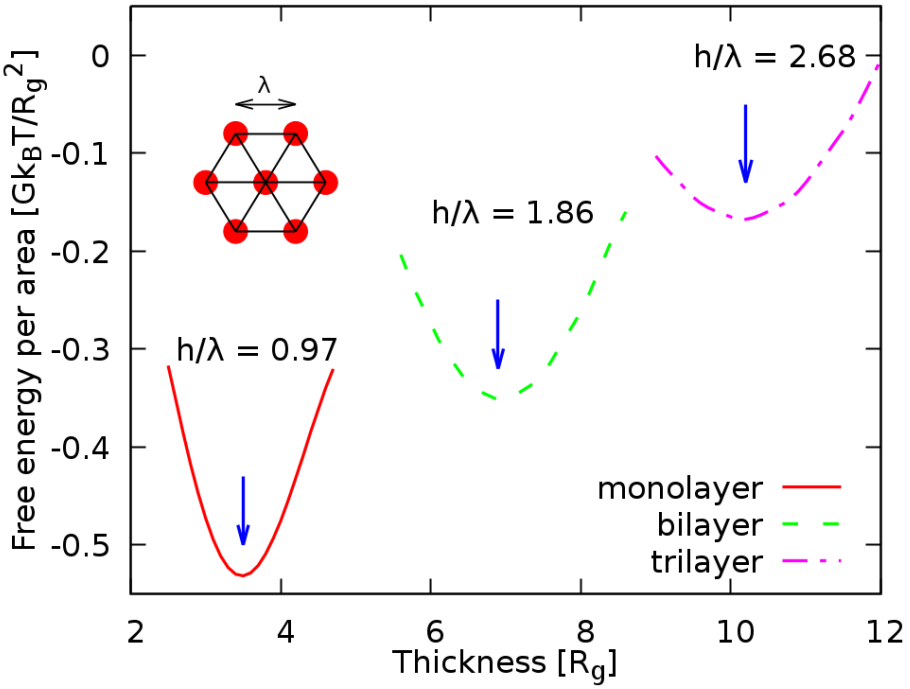

Figure 4.7: Grand canonical free energy per area in units of Gk_BT/R_g^2 as a function of the film thickness in units of R_g for a cylinder-forming diblock copolymer multilayer confined between two surfaces at copolymer chemical potential $\mu = (2.5 + \ln G)k_BT$. The optimum thickness of the thin film is the one corresponding to the free energy minimum and is indicated by the arrows.

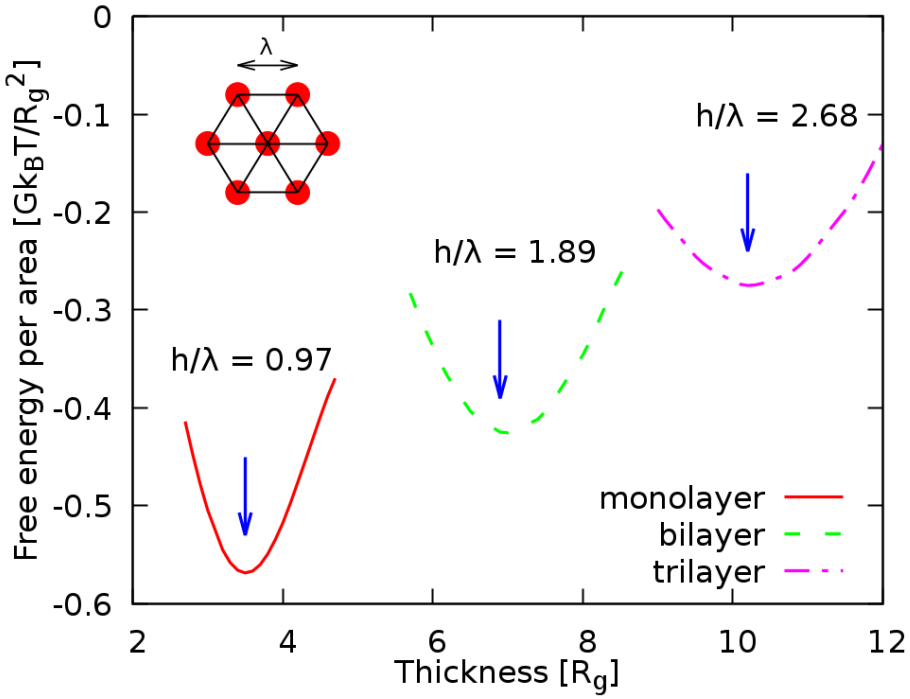

Figure 4.8: Grand canonical free energy per area in units of Gk_BT/R_g^2 as a function of film thickness in units of R_g for a cylinder-forming diblock copolymer multilayer confined between two surfaces at copolymer chemical potential $\mu = (2.512 + \ln G)k_BT$. The optimum thickness of the thin film corresponds to the free energy minimum and is indicated by the arrows.

If one increases the chemical potential, the free energy minima corresponding to multilayers move down relative to the monolayer minimum. It means that the free energy difference of the bilayer and trilayer compared to the monolayer are reduced. However, the bilayer state remains metastable for all $\mu < \mu^*$. For example, if we slightly increase the chemical potential to $\mu = (2.512 + \ln G)k_BT$, the free energy per area as a function of film thickness, which is similar to one in figure 4.7, is presented in figure 4.8. It also has a series of free energy minima corresponding to different numbers of layers of cylinders. The monolayer is still a global state and the bilayer and trilayer remain metastable states. In addition, we find that the free energy difference at the minima of bilayer/monolayer films and trilayer/monolayer films decreases compared to that corresponding to the chemical potential $\mu = (2.5 + \ln G)k_BT$. The value of minimum-energy difference between the bilayer and trilayer films compared to the monolayer films at the chemical potential $\mu = (2.5 + \ln G)k_BT$ are

$$\begin{cases} \Delta F_{21} &= F_2 - F_1 = 0.18\, Gk_BT/R_g^2 \\ \Delta F_{31} &= F_3 - F_1 = 0.36\, Gk_BT/R_g^2 \end{cases}$$

while they are slightly smaller at the chemical potential $\mu = (2.512 + \ln G)k_BT$

$$\begin{cases} \Delta F_{21} &= F_2 - F_1 = 0.14\, Gk_BT/R_g^2 \\ \Delta F_{31} &= F_3 - F_1 = 0.29\, Gk_BT/R_g^2 \end{cases}$$

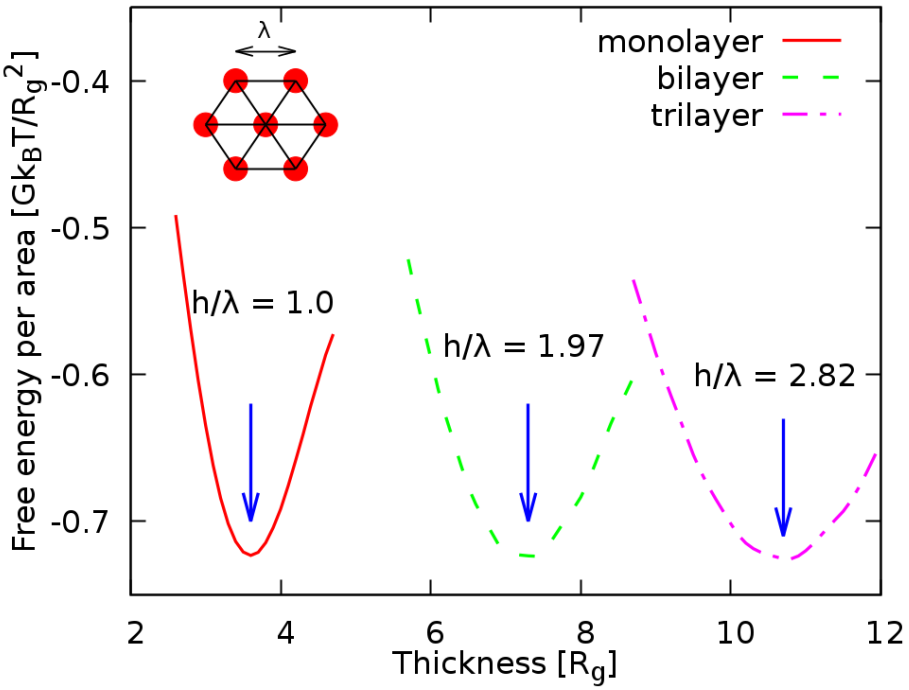

Figure 4.9: Grand canonical free energy per area in units of Gk_BT/R_g^2 as a function of film thickness in units of R_g for a cylinder-forming diblock copolymer multilayer confined between two surfaces. The copolymer chemical potential is fixed at $\mu^* = (2.56 + \ln G)k_BT$, where the film becomes macroscopically thick. The optimum thickness of the thin film corresponds to the free energy minimum and is indicated by the arrows.

As mentioned above, the chemical potential when the film becomes macroscopically thick is $\mu^* = (2.56 + \ln G)k_BT$. We present the Gibbs free energy landscape at the chemical potential μ^* as a function of the film thickness in figure 4.9, which is similar to those in figure 4.7 and 4.8. It also exhibits a series of free energy minima corresponding to different numbers of layers of cylinders. The minimum corresponding to the monolayer is not a global minimum any more. Instead, the free energy minima of bilayer and trilayer films have the same value as that of the monolayer system. This indicates that the film makes a transition to the macroscopically thick state.

In equilibrium, each number n of layers of cylinders will have an optimum thickness, which is determined by the balance of different factors, for example, the enthalpic, entropic energy and the surface interaction energy. The local film thickness has a strong influence on the resulting morphologies, therefore, we also analyze the behavior of the optimum thickness of the thin film here. We find that the optimal thickness h which corresponds to the minimum of

free energy per area, is $h_{1L} = 3.5R_g$ for the monolayer, while for the bilayer and trilayer it becomes $h_{2L} = 6.9R_g$, $h_{3L} = 10.2R_g$, respectively. The multilayer forms a hexagonal close-packed array of cylinders, as demonstrated in figures 4.7 and 4.8. However, it is not a perfect hexagonal lattice as in the bulk phase. It is deformed in response to the confinement in the thin film [82]. Then, for this system the ratios of the film thickness between bilayer and trilayer to monolayer are $h_{2L}/h_{1L} \sim 1.97$ and $h_{3L}/h_{1L} \sim 2.91$, respectively. The optimal thickness of the bilayer we find here is in excellent agreement with experimental results of Abate et al. [80], where it was found to be twice the thickness of the individual layers. Therefore, one can expect that a bilayer system with $h_{2L}/h_{1L} \sim 2$ should be relatively stable towards the development of holes or islands even during long periods of thermal annealing.

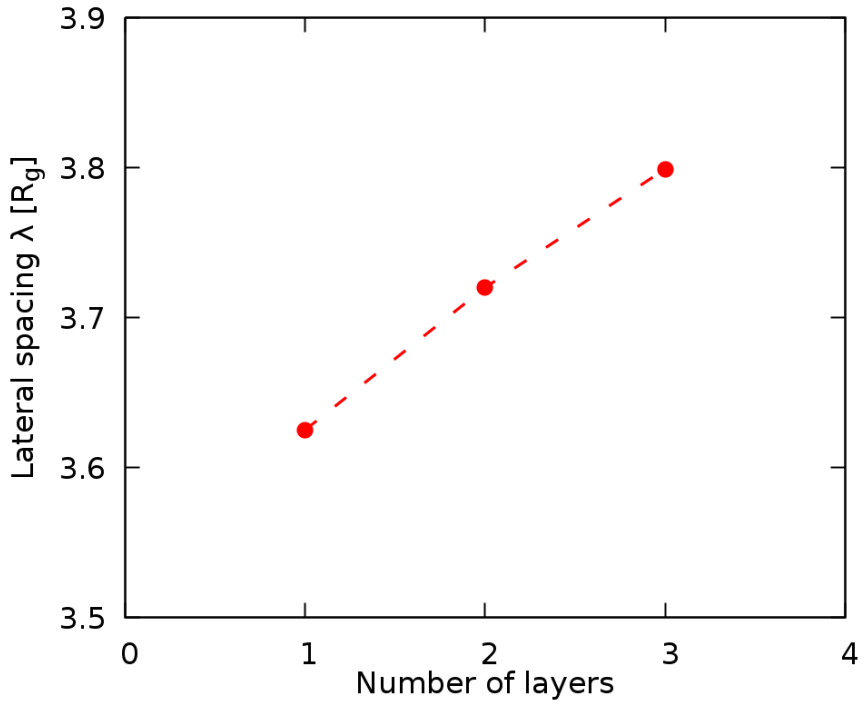

Figure 4.10: The lateral cylinder spacing at the optimum thickness (the characteristic distance between cylinders) is plotted as a function of the number of layers. The horizontal axis corresponds to an integer number of cylinder layers. The copolymer chemical potential is fixed at $\mu = (2.5 + \ln G)k_BT$.

Further, we find that the lateral spacing between neighboring cylinders at the optimal thickness systematically increases as the thin film thickness increases from n to $(n+1)$ layers of cylinders. Figure 4.10 shows this effect. Namely, for the monolayer, bilayer and trilayer systems the optimum inter-cylinder spacing in lateral direction at the energy-minimum thicknesses are, respectively, $\lambda_1 \sim 3.6R_g$, $\lambda_2 \sim 3.7R_g$, and $\lambda_3 \sim 3.8R_g$. For this system, the bulk inter-cylinder spacing is $\lambda \sim 3.7R_g$. Thus, we have $\lambda_1/\lambda \sim 0.97$ for the monolayer, $\lambda_2/\lambda = 1$ for the bilayer, and $\lambda_3/\lambda \sim 1.03$ for the trilayer. The data show that the average lateral distance between cylinders in thin film at the energetically favored thickness deviates from λ in bulk due to the geometrical constraint and the

lateral spacing of monolayer is the smallest and even smaller than that in bulk. It indicates that the monolayer of cylinders is stretched perpendicular to the plane of the film compared to the equivalent bulk structure. The data is also in good agreement with that reported by Knoll et al. for a cylinder-forming diblock and triblock copolymer multilayer [82]. They qualitatively studied the lateral distance of cylinder-forming in the thin film. These authors employed a solvent annealing technique to induce order in the diblock copolymer and then they used scanning force microscopy (SFM) to analyze the structure of the films. Afterwards, they compared the results with the theory based on the strong segregation theory (SST) calculation. They considered up to five-layer-thick films. They also found that in the thin films the unit cell is stretched perpendicular to the film plane, and that the lateral spacing is smaller than those in bulk [82]. Similar to the results shown here, they also observed a systematic variation of the characteristic distances between the cylinders as the film thickness increases from n to $(n+1)$ layers of cylinders [82]. Furthermore, they showed that the differences in the lateral spacings in the adjacent number of layers of cylinders vanish in the fourth layer. Although here we also simulated systems containing tetra-layer of cylinders, the results for the free energy are not reported because the discretization Δz does not belong to the reliable fitting regime. However, the discretization errors may not affect the results of lateral spacings. In addition, we also found that the lateral distance of a tetra-layer of cylinders is $\lambda_4 = 3.8R_g$, which is the same compared to the trilayer of cylinders films. Thus the effect of difference in the lateral distance between n and $(n+1)$ layers disappears in tetra-layer of cylinders films, which is also in agreement with the data in the literature [82].

The density profile of multilayer cylinders of the thin film at the optimum thickness is plotted in figure 4.11. This figure shows the characteristic profiles of the diblock copolymers at the optimum values of the thickness (local minima in figure 4.7) obtained through SCFT calculations. We observe that in the monolayer films the cylinders are not circular but elliptical, in the bilayer films the cylinders becomes more circular. If the number of layers increases, the cylinders become more circular since the confining effect is spread over a larger number of diblock copolymers. For example, in the trilayer films the cylinders are more circular than in the bilayer films. Namely, two layers of cylinders at the surfaces are more circular compared to cylinders in monolayer and bilayer thin films and the cylinders in the middle thin films are circular.

As mentioned above, we minimize the free energy per area not only with respect to the thickness but also to the characteristic wavelength and we just discussed the behavior of the inter-cylinder spacing at the optimum thicknesses of different layers of cylinders. It is also interesting to study how the lateral spacing behaves when we vary the film thickness and it is still in the range of n layers. Figure 4.12 presents the lateral spacing as a function of the film thickness.

When the thickness of a layer is far below the optimal thickness, the block copolymer thin film is strongly compressed. It causes a cost of increasing the compressing energy between two blocks A and B. The data in figure 4.12 indicate that the lateral distance increases compared to that at the optimal thick-

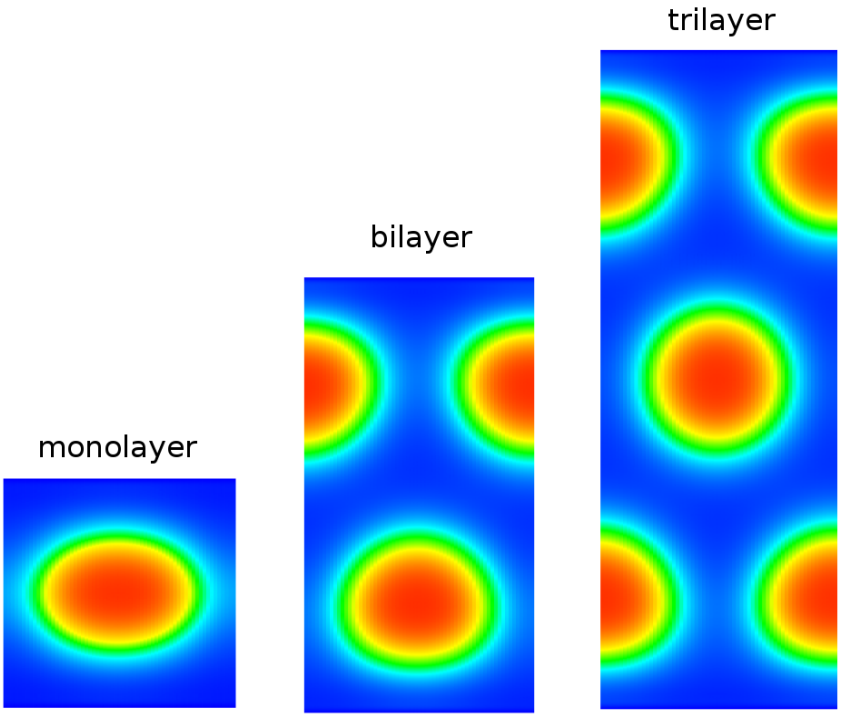

Figure 4.11: Density profiles of a monolayer, a bilayer and a trilayer diblock copolymer thin film at the corresponding optimum thicknesses: $h_{1L} = 3.5\,R_g$, $h_{2L} = 6.9\,R_g$ and $h_{3L} = 10.2\,R_g$. The chemical potential is $\mu = (2.5 + \ln G)k_BT$.

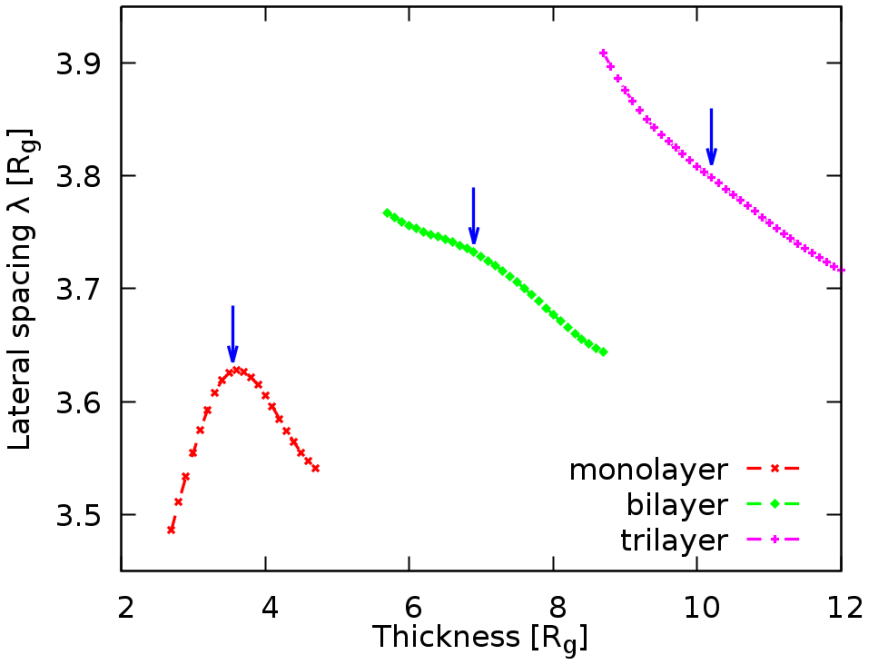

Figure 4.12: The lateral cylinder spacing (the characteristic distance between cylinders) is plotted as a function of the film thickness. The blue arrows indicate the optimum thicknesses of the thin films. The copolymer chemical potential is fixed at $\mu = (2.5 + \ln G)k_BT$.

ness in the bilayer and trilayer films. For example, $\lambda_2 = 3.8R_g$ at the thickness $h_2 = 5.6R_g$ while it is $3.7R_g$ at the optimal thickness of bilayer; and $\lambda_3 = 3.9R_g$ at the thickness $h_3 = 9.0R_g$ while it is $3.8R_g$ at the optimal thickness of trilayer. However, it is different in the monolayer thin films. When the thickness is far below the optimum thickness of the monolayer, the lateral spacing slightly decreases. For instance, at the thickness $h_1 = 2.5\,R_g$, the lateral distance is $\lambda_1 = 3.5\,R_g$ (figure 4.12). This happens because the number of block copolymers becomes smaller when the film is so thin.

In order to have a clear view on how much the structures of diblock copolymer films deform compared to that at the optimum thicknesses, we present the density profiles of multilayer compressed thin films in figure 4.13. It is obvious that the block copolymer cylinders are more compressed than in figure 4.11, and that the cylinders become more squeezed ellipses in the monolayer. The same happens for the cylinders at surfaces of bilayer and trilayer films. However, the degree of compression is less than in the monolayer since it is distributed over a larger number of block copolymers.

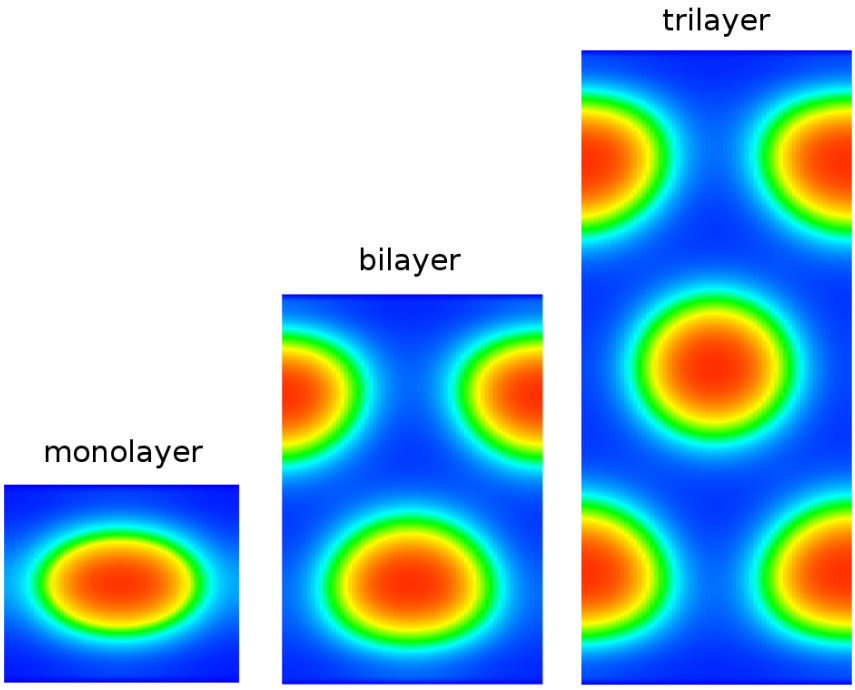

Figure 4.13: Density profiles of a monolayer, a bilayer and a trilayer diblock copolymer thin films at the thicknesses smaller than the corresponding optimum thicknesses: $h_1 = 2.9\,R_g$, $h_2 = 5.6\,R_g$ and $h_3 = 9.0\,R_g$. The copolymer chemical potential is fixed at $\mu = (2.5 + \ln G)k_BT$.

In contrast, when the thickness is increased further above the optimal thickness of n layers, the thin film is stretched perpendicularly to the substrates. As a result, the lateral distance will decrease compared to that at the regime near the optimal thickness (figure 4.12). For instance, the lateral spacing is $\lambda_1 = 3.5R_g$ at the thickness $h_1 = 4.7R_g$ while it is $3.6R_g$ at the optimal thickness of the monolayer films; and $\lambda_2 = 3.6R_g$ at the thickness $h_2 = 8.6R_g$ while

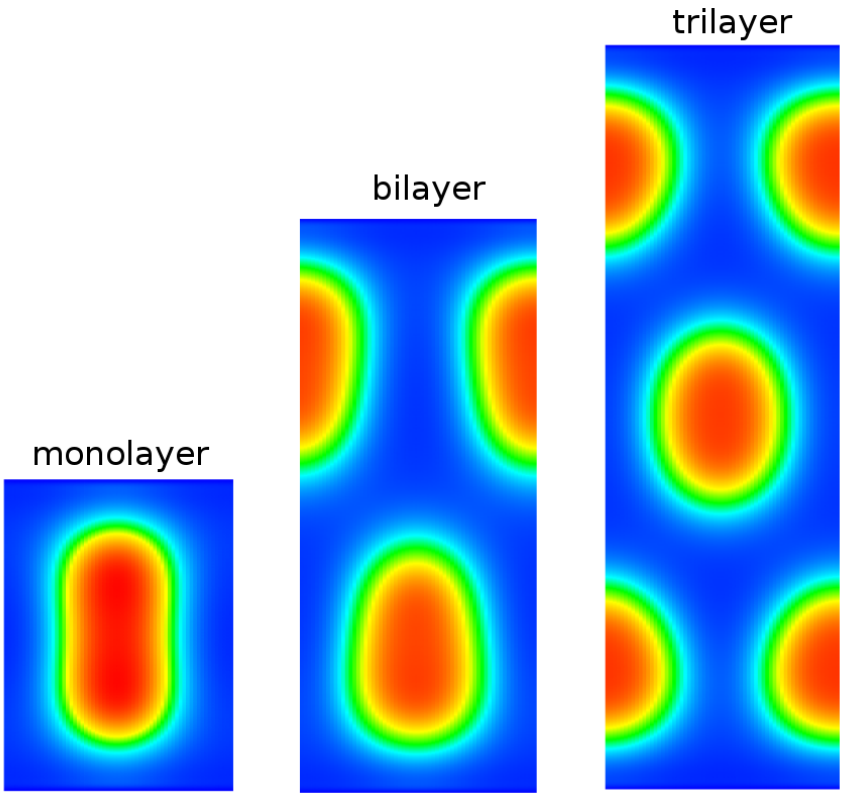

Figure 4.14: Density profiles of a monolayer, a bilayer and a trilayer diblock copolymer thin films at the thicknesses higher than the corresponding optimum thicknesses: $h_1 = 4.7\,R_g$, $h_2 = 8.6\,R_g$ and $h_3 = 11.6\,R_g$. The copolymer chemical potential is fixed at $\mu = (2.5 + \ln G)k_B T$.

it is $3.7R_g$ at the optimal thickness of the bilayer films; and $\lambda_3 = 3.7R_g$ at the thickness $h_3 = 11.6R_g$ while it is $3.8R_g$ at the optimal thickness of the trilayer films. Figure 4.14 shows the density profile of the monolayer, bilayer and trilayer thin films. It is similar to the plots in figure 4.11 and figure 4.13, but at the different thicknesses $h_1 = 4.7R_g, h_2 = 8.6R_g$ and $h_3 = 11.6R_g$, which are larger than the optimal ones. It is clear that the diblock copolymers are elongated perpendicularly to the substrates compared to the density profile of multilayers of thin films at optimal thickness in figure 4.11. Moreover, from the density profile we also observe that the degree of stretching decreases as the number of layers increases. The reason is the stretching is distributed among a larger number of unit cells. For example, cylinders in the trilayer films are less stretched than that in the bilayer films.

Note that the change of lateral distance is small but noticeable as the thin film thickness varies either to higher or smaller values than the energetically favored one and the number of layers remains the same. These results excellently agree with observation in reference [82]. They reported the relationship between the lateral spacing and the local thin fims as well. When the local film thickness increases above n layers, the lateral distance firstly decreases. Then the distance increases abruptly as the stretching energy is greater than the energy needed to accomodate an additional layer of cylinders, to $(n + 1)$ layers.

If the thickness is continuously increased to approach the optimum thickness of $(n+1)$ layers, the lateral distance will relax to its favored value.

From the results we should note that the global equilibrium structure for this diblock copolymer system is the one where a monolayer film coexists with islands of thick multilayer films. This state is not reached on experimental time scales [80]. However, we expect the upper layers, i.e., the second and the third layers, to interact with the first layer to facilitate the penetration of chains such that the cylinders in the second (third) layer can accomodate the local structure of the first layer. The density profiles in figure 4.11 show that the structure of the cylinders changes from squeezed ellipsoids in the monolayer to more circular in the bilayer and trilayer. It is also noted that the layers near the surfaces deform more than the ones located inside of the thin film. In the bulk, cylinders are fully circular. Hence the addition of the second layer slightly changes the structure of the first layer, and this interaction provides a mechanism how a pre-aligned first layer can help to order the upper layers, i.e., the second and the third layers. This helps to minimize the density of defects in thin films which are one of the main problems of the self-assembly of block copolymers.

The coupling mechanism between the lower and the upper layers discussed above, is also observed in the experiments conducted by Abate et al. [80]. They studied cylinder-forming of diblock copolymers PS-PHMA films. First, they used shear alignment to order cylinders parallel to the substrate of bottom layer. Then they put the second layer of diblock copolymers on the top. The stack of the two layers of cylinders, where the thickness is twice that of the monolayer was thermally treated at different annealing times under vacuum at 150°C. They investigated the coupling between the bottom aligned layer and the nonaligned upper layer. Figure 4.15 shows the block copolymer stack prior to thermal annealing.

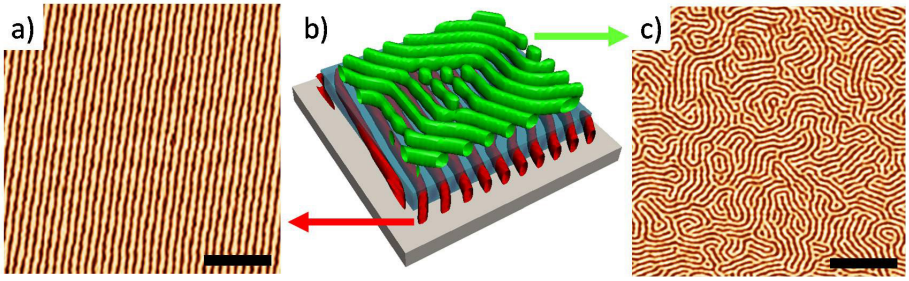

Figure 4.15: The PS-PHMA diblock copolymer film before thermal annealing: Panel a) Atomic force microscopy (AFM) phase image of shear-aligned cylinder-forming of bottom layer, panel b) schematic of bilayer film, where the nonaligned cylinders rest on a shear-aligned bottom layer, and panel c) AFM of nonaligned second layer with many defects [80].

They used atomic force microscopy (AFM) to image the structure of the thin film and observed nice results. Before annealing, there are typical topological defects that appear in diblock copolymer system, particularly in the nona-

ligned upper layer of the thin film (see the panel c) in figure 4.15). For instance, $\pm 1/2$ disclinations are highly energetic cost and destroy the orientational order; and dislocations break the translational order. During the annealing procedure, the interaction between bottom shear-aligned layer and top nonaligned layer drives the annihilation of the defects and promotes the connectivity between cylinders. The layers are competing with each other to impose a local orientation. As a result, the density of dislocations is reduced and the orientational and translational order of the upper layer are improved. In figure 4.16 it is easy to see that there are many defects and the order of the upper layer is very poor after 2 h of annealing (panel a), but the order of the upper layer is already improved in panel b) after 6 h of annealing. If the diblock copolymer system is annealed during 24 h, the second layer adjusts the orientation of the bottom layer and induces the complete annihilition of the topological defects as shown in panel d) [80].

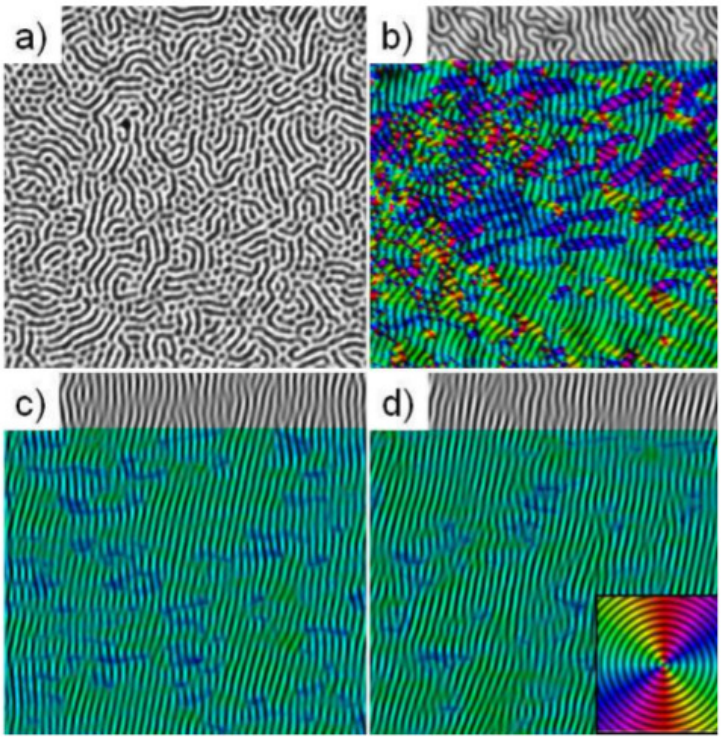

Figure 4.16: Atomic force microscopy (AFM) phase image for block copolymer thin films deposited onto a preordered layer of cylinders with the same structure. The image shows the second layer after annealing at 150°C in vacuum at different times: $t = 2\,h$ (panel a), $t = 6\,h$ (panel b), $t = 16\,h$ (panel c) and $t = 24\,h$ (panel d). The order of the second layer is improved during thermally annealing. This figure is adapted from ref. [80].

Another work by Rahman et al. also showed the interaction mechanism between layers in order to align block copolymer films [83]. They studied multilayers of diblock copolymer PS-b-PMMA films. They found that each copolymer layer acts as a structural factor of the final morphology and a guiding field to order the subsequent layers. Specifically, the second layer does not order independently from the first one. They proposed a responsive layering

mechanism, that the second layer tends to maximize the overlap interface with the first layer during ordering process. Besides the role as a template for directing the order of the upper layers, the first layer also influences the defects of the upper ones. The second layer inherits defects from the first layer; that means, any defects in the first layer will disturb the preferred local motif, introducing a defect in the second layer [83]. Moreover, they obtained new and more complicated morphologies as reported in some other studies [76, 84–87]. These morphologies are hybrid between parallel and perpendicular cylinders, parallel cylinder and perforated lamellae (CP), parallel cylinder and lamellae (CL). It depends on the interplay of selectivity of surface fields for the blocks and the mismatch between the film thickness and the integer number of the natural size of single cylinder layer. For example, when the surfaces are neutral for both blocks A and B, and the film thickness is not an integer number of monolayer periodicity (i.e., $h = (n + 1/2)h_0$), block copolymer films can form complicated strutucres. We do not observe these structures here since our film systems were analyzed in two dimensions, where these symmetries cannot be observed.

4.3 CONCLUSIONS

By using SCFT, we have studied the directed self-assembly of cylinder-forming diblock copolymer thin films confined between two planar surfaces, the substrate and free surface (air interface). Both surfaces selectively attract the majority block (A) to create a wetting layer. A systematic analysis has been done to gain a fundamental understanding to produce ordered diblock copolymer nanostructures. We minimize the free energy per area with respect to the film thickness and the characteristic wavelength in the lateral direction. We can, therefore, determine the optimal conditions of the film thickness and lateral spacing for each number of layers of cylinders. The results indicate that the film thickness is an important control parameter in morphologies of block copolymer films. The global equilibrium state of this diblock copolymer films is a monolayer coexisting with islands or holes of thicker films. We find characteristic behaviour of the lateral spacing as a function of local thickness in each number of layers of cylinders and also as a function of the overall film thickness in different number of layers of cylinders. The stretching of monolayer films relative to the corresponding structure in bulk is in excellent agreement with experiments. More interestingly, we also discover the interaction mechanism of the upper layers and the bottom one. Via this mechanism the bottom layer acts as a periodic external field that stabilizes and dictates the orientation of upper layers. It leads to a sharing of orientations between layers. By this coupling, the density of defects is reduced to get well-ordered structures, it can be obtained through the thermally annealing. Our results demonstrate that it is possible to propagate well-ordered structures in thick block copolymers with appropriate control over a single self-assembling polymeric layer to template successive layers and enhance the long-range order.

5

ORIENTATIONAL PHASE TRANSITION OF DIBLOCK COPOLYMER THIN FILMS

In the bulk, the copolymer structures are mainly determined by the ratio of the block lengths f and the interaction between the different blocks χN. For example, with the right values of f and χN, block copolymers form a hexagonal lattice of cylinders. However, it is different and more complicated in thin films, where we have additional constraints, such as forces from the air-polymer interface and the film-substrate interface, which influence the structure formation. Typically, as we discussed in the previous chapter, the thickness plays an important role in determining the morphologies of block copolymer thin films. There are many experiments and computer simulation studies [32–34, 76, 88] suggesting that the equilibrium phase behaviour of the confined block copolymer films is controlled by two important factors: the degree of preferential attraction of block copolymers to the surface of thin film and the mismatch between the film thickness and the natural thickness of a single layer of cylinders oriented parallel to the film plane. The latter factor is known as commensurability effect. In the thin films, when the film thickness is not an integer number of the thickness of one layer of parallel cylinders, instead of parallel cylinder configuration, the copolymer films tend to form islands and holes to accommodate additional materials or form other configurations, such as perpendicular cylinders [89]. For symmetric and weak surface fields, parallel cylinders were found to be stable. Increasing the strength of the surface fields results in perforated lamellae (PL) or lamellae (L). For asymmetric surface fields, the situation is more complex. Here, parallel and perpendicular configurations can coexist [34]. It is very interesting to study phase transitions between the various phases of block copolymer fluids under the change of certain conditions, such as the thickness or the surface fields. Such a phase transition study is expected to provide a fundamental understanding of the structure formation in copolymer fluids. Therefore, we can contribute a notable impact on nanotechnology, as discussed before. These ordered fluids are facinating materials and have an essential role in technologies as well as in the biological cells researches [18, 90].

Different experimental and simulation studies [86, 91–93] reported the formation of perpendicularly oriented cylinder ($C_\perp$) and perforated lamellae (PL), when the thin film thickness was below the optimum thickness of monolayer. For example, Knoll al et. [91] showed that there is a phase transition $C_{||} \rightarrow C_\perp$ when the surface interaction is not too strong, and the sequence of phase transitions $C_{||} \rightarrow PL \rightarrow C_\perp$ with strong surface interaction. The schematic of phase diagram studied by both simulations and experiments is presented in the figure 5.1. In addition to these phases, there are other morphologies, such as lamellae, undulated cylinders, undulated lamellae and hybrid structures [86]. These phases are also stable under particular conditions of the thin film

thickness and the interactions between copolymers and substrates.

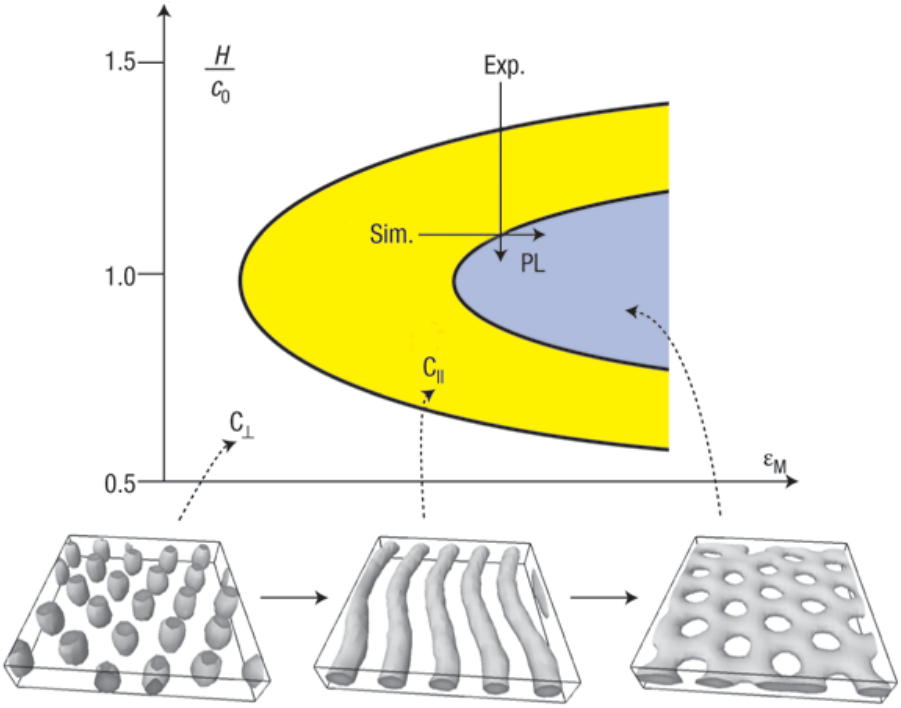

Figure 5.1: Schematic phase diagram of a copolymer thin film. It is a function of the film thickness H, which is in units of the thickness of a monolayer of cylinders c_0, and the strength of interaction between the block copolymers and the surface of the film ϵ_M. The phase diagram was studied in both, computer simulations (Sim.) and experiment (Exp.). This figure is adapted from reference [91].

In the previous chapter, we discussed the phase transition from a monolayer to multilayer of cylindrical phases $C_{||}$, which are oriented parallel to the surface of substrates, where the monolayer of cylinders is a globally stable and the bilayer or trilayer of cylinders are metastable states. In thin films, as the film thickness is varied, cylinders can change their orientation to $C_{\perp}$, as described above, in order to minimize the free energy. In this chapter, we will mainly discuss the phase transition between cylindrical phases due to the influence of the film thickness. These cylindrical phases are cylinders which are oriented perpendicular to the substrate and the monolayer of cylinders which are oriented parallel to the substrates. The phase transition between them occurs as the film thickness is reduced below the periodicity of the monolayer of parallel cylinders. These two kinds of configurations are demonstrated in figure 5.2: panel a) shows the parallel configuration and panel b) shows the perpendicular configuration. Furthermore, we also vary the interactions between the block copolymers and the surfaces to analyze the phase behaviour of the thin films. Specifically, we investigate the change in the orientation of cylinders or the transition to other morphologies. We still employed the self-consistent field theory to obtain the density profile with the minimum free energy.

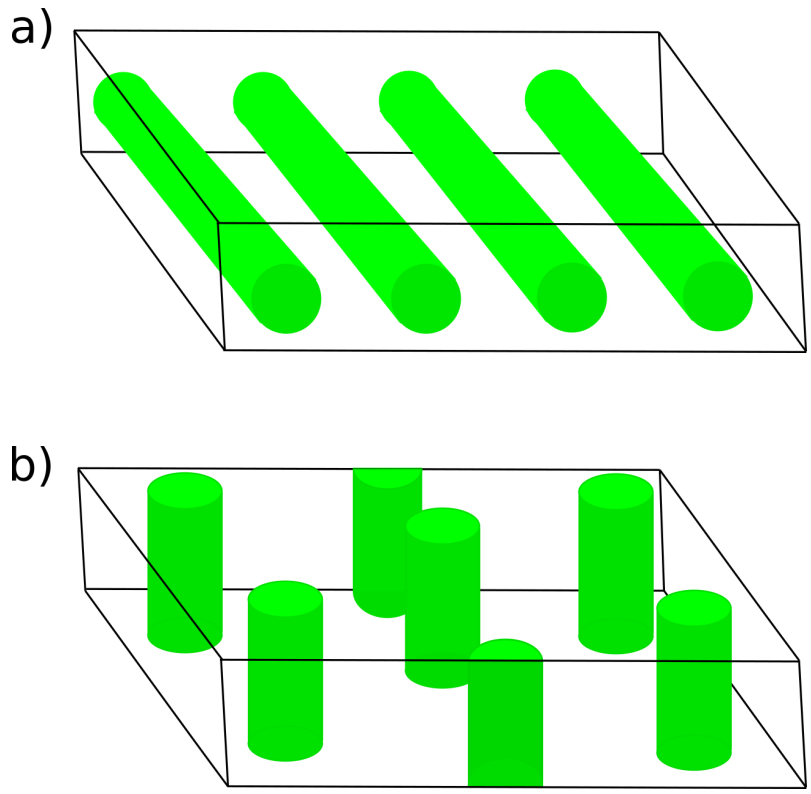

Figure 5.2: a)-Cylinders of block copolymers are oriented parallel to the surfaces; b)-Cylinders of block copolymers are oriented perpendicular to the surfaces. Green corresponds to B-block.

5.1 THEORY

We consider a melt of n asymmetric AB diblock copolymer molecules, where each molecule is modeled as an ideal Gaussian chain without nonbonded interactions [20] and is parameterized by a contour variable s that increases continuously from 0 to 1 along its length. The A and B segments have equal statistical length b. The diblock copolymers are confined between two flat surfaces, which are treated as two hard walls. The two surfaces preferentially attract the majority block (A) of the copolymers as in chapter 4. Here, we focus on the thickness range between zero and the thickness of a monolayer of cylinders. First, we study films of thickness h, that are constrained between two symmetric flat surfaces located at $z = 0$ and $z = h$. Here, symmetric surfaces means that the bottom substrate and the top surface have the same strength of interactions for each A or B block. We investigate the influence of the thickness on the microstructure of the films. Then, for completeness, we also consider the case where thin films are confined between two asymmetric surfaces, which have different degrees of preferential attraction of blocks to the surfaces. Periodic boundary conditions are applied in the other directions, namely, in the x- and y-direction. The strength of repulsion between the unlike blocks is controlled by the product χN, where χ is the Flory-Huggins parameter and N is polymerization degree. Here, we study intermediate segregation level, and the parameter values are chosen as $\chi N = 20$, and $f = 0.7$ being the volume frac-

tion of the A-block. As expected, a cylindrical phase is formed. The inverse compressibility parameter of the melt is chosen to be $\kappa N = 25$ for numerical reasons. The calculations are performed in the grand canonical ensemble, and the number of diblock copolymers is adjusted to the film thickness. The chemical potential of the copolymers is kept fixed at $\mu = (2.5 + \ln G)k_B T$. Here, G is the dimensionless Ginzburg parameter $G = \frac{\rho_0}{N} R_g^3$ (ρ_0 is the average monomer density).
Similar to the discussion in chapter 4, we employed the self-consistent field theory to study the self-assembly of patterns. It has been established in detail in the previous chapters, here we just briefly describe it. In its spirit the free energy of the diblock copolymer melt is given by:

$$\begin{aligned}\frac{F_{GC}}{k_B T} &= -e^{\mu} Q + \rho_0 \int d\mathbf{r} \left[\chi \phi_A(\mathbf{r})\phi_B(\mathbf{r}) + \frac{\kappa}{2}\left(\phi_A(\mathbf{r}) + \phi_B(\mathbf{r}) - 1\right)^2\right] \\ &\quad -\frac{\rho_0}{N}\int d\mathbf{r}\left[\omega_A(\mathbf{r})\phi_A(\mathbf{r}) + \omega_B(\mathbf{r})\phi_B(\mathbf{r})\right] \\ &\quad +\frac{\rho_0}{N}\int d\mathbf{r}\, H(\mathbf{r})\left[\Lambda_A N\, \phi_A(\mathbf{r}) + \Lambda_B N\, \phi_B(\mathbf{r})\right] \end{aligned} \tag{5.1}$$

where Λ_A, Λ_B are the strengths of the interaction between the A-block and B-block to the surfaces, respectively. $H(\mathbf{r})$ is the surface field defined as follows:

$$H(\mathbf{r}) = \begin{cases} (1 + \cos(\pi z/\epsilon)) & 0 \leqslant z \leqslant \epsilon \\ 0 & \epsilon \leqslant z \leqslant h - \epsilon \\ (1 + \cos(\pi(h - z)/\epsilon)) & h - \epsilon \leqslant z \leqslant h \end{cases} \tag{5.2}$$

The free energy of the system then will be expressed in units of $Gk_B T$.
The fields $\omega_A(\mathbf{r})$, $\omega_B(\mathbf{r})$ act on the A monomers and B monomers, respectively; and the densities of each segment are determined from the following SCF equations:

$$\omega_A(\mathbf{r}) = N\chi\phi_B(\mathbf{r}) + N\kappa\left[\phi_A(\mathbf{r}) + \phi_B(\mathbf{r}) - 1\right] + N\Lambda_A H(\mathbf{r}) \tag{5.3}$$

$$\omega_B(\mathbf{r}) = N\chi\phi_A(\mathbf{r}) + N\kappa\left[\phi_A(\mathbf{r}) + \phi_B(\mathbf{r}) - 1\right] + N\Lambda_B H(\mathbf{r}) \tag{5.4}$$

$$\phi_A(\mathbf{r}) = e^{\mu}\int_0^f ds\, q(\mathbf{r}, s) q^{\dagger}(\mathbf{r}, 1 - s) \tag{5.5}$$

$$\phi_B(\mathbf{r}) = e^{\mu}\int_f^1 ds\, q(\mathbf{r}, s) q^{\dagger}(\mathbf{r}, 1 - s) \tag{5.6}$$

We first study an effectively two-dimensional (2D) system for a single layer of parallel cylinders, which does not loose the general properties of the system in three dimensions. However, it requires to study three-dimensional (3D) systems for perpendicular cylinders because this configuration cannot be observed in two dimensions. Therefore, the Laplace operator in the modified diffusion equations for $q(\mathbf{r}, s)$ and $q^{\dagger}(\mathbf{r}, 1 - s)$ will take the form

$$\Delta = \frac{\partial^2}{\partial x^2} + \frac{\partial^2}{\partial z^2} \qquad \text{(for 2D)} \tag{5.7}$$

$$\Delta = \frac{\partial^2}{\partial x^2} + \frac{\partial^2}{\partial y^2} + \frac{\partial^2}{\partial z^2} \qquad \text{(for 3D)} \tag{5.8}$$

The modified diffusion equations in 2D- and 3D- systems are:

$$\frac{\partial q(x,z,s)}{\partial s} = \left(\frac{\partial^2}{\partial x^2} + \frac{\partial^2}{\partial z^2}\right) q(x,z,s) - \omega_\alpha q(x,z,s) \tag{5.9}$$

$$\frac{\partial q(x,y,z,s)}{\partial s} = \left(\frac{\partial^2}{\partial x^2} + \frac{\partial^2}{\partial y^2} + \frac{\partial^2}{\partial z^2}\right) q(x,y,z,s) - \omega_\alpha q(x,y,z,s) \tag{5.10}$$

The discretization in space is chosen as $\Delta z = 0.01\, R_g$ for either 2D or 3D films. In the lateral directions, x and y, the values are $\Delta x \approx 0.05\, R_g$ for 2D films, and $\Delta x \approx 0.05\, R_g$, $\Delta y \approx 0.1\, R_g$ for 3D films. The contour parameter s is discretized in steps of $\Delta s = 0.0001$ and $\Delta s = 0.0003$ for 2D and 3D films, respectively. The discretization here has a high resolution compared to other SCFT studies. These above discretization values in 2D and 3D systems are chosen such that these values are optimal to conduct calculations without influencing the free energies of stable morphologies. From the work presented in the last chapter, we know that most of these discretization choices are not critical, and the discretization in the z direction had a significant effect on the resulting free energies. Hence, the discretization errors could not be neglected. On the other hand, we also found that they lead to an energy shift ΔF, which only depends on the discretization in the direction perpendicular to the plane of the thin film, Δz, and does not depend on the film thickness. As in the previous chapter, we therefore study the dependence of ΔF on Δz systematically for five different values in the range of study of the film thickness. We calculate the shifted energy ΔF at different Δz, which has a range from $\Delta z = 0.0033\, R_g$ to $\Delta z = 0.017\, R_g$. Then we fit the results to a third order polynomial. We do the fit for individual set of surface interactions parameters. For example, with the symmetric surface interactions $\Lambda_A N = -120$ and $\Lambda_B N = -115$, the estimate for the fit function is $\Delta F(\Delta z) = -12.27\,\Delta z - 341\,\Delta z^2 + 1447\,\Delta z^3$. The corresponding data is shown in figure 5.3. For another example with asymmetric surface interactions, where $\Lambda_A N = -120$, $\Lambda_B N = -115$ at one surface and $\Lambda_A N = -95$, $\Lambda_B N = -90$ at the other surface, the fit function is $\Delta F(\Delta z) = -11.43\,\Delta z - 375\,\Delta z^2 + 7012\,\Delta z^3$. The corresponding data is displayed in figure 5.4. These corrections are then applied to the corresponding SCF data below.

As discussed in previous chapter, we also consider the effect of the long-range van der Waals (vdW) interaction on the free energy of the diblock copolymer films. The system studied in this thesis is similar to the experimental system investigated by Vega et al. [78]. They studied triblock copolymer polystyrene-block-polybutadiene-block-polystyrene (SBS) with an average molecular weight of $M \sim 140000$ g/mol. The copolymer was deposited on the Si substrate and the carbon dioxide CO_2 interface. As shown by Matsen and Thompson [94], the phase diagram of an ABA triblock is similar to that of an AB diblock with the same composition but with half of its molecular weight. Hence, our SCFT calculations investigate the phase behaviour of the diblock copolymers. To compute the van der Waals interaction for such a system, we take the value of M to be half that of the experimentally investigated system ($M \sim 70000$ g/mol). The Hamaker constant is chosen $A = -3 \cdot 10^{-20}$ J, which

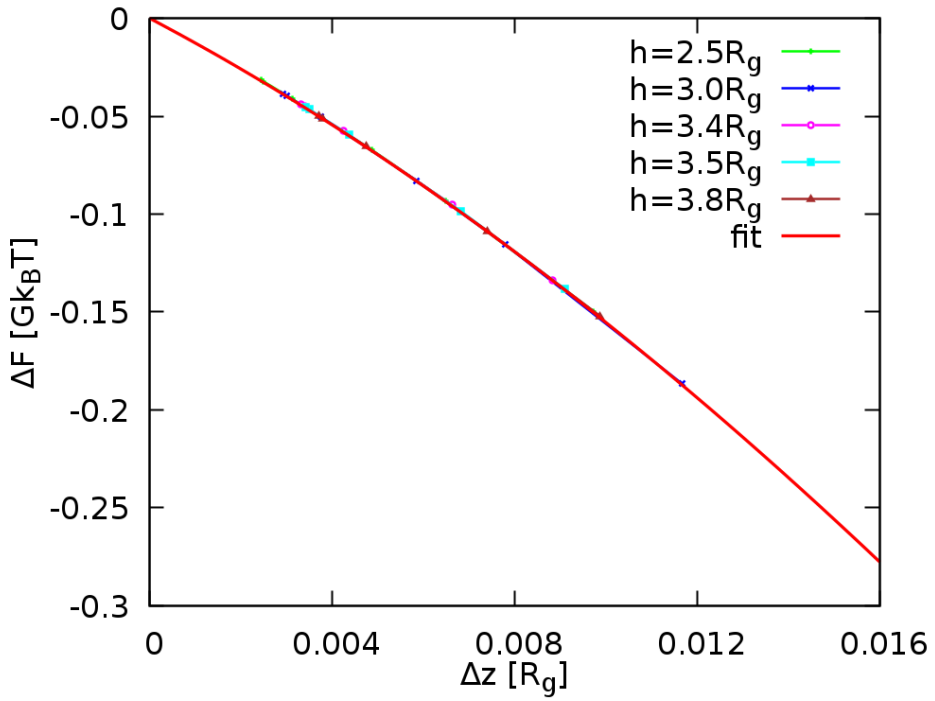

Figure 5.3: Shifted energy ΔF as a function of discretization Δz for different film thicknesses h with surface interactions $\Lambda_A N = -120$, $\Lambda_B N = -115$ and the chemical potential $\mu = (2.5 + \ln G)k_B T$. The solid line corresponds to the fit function, $\Delta F(\Delta z) = -12.27\,\Delta z - 341\,\Delta z^2 + 1447\,\Delta z^3$.

is the Hamaker constant of PS deposited on the Si substrate and CO_2 surface [79]. These values of M and A result in van der Waals interaction in the range of $[0.01 : 0.5]Gk_B T$. Since the value is significant when compared to the SCFT free energy, the van der Waals interaction cannot be neglected here.

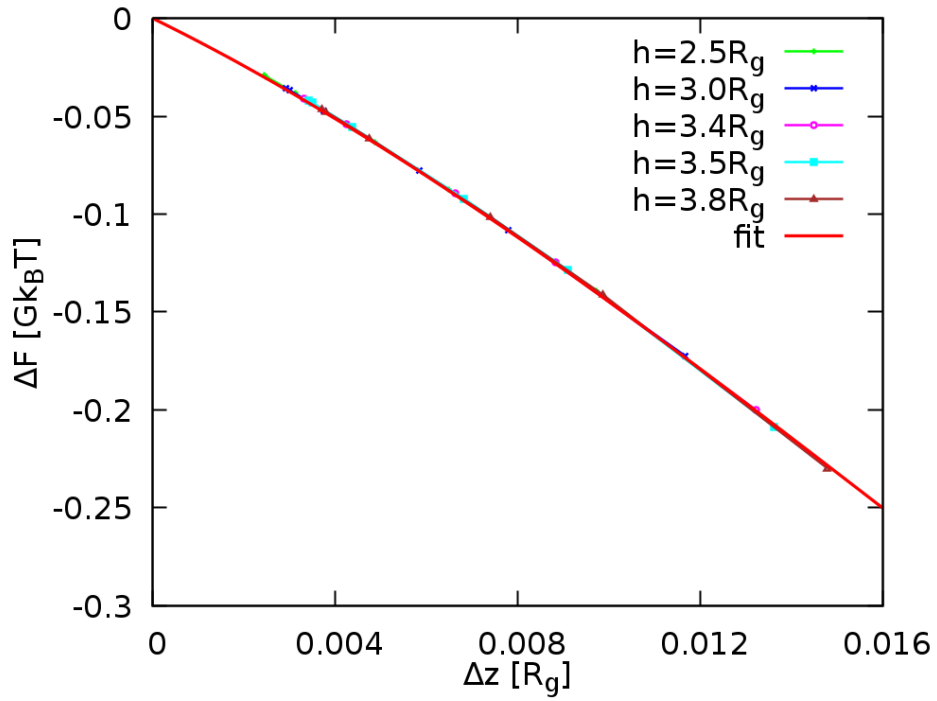

Figure 5.4: Shifted energy ΔF as a function of discretization Δz for different film thicknesses h with surface interactions $\Lambda_A N = -120$, $\Lambda_B N = -115$ at one surface and $\Lambda_A N = -95$, $\Lambda_B N = -90$ at the other surface. The chemical potential $\mu = (2.5 + \ln G) k_B T$. The solid line corresponds to the fit function, $\Delta F(\Delta z) = -11.43\,\Delta z - 375\,\Delta z^2 + 7012\,\Delta z^3$.

5.2 RESULTS

5.2.1 *Symmetric surfaces*

First, we study the AB diblock copolymer thin films confined between two symmetric surfaces with the interaction strength $\Lambda_A N = -120$, and $\Lambda_B N = -115$ at either surfaces. We investigate the orientational phase transition from a monolayer of cylinders, which are aligned parallel to the substrates ($C_{||}$), to a configuration of cylinders, which are oriented perpendicular to the substrate ($C_{\perp}$) due to the confinement effect. We apply self-consistent field theory (SCFT) [22, 52] to determine the Gibbs free energy per area landscape of the parallel and perpendicular cylinder phases as a function of the film thickness. At a given thickness, we always minimize the free energy with respect to the lateral distance in $x - y$ plane. As we mentioned before, in order to have an accurate free energy profile, the discretization effect could not be neglected. We have to be very careful when identifying the equilibrium morphologies. The free energies obtained from SCF calculations are then applied the corresponding shifted free energy $\Delta F = -12.27\,\Delta z - 341\,\Delta z^2 + 1447\,\Delta z^3$ due to the discretization error, as well as the van der Waals energy contribution.

Figure 5.5 presents the Gibbs free energy landscape as a function of the film thickness. We find that the local film thickness has a strong role in the phase

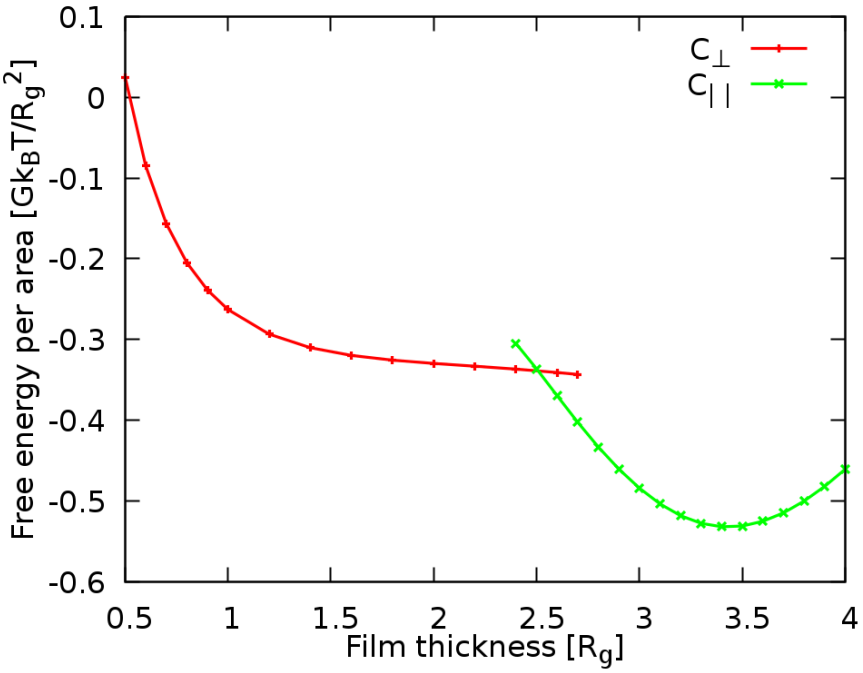

Figure 5.5: Gibbs free energy per area as a function of the film thickness of diblock copolymers confined between two symmetric surfaces at the chemical potential $\mu = (2.5 + \ln G)k_B T$. The strength of the interactions between block copolymers and the two identical walls are $\Lambda_A N = -120$, $\Lambda_B N = -115$.

diagram of diblock copolymers. As we discussed in the last chapter, there exists a minimum in the free energy landscape of a single layer of cylinders corresponding to the optimum thickness $h_{1L} = 3.5\, R_g$. When the film thickness is reduced below the optimum thickness of the monolayer, we observe a commensurability effect. To be more specific, at the thicknesses $h \leqslant 2.5 R_g$, this condition is energetically unfavourable for the monolayer of parallel cylinders, and the films start to orient themselves perpendicular to the plane of the films. As a result, there is a phase transition from the parallel to perpendicular orientation. The results are in a good agreement with other studies [32, 33, 91], where they studied both, static and dynamic properties of the phase behaviour of block copolymer thin films in experiments and computer simulations. They also observed the phase transition $C_{||} \rightarrow C_{\perp}$ as the film thickness mismatches with the favorite thickness of the monolayer and the surface fields are not strong. However, the cylinder aligned parallel to the surfaces ($C_{||}$) is more stable because its free energy minimum has lower value in the energy landscape (figure 5.5). On the contrary, the perpendicular cylinder configuration ($C_{\perp}$) does not have a real free energy minimum.

If one decreases the chemical potential, the free energy minimum corresponding to the $C_{||}$ configuration moves up relative to the free energy of $C_{\perp}$. This is clearly seen from figure 5.6. In the figure, we present free energy profile of the system when the chemical potential is decreased to $\mu = (2.372 + \ln G)k_B T$. The figure exhibits two free energy minima corresponding to the

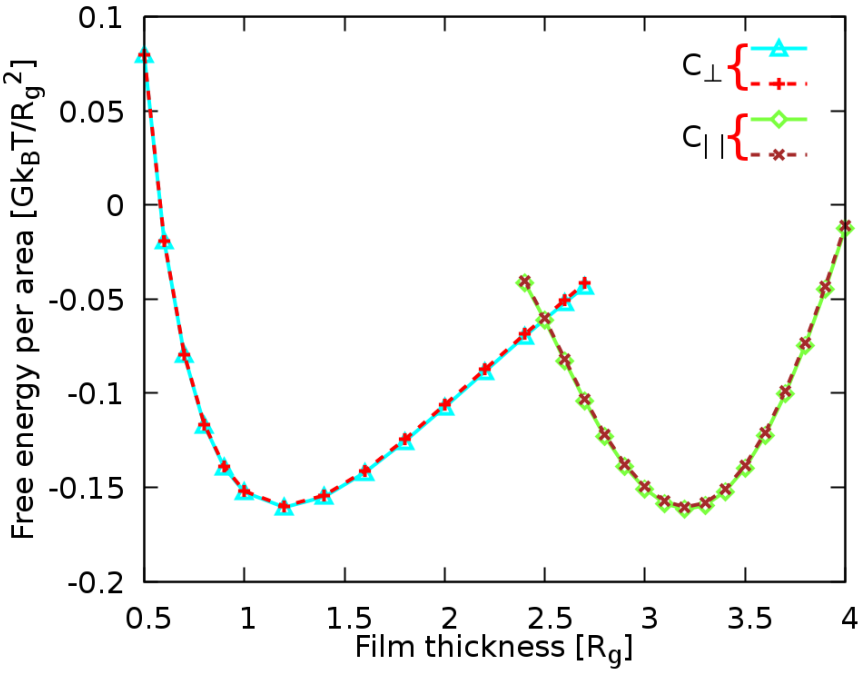

Figure 5.6: Gibbs free energy per area as a function of the film thickness of diblock copolymers confined between two symmetric surfaces at $C_{||}/C_{\perp}$ coexistence, $\mu = (2.372 + \ln G)k_BT$. The strength of the interactions between block copolymers and the two identical walls are $\Lambda_A N = -120$, $\Lambda_B N = -115$. The dashed lines are estimation from figure 5.5 via "μ- extrapolation method".

$C_{\perp}$ and $C_{||}$ orientations. It is noted that these two free energy minima have the same value. This result indicates that the $C_{\perp}$ configuration coexists with the $C_{||}$ one. Additionally, figure 5.6 also presents the free energy profile of the thin films at the chemical potential $\mu = (2.373 + \ln G)k_BT$ (two dashed lines), which is extracted from the data at the chemical potential $\mu = (2.5 + \ln G)k_BT$ via the following formula:

$$F_2 = F_1 - (\mu_1 - \mu_2)\, h\, \bar{\rho} = F_1 - \Delta\mu\, h\, \bar{\rho} \tag{5.11}$$

where $\Delta\mu$ is the difference of the chemical potential, h is the film thickness, and $\bar{\rho}$ is the average density. The extracted data are in very good agreement with those obtained from the SCFT calculations. It is noted that the "μ- extrapolation method" is a faster way to estimate the coexistence. However, the data obtained from such a method is not exactly the same as the one obtained from the SCFT. This is because $\bar{\rho}$ depends on the chemical potential μ. As a result, the configuration changes slightly with μ even at fixed thickness.

If we further decrease the chemical potential, the free energy minimum of the $C_{||}$ continues moving up relative to the $C_{\perp}$ minimum. Figure 5.7 shows the plot similar to those presented in figure 5.5 and 5.6 at the chemical potential $\mu = (2.35 + \ln G)k_BT$. There is still the phase transition $C_{||} \rightarrow C_{\perp}$ when the thickness is below the optimum thickness of the parallel monolayer. The $C_{\perp}$ perpendicular configuration becomes more stable than the $C_{||}$ parallel monolayer configuration since the free energy minimum of $C_{\perp}$ is lower than that of

the $C_{||}$. As before, the estimation from the "μ- extrapolation method" is quite good (two dashed lines).

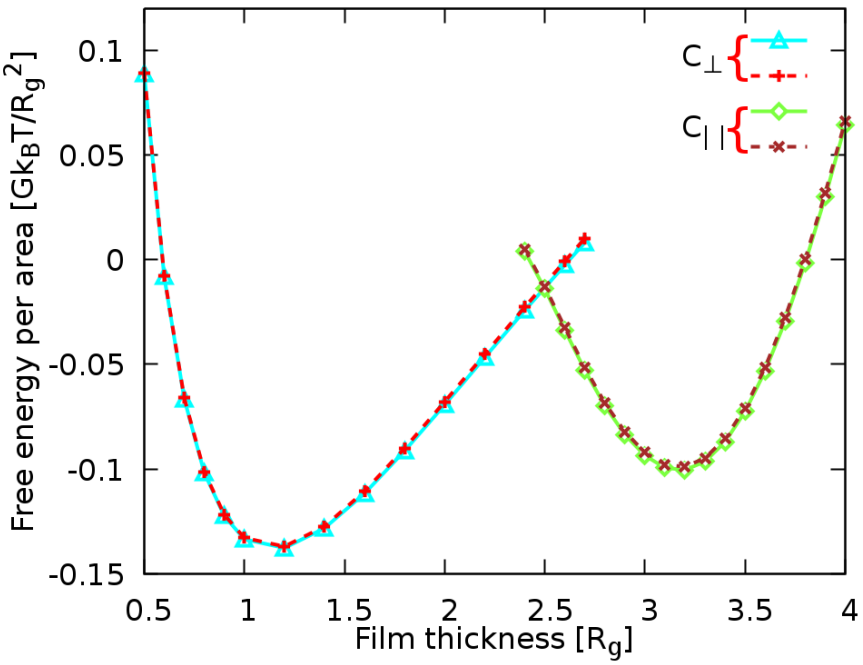

Figure 5.7: Gibbs free energy per area as a function of the film thickness of diblock copolymers confined between two symmetric surfaces at the chemical potential $\mu = (2.35 + \ln G)k_B T$. The strength of the interactions between block copolymers and the two identical walls are $\Lambda_A N = -120$, $\Lambda_B N = -115$. The dashed lines are estimation from figure 5.5 via "μ- extrapolation method".

Note that the free energy per area of the perpendicular configuration ($C_\perp$) increases as the film thickness decreases at different values of chemical potential discussed above. The results indicate that the perpendicular configuration $C_\perp$ is unstable and the thin films dewet from the substrate when the thickness is very small.

Our results are qualitatively consistent with recent experimental results of Professor Vega's group, where they studied the polystyrene-polybutadiene-polystyrene (SBS) triblock copolymer thin films. They employed supercritical carbon dioxide ($Sc - CO_2$) to anneal the thin films. Figure 5.8 shows the AFM image for the structures of copolymer films after 2h of annealing at different thicknesses. They found that the optimum thickness of monolayer is 39 nm. The copolymer films favor the $C_\perp$ perpendicular configuration at the thickness smaller than the optimum condition of the monolayer (panel b) and the films dewet and develop islands when the thickess is as well below the optimum thickness for the formation of the monolayer (panel a). However, the SCFT results are not quantitatively consistent with the experimental observation. Figure 5.9 shows the free energy as the function of the ratio h/λ_{bulk}, where $\lambda_{bulk} = 3.7\, R_g$ [80]. Our SCFT calculations suggest that the optimum thickness of the monolayer of parallel cylinders is $h/\lambda_{bulk} = 0.87$, while the experimental result for the same is $h/\lambda_{bulk} = 0.95$. Moreover, the SCFT

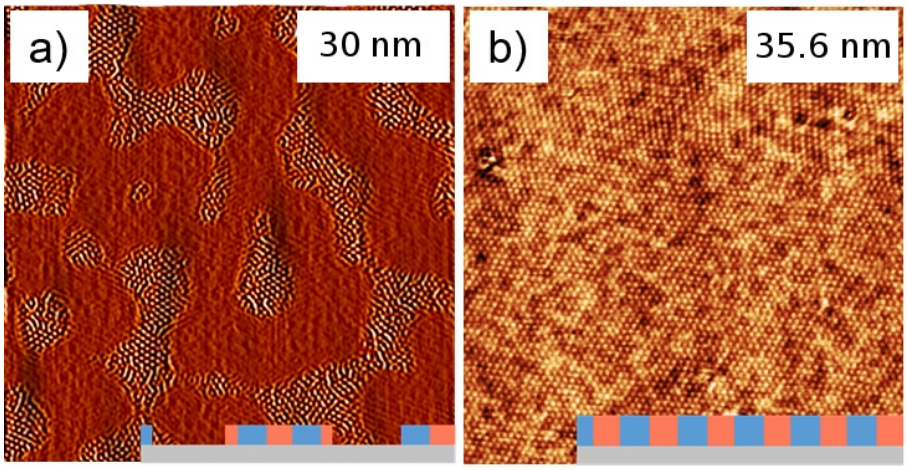

Figure 5.8: Atomic force microscopy (AFM) phase image for copolymer film configurations after 2 h of annealing in supercritical CO_2 at different film thicknesses [78].

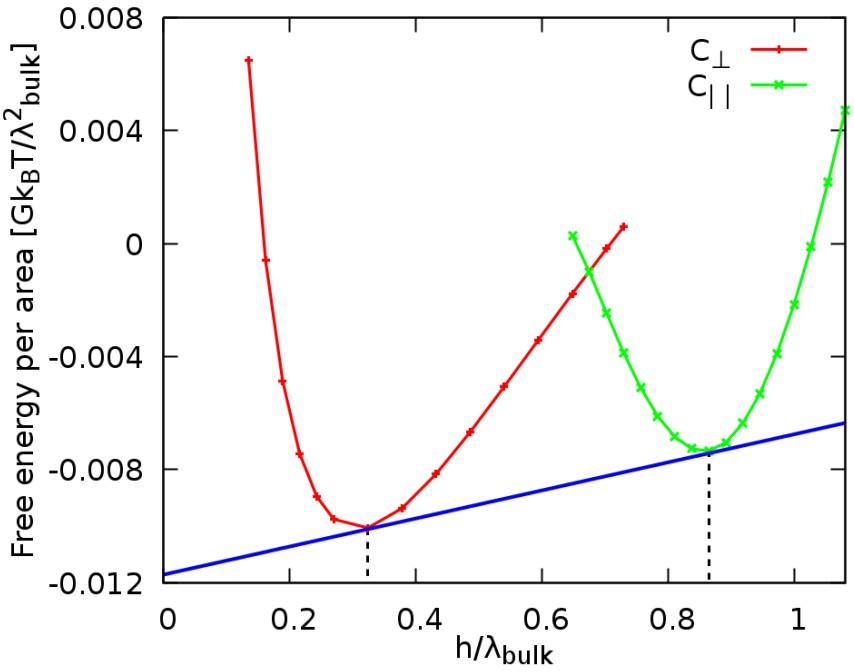

Figure 5.9: Gibbs free energy per area as a function of the ratio h/λ_{bulk} of diblock copolymers confined between two symmetric surfaces at the chemical potential $\mu = (2.35 + \ln G)k_BT$. The strength of the interactions between block copolymers and the two identical walls are $\Lambda_A N = -120$, $\Lambda_B N = -115$. The blue line is the constructed common tangent line.

results indicate that there is a coexistence of $C_\perp$ and $C_{||}$ at the thickness $0.3 < h/\lambda_{bulk} < 0.87$ and the films dewet at $h/\lambda_{bulk} < 0.3$. However, the experiments observed the $C_\perp$ at the thickness $h/\lambda_{bulk} = 0.87$, and the films dewet when the thickness is $h/\lambda_{bulk} \leqslant 0.7$.

5.2.2 *Asymmetric surfaces*

Although the assumption that the film surface is symmetric simplifies some analyses, many film systems have asymmetric surfaces, i.e., where the blocks/surface interactions have different strength at the two surfaces. This is the case for supported thin films. In order to explore the role of the strength of the surface fields in the morphologies of thin films, we consider a thin film with non-homogeneous surface conditions as well. The calculations for symmetric surfaces are carried out for asymmetric surfaces as well. In order to understand how the preference for the major A-block affects the morphologies of block copolymers, we study different degrees of asymmetric boundary conditions. We first study the thin film where the difference of interaction strength between copolymers and the two surfaces is small. The interaction parameters are chosen as $\Lambda_A N = -125$, $\Lambda_B N = -120$ at one wall and $\Lambda_A N = -115$, $\Lambda_B N = -110$ at the other one. Thus the difference of interactions between the two surfaces and the A-block is $\Delta^A_\Lambda = 10$ for such asymmetric interactions. The chemical potential is still fixed at $\mu = (2.5 + \ln G)k_B T$ as before. We find the equilibrium configuration and the corresponding free energy of the thin films at a given thickness. The SCF free energies are then applied the corresponding shifted energy ΔF due to the discretization error $\Delta F = -12.68\,\Delta z - 269\,\Delta z^2 - 2788\,\Delta z^3$ and the van der Waals interaction.

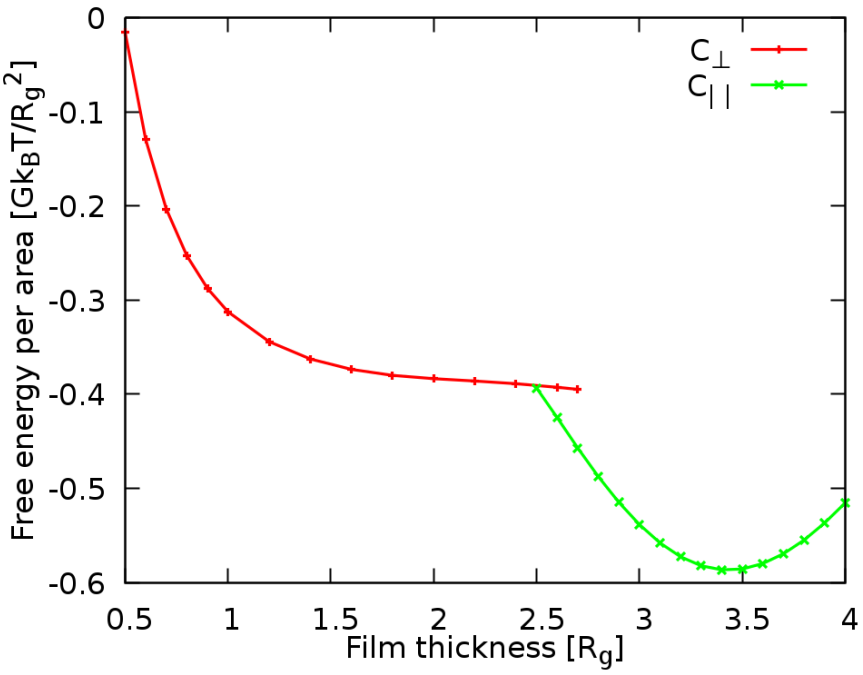

Figure 5.10: Gibbs free energy per area as a function of the film thickness of diblock copolymers confined between two asymmetric surfaces at the chemical potential $\mu = (2.5 + \ln G)k_B T$. The strength of surface interactions are chosen as: $\Lambda_A N = -125, \Lambda_B N = -120$ at one surface and $\Lambda_A N = -115, \Lambda_B N = -110$ at the other one.

The Gibbs free energy landscape as a function of the film thickness is presented in figure 5.10. Note that the results are similar to that of symmetric interaction at the surfaces. There is a phase transition from the single layer of parallel configuration to the perpendicular one as the film thickness is reduced below the natural size of the monolayer of cylinders. The boundary of the phase transition between parallel and perpendicular cylinders is around $h \leqslant 2.5R_g$ as for symmetric surface interactions. On the other hand, the single layer of parallel cylinders remains more stable since its minimum energy has the lower value. The results are consistent with the ones showed in Knoll's work [33, 91] as we discussed in the symmetric surface fields. Moreover, Knoll and his colleagues also found the perforated lamellae (PL) phase. We do not observe it in our system with the given surface field parameters. The reason might be that asymmetric surface interactions we used do not belong to the region of PL phase.

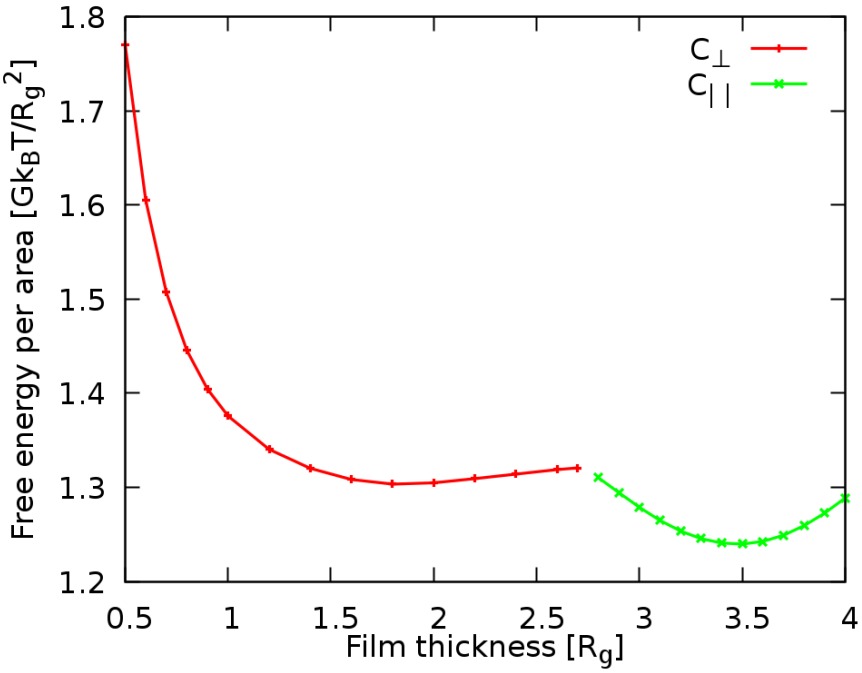

Figure 5.11: Gibbs free energy per area as a function of the film thickness of diblock copolymer confined between two asymmetric surfaces at the chemical potential $\mu = (2.5 + \ln G)k_BT$. The strength of the surface interactions are: $\Lambda_A N = -120, \Lambda_B N = -115$ at one surface and $\Lambda_A N = -100, \Lambda_B N = -95$ at the other one.

Afterwards, we slightly increase the asymmetry between the two surfaces by further reducing the interaction strengths at one surface. In particular, the interaction parameters are kept the same as before at one surface $\Lambda_A N = -120$, $\Lambda_B N = -115$, and at the other one are changed to $\Lambda_A = -100$, $\Lambda_B N = -95$. Thus the difference of the interaction strength between the A-block and the two surfaces is $\Delta_\Lambda^A = 20$ for such interaction parameters. We also consider another set of surface interactions with $\Delta_\Lambda^A = 25$, where $\Lambda_A N = -120$, $\Lambda_B N = -115$ at one wall and $\Lambda_A = -95$, $\Lambda_B N = -90$ at the other wall. We then seek

the concentration profiles corresponding to the minimum free energy of the systems at a certain film thickness. Thereafter, the free energies obtained from the SCFT calculations were corrected for the discretization errors. Then the energetic contributions due to the van der Waals interaction were added to the free energy above.

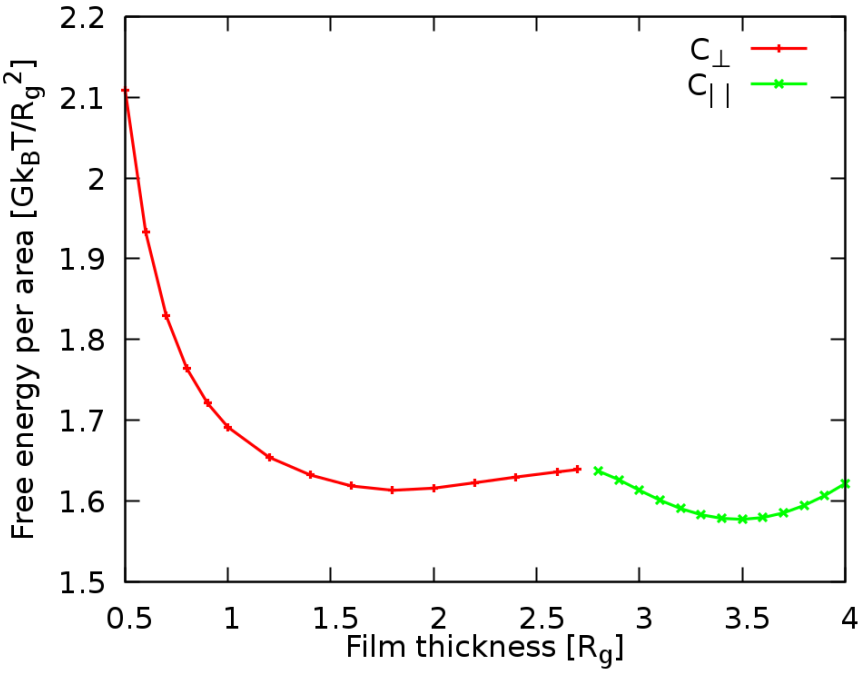

Figure 5.12: Gibbs free energy per area as a function of the film thickness of diblock copolymers confined between two asymmetric surfaces at the chemical potential $\mu = (2.5 + \ln G)k_BT$. The strength of surface interactions are: $\Lambda_A N = -120, \Lambda_B N = -115$ at one surface and $\Lambda_A N = -95, \Lambda_B N = -90$ at the other one.

Figures 5.11 and 5.12 show the same content as figures 5.5 and 5.10, the Gibbs free energy landscape of the films as a function of the film thickness. We still observed a phase transition from $C_{||} \rightarrow C_\perp$ as the film thickness is decreased below the natural size of the monolayer of cylinders. The $C_{||}/C_\perp$ border is changed to a slightly thicker thickness $h \leqslant 2.7\, R_g$. It means that the thin films start to rearrange the orientation to the plane of the film at thicker regions compared to the previous parameter set. Note that the free energy difference of $C_{||}$ and $C_\perp$ decreases as the degree of asymmetry between the two surfaces increases. Furthermore, the free energy profile of the perpendicular configuration starts to have a minimum. In other words, the $C_\perp$ phase has a favored film thickness, which is about half the optimal thickness of the monolayer of parallel cylinders. However, the free energy minimum of the parallel configuration has a lower value. Therefore, the $C_{||}$ phase is still more stable than the $C_\perp$ one.

As discussed in the symmetric surface interaction case, if one decreases the chemical potential the free energy minimum of monolayer of parallel cylinders moves up relative to the perpendicular minimum. For instance, we slightly

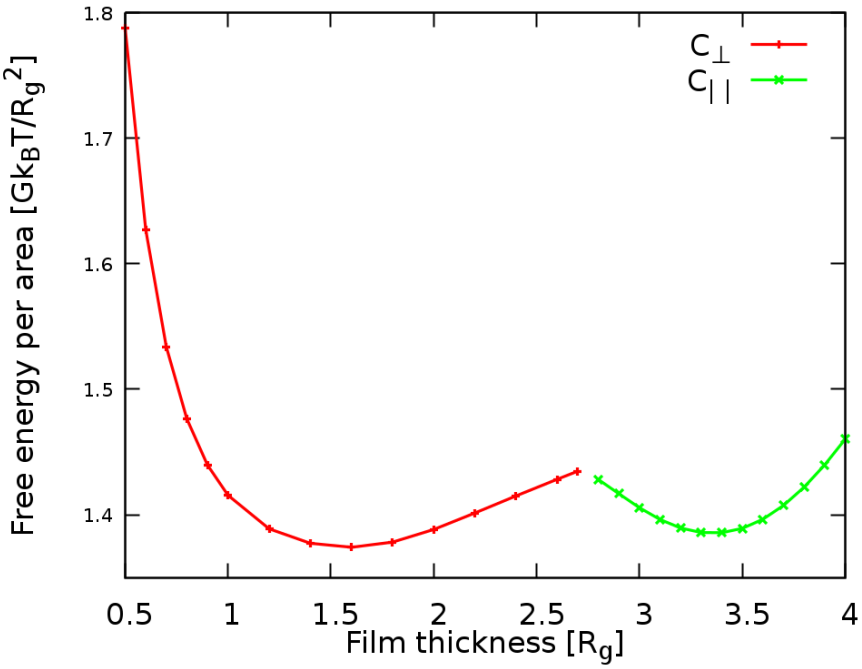

Figure 5.13: Gibbs free energy per area as a function of the film thickness of diblock copolymers confined between two asymmetric surfaces at the chemical potential $\mu = (2.45 + \ln G)k_BT$. The strength of surface interactions are: $\Lambda_A N = -120, \Lambda_B N = -115$ at one surface and $\Lambda_A N = -100, \Lambda_B N = -95$ at the other one.

decrease the chemical potential from $\mu = (2.5 + \ln G)k_BT$ down to $\mu = (2.45 + \ln G)k_BT$, then calculate the Gibbs free energy landscape of the films. Figure 5.13 presents the free energy per area as a function of the thickness. The $C_{||}/C_\perp$ is still around $h \approx 2.7\, R_g$. It is noted that the $C_\perp$ now has lower free energy minimum than the $C_{||}$. This indicates that the perpendicular configuration is more stable than the parallel configuration.

A further increase of the asymmetry of the affinity of A block between the two surfaces causes a significantly different structure evolution of the thin films. It results in the appearance of new morphologies, such as perforated lamellae (PL) and lamellae (L). In particular, we reduce the interaction strength between one surface and the blocks to enhance the affinity difference between the two surfaces. For example, we increase the difference of the selectivity of the A-block between the two surfaces up to $\Delta^A_\Lambda = 30$ with the surface interactions $\Lambda_A N = -120, \Lambda_B N = -115$ at one surface and $\Lambda_A N = -90, \Lambda_B N = -85$ at the other one. Then we find the equilibrium configuration and the minimum free energy as before. We see a transformation from $C_\perp$ into a perforated lamella PL structure at the film thickness corresponding to half of the optimum one of a single monolayer, $h = 1.8R_g$. The PL is found at a very specific film thickness, in agreement with Heckmann's work [92], where they found that perforated lamellae appeared only in a very small region of their phase diagram. We emphasize that our simulations are not biased to any particular microdomain structures. For instance, we use the $C_\perp$ phase as an initial

configuration to obtain the PL phase. It took quite a long computation time to reach the convergence conditions to equilibrate the PL phase compared to the $C_{||}$ or the $C_{\perp}$ phases in our SCFT calculations. Figure 5.14 shows the density profile of the PL configuration of the thin films. Instead of the B-minority block cylinders oriented parallel $C_{||}$ or perpendicular $C_{\perp}$ to the surfaces, there are hexagonally ordered microdomains of the A-majority block in a continuous B-block layer.

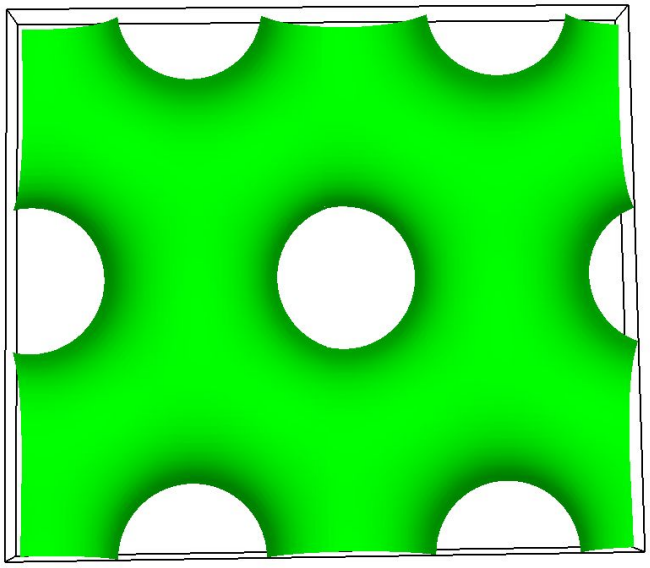

Figure 5.14: Perforated lamellae (PL) structure of the AB diblock copolymer thin films. Here, hexagonally ordered microdomains of the A-majority block in a continuous layer of the B-minority block, i.e., a perforated B block lamella are shown.

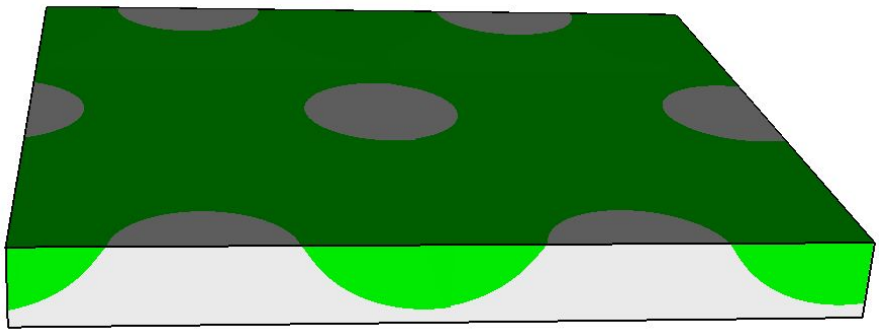

Figure 5.15: Perforated lamellae (PL) structure of the AB diblock copolymer thin films. It is similar to the figure 5.14 but from the side view.

We also investigate the free energy landscape in order to analyze the stability of the different morphologies of the diblock copolymer thin films. Figure 5.16 displays the free energy per area as a function of the film thickness. The existence of sharp borders between the $C_{\perp}$ and the PL perforated lamella phase in the energy landscape indicates that the $C_{\perp} \rightarrow$ PL transition as a function of film thickness is a first order phase transition. Interestingly, the free energy

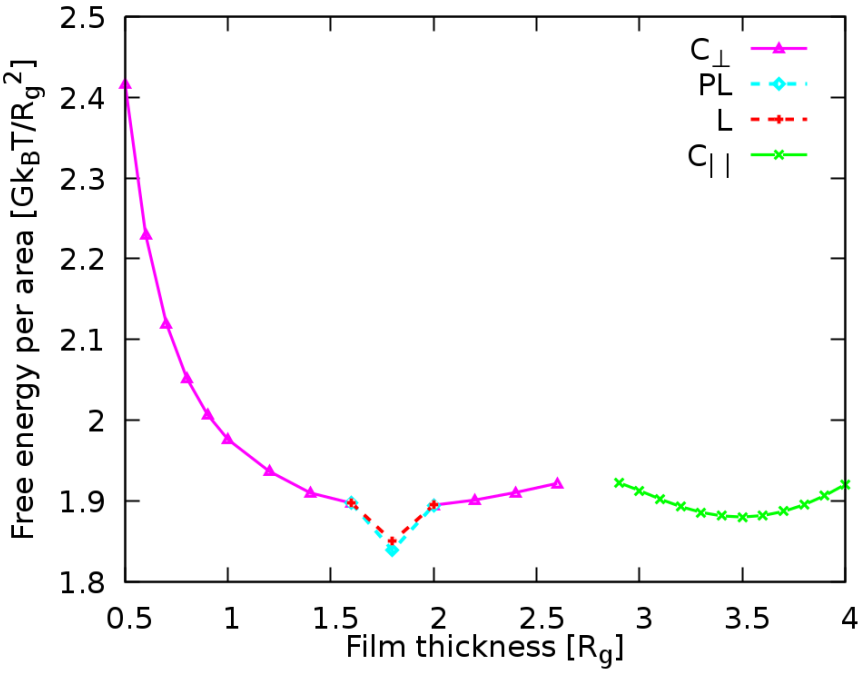

Figure 5.16: Gibbs free energy per area as a function of the film thickness of diblock copolymers confined between two asymmetric surfaces at the chemical potential $\mu = (2.5 + \ln G)k_BT$. The strength of surface interactions are: $\Lambda_A N = -120, \Lambda_B N = -115$ at one surface and $\Lambda_A N = -90, \Lambda_B N = -85$ at the other one.

of the $C_{||}$ does not correspond to the lowest free energy minimum any more. Instead, the free energy of PL phase is lower. In addition, we also calculate the free energy of lamellar phase (L) of the film (figure 5.17) in the region of the thickness where PL phase is found. Then we compare the free energy between the perforated lamellar and lamellar phases. It is obtained that the free energy of PL phase has the lowest value. It is an intriguing result since it is still an open question whether the perforated lamellae are stable phase or not. There are different studies of PL phase of copolymers in the bulk or in thin films with different conclusions. Hajduk et al. [95] studied different block copolymer systems and showed that the perforated lamella phase is a nonequilibrium structure, which might result from instabilities of the lamellae phase and is transformed into the gyroid phase after sufficienly long isothermal annealing. A theoretical study of Qi and Wang [96] suggested that the PL is a metastable phase, which is caused by unstable fluctuation of lamellae phase. Using real-space SCFT, Yang et al. [86] claimed that the PL phase is stable under thin film conditions, i.e., the confinement and the affinity of the substrates to the blocks. The thin films also dewet at very thin thickness.

These results again indicate that the surface fields play an essential role in determining the stable structure of the thin films as well as the film thickness [32, 33, 91]. It is also interesting to investigate the phase diagram of thin films when the asymmetry of the two surfaces to A-block becomes even larger. Thus we further increase the affinity difference of the two walls for A-

block up to $\Delta_\Lambda^A = 40$, where the interaction strength of the surface fields are $\Lambda_A N = -120, \Lambda_B N = -115$ at one surface and $\Lambda_A N = -80, \Lambda_B N = -75$ at the other one. Then, we carefully determine the equilibrium configurations of the films. Such a study results in an interesting phase behaviour. Besides the $C_{||}$ and $C_\perp$ structures, we obtain the lamella phase parallel to the substrates within a certain regime of the film thickness, which is around half of the optimal thickness of a single layer. The reason is that since the affinity of one wall for A-block is much stronger compared to the other wall, the concentration of the A-block increases near the former surface. Therefore, the films undergo another phase transition $C_\perp \to L$ in addition to the $C_{||} \to C_\perp$ transition. Figure 5.17 shows the parallel lamellar phase of the diblock copolymer films. Note that the PL phase is not found here. This confirms one more time the role of the surface fields in morphologies of thin films.

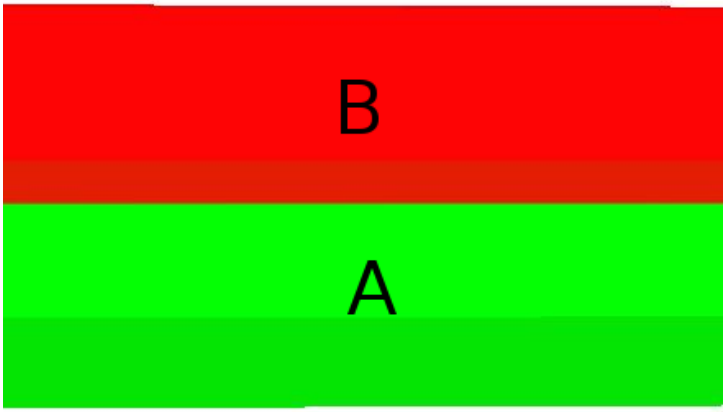

Figure 5.17: Lamellae (L) structure of the AB diblock copolymer thin films.

We present the Gibbs free energy per area of diblock thin films as a function of the thickness in figure 5.18 as we did for the surface fields in the cases above. From that we can examine the stability of the thin films. More interestingly, the single layer of parallel cylinders is not globally stable any more. The lamella phase becomes the globally stable one since its free energy is a global minimum. The optimum thickness, which corresponds to the energy minimum of the L phase is $h \approx 1.8\, R_g$. It is approximately half the optimum thickness of the monolayer of parallel cylinders. The difference of free energy between the minimum energies of the L and $C_{||}$ phases increases as the asymmetry between the air/film and film/substrate interfaces increases. This is shown in figure 5.19 where the surface selectivity difference Δ_Λ^A is extremely large. For such asymmetric interaction, the strength of the polymer/surface interactions are chosen as $\Lambda_A N = 5, \Lambda_B N = 30$ at one surface and $\Lambda_A N = -151, \Lambda_B N = -150$ at the other one. The free energy minimum corresponding to the L phase profoundly moves down relative to the monolayer minimum. It is reasonable since the preference of one surface to the A-block is much stronger than that of the other surface; therefore, the A-block has a significantly increased concentration near

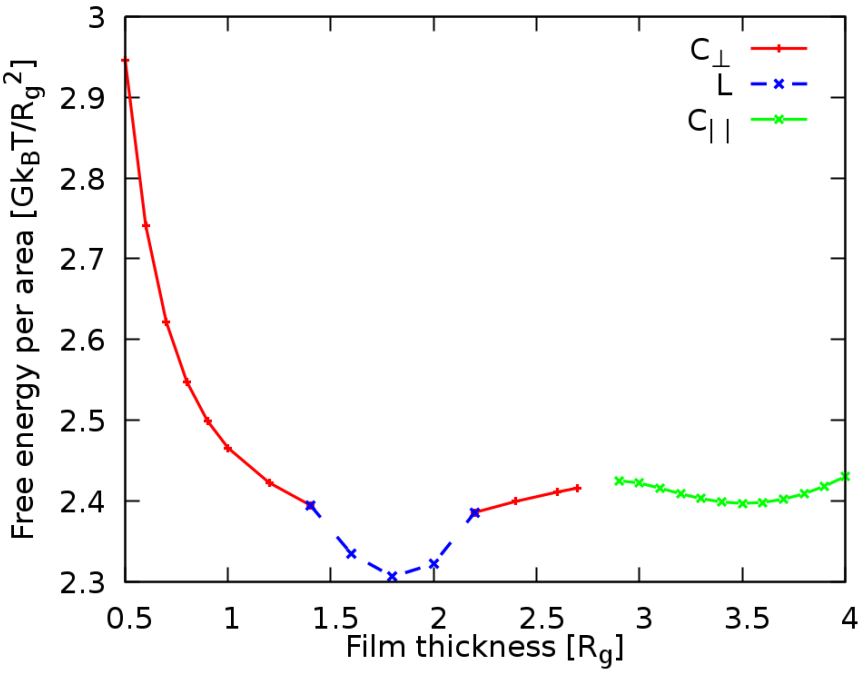

Figure 5.18: Gibbs free energy per area as a function of the film thickness of diblock copolymer confined between two asymmetric surface at the chemical potential $\mu = (2.5 + \ln G)k_BT$. The strength of surface interactions are: $\Lambda_A N = -120, \Lambda_B N = -115$ at one surface and $\Lambda_A N = -80, \Lambda_B N = -75$ at the other one.

the former surface. It results in the reduction of the free energy of the L lamella phase.

5.3 CONCLUSION

In conclusion, we have studied the morphologies of asymmetric diblock copolymers confined between two hard walls using the SCFT. We chose the volume fraction of the A-block to be $f = 0.7$, and an intermediate segregation parameter of $\chi N = 20$. The two surfaces preferentially attract the major block. We have identified the phase behaviour of copolymer thin films under the effect of both, surface fields and film thickness, where equilibrium structures for two- or three-dimenional systems were analyzed. We considered the case of two identical sufaces as well as the case of asymmetric surfaces. Together with other studies, either simulations or experiments [32, 78, 86, 91], our results give evidence that the equilibrium phase behaviour of diblock copolymer thin films is controlled by the interplay between the strength of the surface interaction fields and the mismatch of the film thickness and the optimal size of the monolayer of parallel cylinders. This causes either a rearrangement of orientation of cylinders to the plane of the films, a phase transition from the parallel to perpendicular configurations ($C_{||} \rightarrow C_{\perp}$) or the formation of other structures with sufficient surface fields, such as perforated lamellae and lamellae

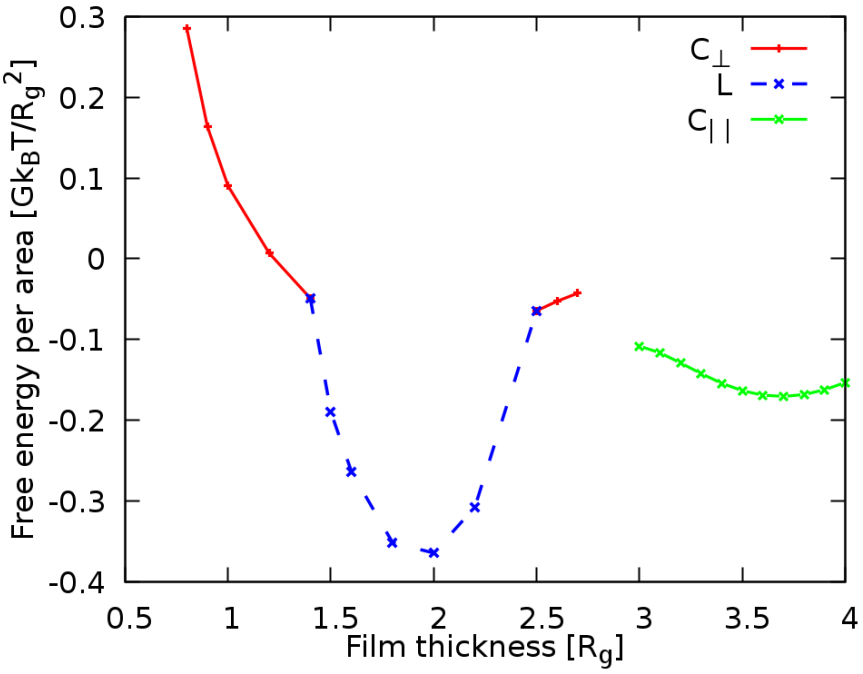

Figure 5.19: Gibbs free energy per area as a function of the film thickness of diblock copolymers confined between two asymmetric surfaces at the chemical potential $\mu = (2.5 + \ln G)k_BT$. The strength of surface interactions are: $\Lambda_A N = 5, \Lambda_B N = 30$ at one surface and $\Lambda_A N = -151, \Lambda_B N = -150$ at the other one.

phases. Therefore, other phase transitions, such as $C_\perp \to PL$ or $C_\perp \to L$ occur. The globally stable phase of the thin films depends on the surface fields. Specifically, the monolayer of $C_{||}$ parallel cylinders is stable as the surface fields are symmetric or slightly asymmetric, but the PL or L phases become more stable as the degree of asymmetry increases. Moreover, the thin films become unstable and dewet as the thickness is far below the natural size of a single layer of parallel cylinders.

6

CURVATURE AS A GUIDING FIELD FOR PATTERNS IN THIN BLOCK COPOLYMER FILMS

Previous chapters focused on block copolymer thin films confined between two planar substrates. In this chapter, we extend this framework to block copolymer thin films confined in a curved geometry (two coaxial cylindrical surfaces). We study the elastic properties of a monolayer of diblock copolymers forming cylindrical phase in free-standing membranes and curved supported thin films with self-consistent field theory (SCFT). The bending elasticity of anisotropic ordering on surfaces is common in biological membranes, where the competition with the membrane elasticity has a significant role in the morphology of these systems [97, 98]. We analyze how the curvature of the substrate affects the translational and orientational order that arises by minimizing the distortion energy of cylinder [35] in the free-standing membranes and the curved supported films. Moreover, the stability of the thin films against dewetting due to curvature is considered as well.

Part of the work presented in this chapter can be found in the preprint: "Curvature as a guiding field for patterns in thin block copolymer films", *Phys. Rev. Lett.*, **121**, 087801, 2018.

6.1 CURVATURE

The curvature is the deviation from flatness, for example, a surface deviates from being a flat plane or a curve from being a straight line. Therefore, it is a measure of the rate of change of the tangent vector along the normal, or, in other words, a measure of the rate of change the normal along the tangent vector. This can be described through the principal curvatures. For a two dimensional surface, there are two principal curvatures k_1 and k_2, which determine the local shape of a point on a surface. One shows the direction of maximum curvature, while the other shows the direction of minimum curvature. The local geometric properties of a surface can be described through k_1 and k_2 by the mean and Gaussian curvatures. The mean curvature H is equal to half the sum of the principal curvatures

$$H = \frac{1}{2}(k_1 + k_2) \tag{6.1}$$

and the Gaussian curvature K is equal to the product of the principal curvatures

$$K = k_1 k_2, \tag{6.2}$$

If at a point on a surface, k_1 and k_2 have the same sign then the Gaussian curvature is positive, for example in spheres or ellipsoids. In contrast to that, the Gaussian curvature is negative, if k_1 and k_2 have opposite signs at a point on the surface. This is the case of a saddle-like surfaces. The magnitudes of k_1

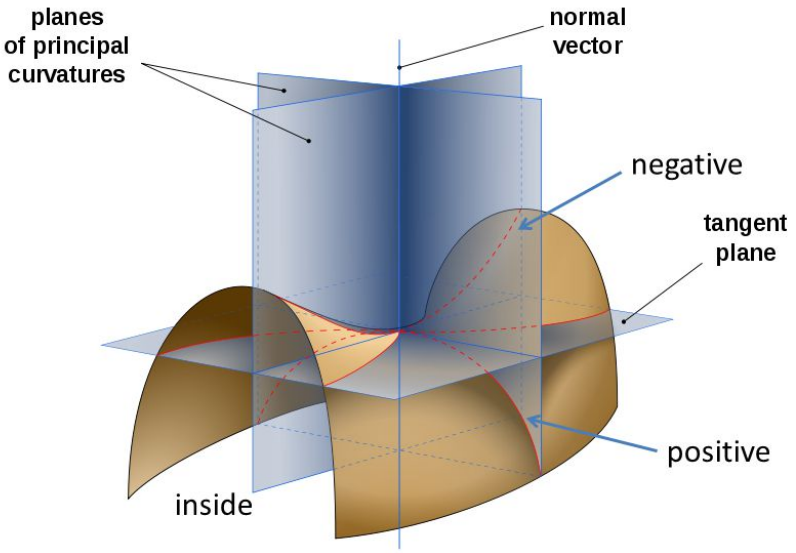

Figure 6.1: The saddle surface has negative curvature since k_1 and k_2 have different signs. The magnitudes of the two principal curvatures are given by the inverse radii of the tangent circles drawn as dashed red line [**wiki**].

and k_2 are equal to the inverse of the radius of tangent circles in the principal directions. An example is saddle surface, which is shown in figure 6.1. It has a negative Gaussian cuvature.

6.2 SYMMETRY CONSIDERATIONS

Here, we first establish a theoretical understanding of the phenomena observed in diblock copolymer membranes by using general symmetry considerations. The curvature free energy per area of *isotropic* fluid-like membranes can be written as the Helfrich formula [99, 100]:

$$F_{HC} = \frac{\kappa_b}{2}(2H - c_0)^2 + \kappa_g K \ , \tag{6.3}$$

where κ_b is the bending regidity, κ_g is the Gaussian curvature modulus, and c_0 is the spontaneous curvature. These parameters determine the properties of the thin films. The first term describes the change in energy since the average curvature of the film deviates from the spontaneous curvature. The last term is the part of the energy which depends on the Gaussian curvature K, and therefore on the topology of the film. One can consider this energy as an expansion in terms of the invariants of the shape operator **S** of the surface. This phenomenological approach was initiated by Helfrich and de Gennes, and further developed by a number of authors. It has become a successful method to study molecular membranes, vesicles, and microemulsion [101–103].

Now we discuss a general expression for the curvature free energy per area of a mathematically thin surface with the shape operator $\mathbf{S}$. In its own Eigensystem, the shape tensor $\mathbf{S}$ can be written as:

$$\mathbf{S} = k_1 \mathbf{u}_1 \otimes \mathbf{u}_1 + k_2 \mathbf{u}_2 \otimes \mathbf{u}_2 \tag{6.4}$$

Here, k_1, k_2 are the principal curvatures and $\mathbf{u}_1, \mathbf{u}_2$ denote the corresponding Eigenvectors. We can choose $|k_1| > |k_2|$ without loss of generality. If a membrane or thin film has in-plane order characterized by a director field $\mathbf{n}$, which is the orientation of the cylinders, then the curvature free energy per area no longer has to be rotationally symmetric. Thus, it may contain additional terms. These terms take the form $(\mathbf{n}\cdot\mathbf{S}\cdot\mathbf{n})$, $(\mathbf{n}\cdot\mathbf{S}\cdot\mathbf{n})^2$ [104, 105], and $(\mathbf{n}\cdot\mathbf{S})^2$ [106, 107]. Here, we consider up to second order in terms of $\mathbf{S}$. We write the contribution of these additional terms to the curvature free energy per area in the general form:

$$F_{\mathbf{n}} = A\,\mathbf{n}\cdot S\cdot\mathbf{n} - B(\mathbf{n}\cdot\mathbf{S}\cdot\mathbf{n})^2 - C(\mathbf{n}\cdot\mathbf{S})^2 \tag{6.5}$$

It is useful to represent $F_{\mathbf{n}}$ in terms of an angle of the director orientation with respect to the direction of the curvature $\{\mathbf{u}_1, \mathbf{u}_2\}$. The product $(\mathbf{n}\cdot\mathbf{u}_1)$ defines the angle θ between the director and the direction of the largest curvature *via*

$$(\mathbf{n}\cdot\mathbf{u}_1)^2 = \cos^2\theta \tag{6.6}$$

In addition, $\mathbf{n}, \mathbf{u}_1$ and $\mathbf{u}_2$ have the following properties

$$\mathbf{n} = (\mathbf{n}\cdot\mathbf{u}_1)\mathbf{u}_1 + (\mathbf{n}\cdot\mathbf{u}_2)\mathbf{u}_2 \tag{6.7}$$

$$(\mathbf{n}\cdot\mathbf{u}_2)^2 = 1 - (\mathbf{n}\cdot\mathbf{u}_1)^2 \tag{6.8}$$

Inserting these three equations into equation 6.5 of $F_{\mathbf{n}}$, we obtain:

$$\begin{aligned} F_{\mathbf{n}} = {} & A\,H - \left(\frac{3}{2}B + 2C\right)H^2 + \left(\frac{1}{2}B + C\right)K \\ & + \left(\frac{A}{2}(k_1 - k_2) - (B + C)(k_1 - k_2)H\right)\cos(2\theta) \\ & - \frac{B}{2}(H^2 - K)\cos(4\theta) \end{aligned} \tag{6.9}$$

In this equation, the first term can be absorbed in the spontaneous curvature c_0, and the next two terms in the bending and Gaussian modulus κ_b and κ_g, respectively. The last two terms give the expression for the anisotropic curvature free energy per area F_{ani}, which we obtained by substracting isotropic contributions F_{HC} from $F_{\mathbf{n}}$. By some simple calculations we get the following general expression for the anisotropic curvature free energy per area:

$$F_{ani} = -\frac{\kappa'}{2}(k_1 - k_2)(2H - c_0')\cos(2\theta) - \frac{\kappa''}{2}(H^2 - K)\cos(4\theta) \tag{6.10}$$

with

$$\begin{cases} \kappa' = B + C \\ \kappa'' = B \\ c_0' = A/(B + C) \end{cases}$$

Here $\theta \in [0 : \pi/2]$, κ', κ'', and c_0' are anisotropic elastic parameters. In the symmetric membranes, c_0' vanishes ($c_0' = 0$).

6.3 POLYMER SYSTEM

We study a melt of n asymmetric AB diblock copolymer molecules confined in a volume V between two coaxial cylindrical surfaces of radius R_1 and $R_2 = R_1 + h$, with h being the thickness of the confined film (see scheme of the systems below, figures 6.5 and 6.15). Hence, the Gaussian curvature of the thin film vanishes ($K = 0$) due to the property of the cylindrical surface. Each diblock copolymer molecule consists of N segments of which a fraction f represents the majority block A. We assume that A and B segments have equal statistical segment length b. These two surfaces preferentially attract the majority block A. The microscopic concentration operators of the A and B segments at a given point $\mathbf{r}(r, \varphi, z)$ are defined as

$$\hat{\phi}_A(\mathbf{r}) = \frac{N}{\rho_0} \sum_{j=1}^{n} \int_0^f ds\, \delta(\mathbf{r} - \mathbf{r}_j(s)) \tag{6.11}$$

$$\hat{\phi}_B(\mathbf{r}) = \frac{N}{\rho_0} \sum_{j=1}^{n} \int_f^1 ds\, \delta(\mathbf{r} - \mathbf{r}_j(s)) \tag{6.12}$$

respectively. These concentrations are made dimensionless by dividing by the average segment density ρ_0 ($\rho_0 = \frac{nN}{V}$).

The interaction potential of the melt is given in the form

$$\begin{aligned} \mathcal{H}_\mathcal{J} &= k_B T \rho_0 \chi \int d\mathbf{r} \hat{\phi}_A(\mathbf{r}) \hat{\phi}_B(\mathbf{r}) + k_B T \rho_0 \frac{\kappa}{2} \int d\mathbf{r} \left[\hat{\phi}_A(\mathbf{r}) + \hat{\phi}_B(\mathbf{r}) - 1\right]^2 \\ &\quad + k_B T \rho_0 \int d\mathbf{r}\, H(\mathbf{r}) \left[\Lambda_A^{s,a} \hat{\phi}_A(\mathbf{r}) + \Lambda_B^{s,a} \hat{\phi}_B(\mathbf{r})\right] \end{aligned} \tag{6.13}$$

where $H(\mathbf{r})$ are surface fields, and $\Lambda_{A,B}^{s,a}$ give the interaction strength between the A or B block, respectively, and the substrate (s) and air (a) interface. We choose a form of the surface interaction, which is similar to that in the planar thin films:

$$H(\mathbf{r}) = \begin{cases} (1 + \cos(\pi(r - R_1)/\epsilon)) & R_1 \leqslant r \leqslant R_1 + \epsilon \\ 0 & R_1 + \epsilon \leqslant r \leqslant R_2 - \epsilon \\ (1 + \cos(\pi(R_2 - r)/\epsilon)) & R_2 - \epsilon \leqslant r \leqslant R_2 \end{cases} \tag{6.14}$$

with the cutoff of the surface interactions $\epsilon = 0.2 R_g$. The "surface interaction energies per area" of the component A or B are defined as the integrated surface energy per area of a hypothetical film of A or B monomers with density $\hat{\phi}_{A,B} \equiv 1$, i.e.,

$$\gamma_{A,B}^{s,a} = \rho_c \int d\mathbf{r}\, H(\mathbf{r})\, \Lambda_{A,B}^{s,a} \tag{6.15}$$

Where $\rho_c = \rho_0/N$ is the density of the copolymer chains. The "surface interaction energies per area" will be given in units of $\hat{\gamma} = \rho_c R_g k_B T$ (which is a unit of energy per area).

Here we study two systems, one is free-standing membranes and the other is curved supported thin films. In the membranes study we assume that the two surfaces are symmetric for each block, $\Lambda_A^s N = \Lambda_A^a N = -120$ and $\Lambda_B^s N = \Lambda_B^a N = -115$ corresponding to $\gamma_A^{s,a} N = -24\hat{\gamma}$ and $\gamma_B^{s,a} N = -23\hat{\gamma}$. In the curved supported thin films, we choose symmetric surface interactions for the B-block $\Lambda_B^s N = \Lambda_B^a N = -30$ corresponding to $\gamma_B^{s,a} N = -6\hat{\gamma}$, and asymmetric conditions for the A-block. Specifically, we study two cases:

I. The substrate attracts the A-block stronger than the free (air) surface. The surface interaction parameters are: $\Lambda_A^s N = -120, \Lambda_A^a N = -50$ with corresponding surface energy per area $\gamma_A^s N = -24\hat{\gamma}$, $\gamma_A^a N = -10\hat{\gamma}$.

II. The free surface attracts the A-block stronger than the substrate. The surface interactions are chosen as $\Lambda_A^s N = -50, \Lambda_A^a N = -100$ with corresponding surface energy per area $\gamma_A^s N = -10\hat{\gamma}$ and $\gamma_A^a N = -20\hat{\gamma}$. In this case of asymmetric conditions, we also do simulations with two other sets of paramters. We keep the interaction between B-block and the surfaces but vary the interaction of the A-block and the surfaces as: ($\Lambda_A^s N = -70, \Lambda_A^a N = -100$ corresponding to $\gamma_A^s N = -14\hat{\gamma}, \gamma_A^a N = -20\hat{\gamma}$) and ($\Lambda_A^s N = -50, \Lambda_A^a N = -120$ corresponding to $\gamma_A^s N = -10\hat{\gamma}, \gamma_A^a N = -24\hat{\gamma}$).

As we discussed in chapter 2, the main task is solving modified diffusion equations. However, here the systems are given in cylindrical coordinates, so the Laplace operator takes the form:

$$\Delta = \frac{\partial^2}{\partial r^2} + \frac{1}{r}\frac{\partial}{\partial r} + \frac{1}{r^2}\frac{\partial^2}{\partial \varphi^2} + \frac{\partial^2}{\partial z^2} \tag{6.16}$$

Due to the anisotropy of the smectic pattern, the elastic energy of deformation depends on the local orientation of the pattern with regard to the directions on the main curvature. To determine the configurations with the lowest energy and to facilitate comparison with experiments, here we mainly consider the two limiting cases where the pattern is either parallel ($C_{||}$) or perpendicular ($C_\perp$) to the $\vec{e}_z$ direction (see scheme below). In each case, the radius of curvature R of the substrate is fixed while the thin film thickness and characteristic pattern wavelength are optimized to obtain the lowest energy state.

The parallel configuration does not depend on the z-direction, so we solve the diffusion equations in the two dimensional films to save simulation time using the following Laplace operator:

$$\Delta = \frac{\partial^2}{\partial r^2} + \frac{1}{r}\frac{\partial}{\partial r} + \frac{1}{r^2}\frac{\partial^2}{\partial \varphi^2} \tag{6.17}$$

The confined film of thickness in constrained in r-direction, and the periodic boundary conditions are imposed in the φ-direction.
Similarly, the perpendicular configuration does not depend on φ-direction. Thus, we solve the diffusion equations in the two dimensional systems using the following Laplace operator:

$$\Delta = \frac{\partial^2}{\partial r^2} + \frac{1}{r}\frac{\partial}{\partial r} + \frac{\partial^2}{\partial z^2} \tag{6.18}$$

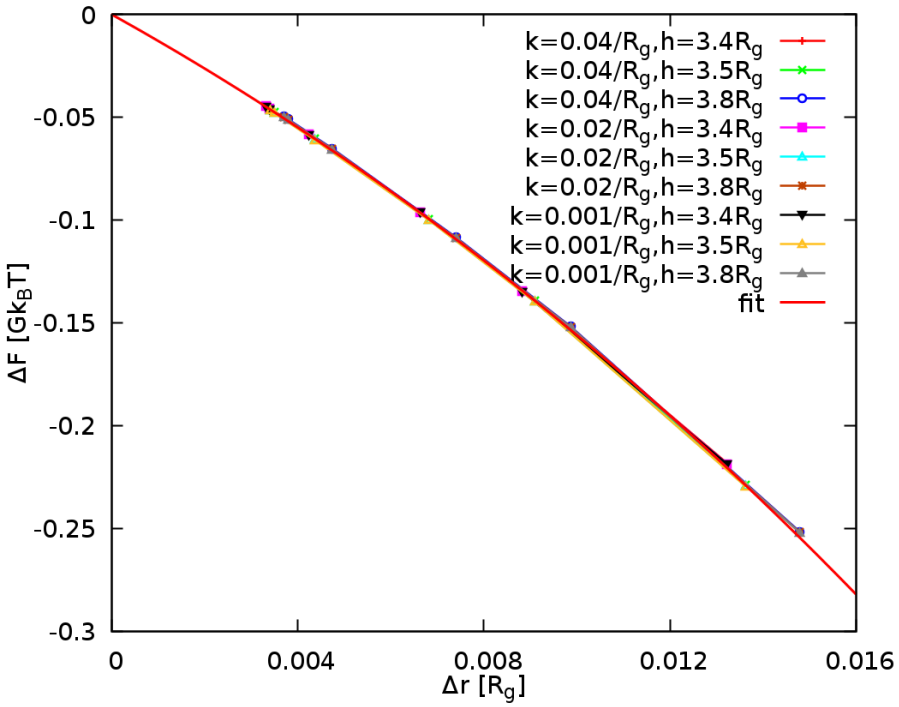

Figure 6.2: Shift of free energy ΔF as a function of discretization Δr for the symmetric films with the surface interactions $\Lambda_A^a N = -120$, $\Lambda_B^a N = -115$, for different curvatures and film thicknesses h as indicated. The solid line corresponds to the fit function $\Delta F(\Delta r) = -12.6\Delta r - 277\Delta r^2 - 2367\Delta r^3$.

Periodic boundary conditions are applied in the z-direction. All calculations are performed in the grand canonical ensemble. Of course, we need input for the chemical potential. It was used $\mu = (2.5 + \ln G)k_B T$ in chapter 4 and 5, but in this chapter we have to slightly increase it $\mu = (2.55 + \ln G)k_B T$, otherwise the films on curved substrates with positive curvature are not stable or metastable. However, the calculations are performed with both values of the chemical potential $\mu = (2.5 + \ln G)k_B T$ and $\mu = (2.55 + \ln G)k_B T$ for the free-standing membranes.

The discretization in space, the azimuthal and thin film directions is chosen as $\Delta z = 0.05 R_g$ and $\Delta r = 0.01 R_g$, respectively. The contour parameter s is discretized in steps of $\Delta s = 0.0001$. As in the previous chapters, we find that the discretization in the direction normal to the film plane (r-direction) has a significant influence on the accuracy of the free energies, and discretization errors could not be neglected. On the other hand, we also find that they lead to an energy shift ΔF which depends only on Δr and not on the film thickness, the curvature, or the orientation of the cylinders (parallel or perpendicular). Therefore, we study the dependence of ΔF on Δr systematically for different values of the film thickness and curvature. Then we fit the result to a third order polynomial, the fit functions are $\Delta F(\Delta r) = -11.75\Delta r - 270\Delta r^2 + 5035\Delta r^3$ ($\Delta F(\Delta r) = -11.95\Delta r - 167\Delta r^2 + 3737\Delta r^3$) and $\Delta F(\Delta r) = -12.6\Delta r - 277\Delta r^2 - 2367\Delta r^3$ with asymmetric and symmetric surface interactions, respectively. Figures 6.2, 6.3

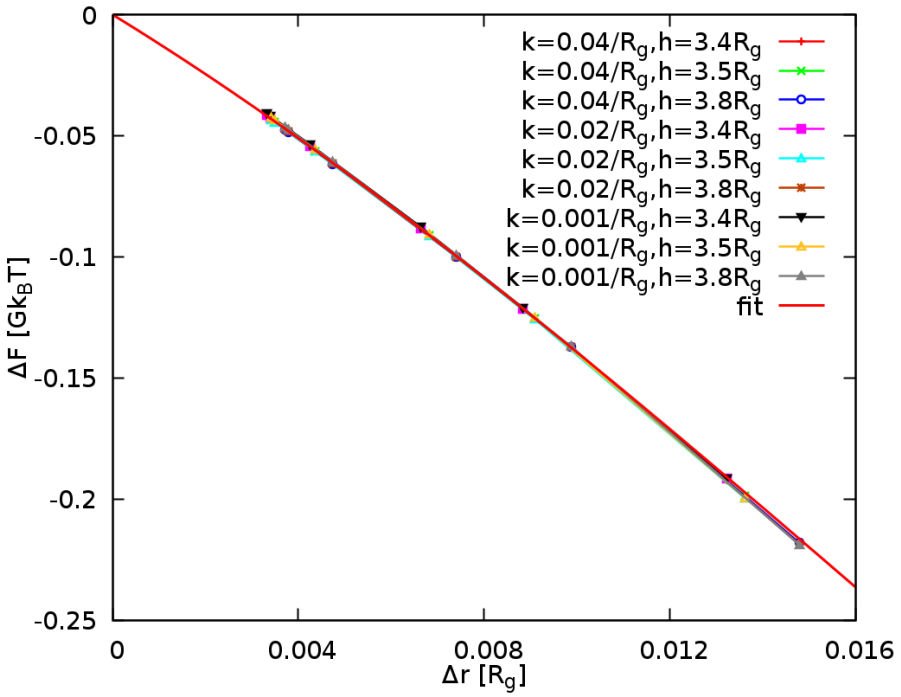

Figure 6.3: Shift of free energy ΔF as a function of discretization Δr for the films with asymmetric surface interaction $\Lambda_A^s N = -120, \Lambda_B^s N = -30$ at the fixed substrate and $\Lambda_A^a N = -50, \Lambda_B^a N = -30$ at the free surface for different curvatures and film thicknesses h as indicated. The solid line corresponds to the fit function $\Delta F(\Delta r) = -11.75\Delta r - 270\Delta r^2 + 5035\Delta r^3$.

and 6.4 present the fitting results. These corrections are then applied to the results of the SCFT calculations.

In addition, we also consider the contribution of the van der Waals interaction to the free energy of the diblock copolymer films as previous chapters. However, the estimate of the vdW interaction for the systems studied in this chapter is $\sim 0.004\, G k_B T$. Such a value is very small when compared to the SCFT free energies. Hence, it can be neglected as in chapter 4 without influencing the results regarding the most stable morphology.

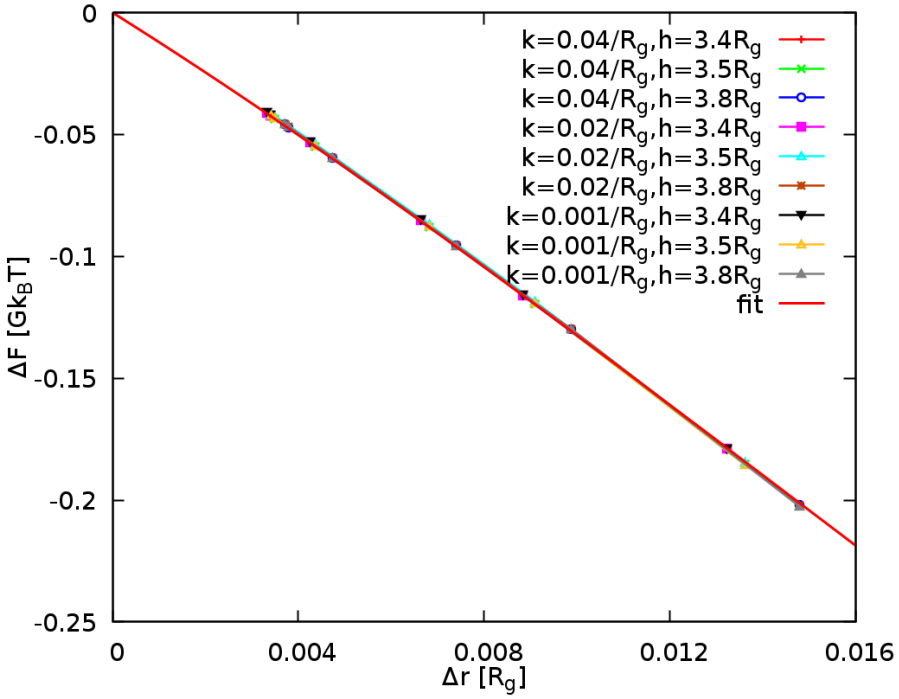

Figure 6.4: Shift of free energy ΔF as a function of discretization Δr for films with the asymmetric surface interactions $\Lambda_A^s N = -50, \Lambda_B^s N = -30$ at the fixed substrate and $\Lambda_A^a N = -100, \Lambda_B^a N = -30$ at the free surface for different curvatures and film thicknesses h as indicated. The solid line corresponds to the fit function $\Delta F(\Delta r) = -11.95\Delta r - 167\Delta r^2 + 3737\Delta r^3$.

6.4 BOUNDARY CONDITIONS

As discussed in the previous section, the SCFT calculations are done in cylindrical coordinates (r, φ, z), where r is the direction normal to the plane of the films or the membranes and z is the direction of the zero curvature. Configurations $C_{\parallel}$ and $C_{\perp}$ with cylinder orientations parallel or perpendicular to the direction of the curvature can be obtained with periodic boundary conditions in the (φ, z) directions. Furthermore, in the free-standing membranes, we also consider a configuration where the angle between the orientation of the cylinder and the direction of the largest curvature is an arbitrary angle θ. This configuration is called θ-configuration. In order to impose a given tilted orientation with tilt angle θ, we must apply tilted boundary conditions, either in the z or in the φ direction. We do this by using affine coordinates (r, u, v) with periodic boundary conditions in (u, v). To be more specific, we use two affine coordinate systems. The first one is:

$$\begin{cases} r &= r \\ u &= \varphi \\ v &= z - \varphi a \qquad \text{case (1)} \\ a &= R \tan\theta \end{cases}$$

and the second affine coordinate system is:

$$\begin{cases} r &= r \\ u &= \varphi - bz \\ v &= z \qquad\qquad \text{case (2)} \\ b &= 1/R/\tan\theta \end{cases}$$

where R is the radius of the curvature of the membranes. In case (1), $a = 0$ corresponds to the perpendicular configuration $C_\perp$ ($\theta = 0$), and in case (2) $b = 0$ corresponds to the parallel configuration $C_\parallel$ ($\theta = \pi/2$).

We solve the modified diffusion equations with periodic boundary conditions in effectively two dimensions: (r, v), independent of u in case (1), and (r, u), independent of v in case (2). This enforces tilted orientations of cylinders. In general, the Laplace-Beltrami operator has the following form

$$\Delta_{LB} = \frac{1}{\sqrt{|\det g|}} \sum_{ij} \frac{\partial}{\partial x_i} \left(g^{ij} \sqrt{|\det g|} \frac{\partial}{\partial x_j} \right) \tag{6.19}$$

where g_{ij} is the metric tensor and g^{ij} is its inverse. Applying this general expression of the Laplace-Beltrami operator for the cases (1) and (2), we obtain the Laplace-Beltrami operator in the two cases as below

$$\begin{aligned} \Delta_{LB}^{(1)} &= \frac{1}{r}\frac{\partial}{\partial r} + \frac{\partial^2}{\partial r^2} + \frac{1}{r^2}\frac{\partial^2}{\partial u^2} - \frac{2a}{r^2}\frac{\partial^2}{\partial u\,\partial v} \\ &\quad + \left(1 + \frac{a^2}{r^2}\right)\frac{\partial^2}{\partial v^2} \qquad \text{case (1)} \end{aligned} \tag{6.20}$$

$$\begin{aligned} \Delta_{LB}^{(2)} &= \frac{1}{r}\frac{\partial}{\partial r} + \frac{\partial^2}{\partial r^2} + \left(\frac{1}{r^2} + b^2\right)\frac{\partial^2}{\partial u^2} \\ &\quad -2b\frac{\partial^2}{\partial u\,\partial v} + \frac{\partial^2}{\partial v^2} \qquad \text{case (2).} \end{aligned} \tag{6.21}$$

We use the setup (1) for small angles θ where they are gradually increased from 0 to $\pi/4$. Similarly, we use the setup (2) for the angles θ close to $\pi/2$ where they are gradually reduced from $\pi/2$ to $\pi/4$. Afterwards, we combine the results from both setups in order to have the entire range of intermediate angles $\theta \in (0 : \pi/2)$.

6.5 RESULTS

6.5.1 *Free-Standing Membranes*

Since in the free-standing membrane systems there is an up-down symmetry, the middle surface of the thin film is considered as the surface of reference. The middle surface as demonstrated in figure 6.5 is charaterized by a radius of curvature R_m, and the curvature therefore is $k = 1/R_m$. This surface is kept fixed when minimizing the surface energy per area. The strength of interactions between the two surfaces (substrate and air) are symmetric to each block copolymer, with $\Lambda_A^s N = \Lambda_A^a N = -120$ and $\Lambda_B^s N = \Lambda_B^a N = -115$ corresponding to $\gamma_A^{s,a} N = -24\hat{\gamma}$ and $\gamma_B^{s,a} N = -23\hat{\gamma}$. The free energy per area is normalized on the middle surface and the structure of diblock copolymers is adjusted with the distance from the center of curvature.

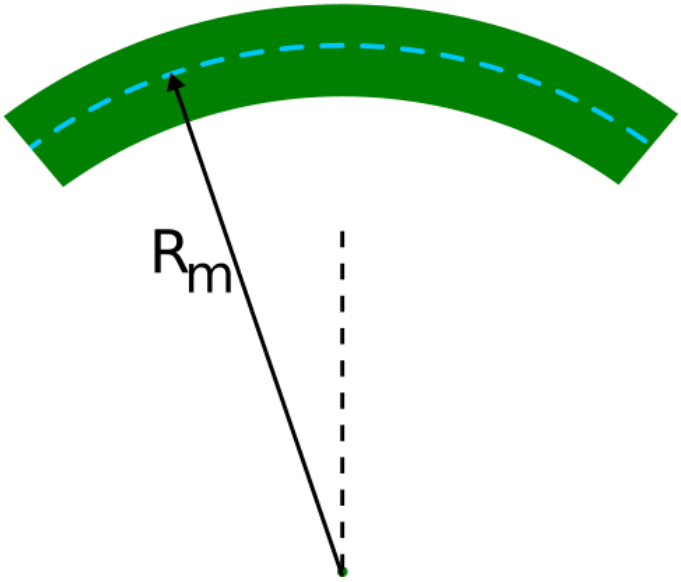

Figure 6.5: Schematic representation of the free-standing membranes. R_m is the radius of the middle surface of the membranes, which is the surface of reference.

We calculate the free energy per area as a function of the curvature radius $1/R_m$ of the middle surface of the free-standing membranes (see figure 6.5) for the two cases where cylinders are aligned parallel $C_{\parallel}$ or perpendicular $C_{\perp}$ to the direction of the main curvature. In each orientation of the alignment, the film thickness h and the wavelength of the characteristic pattern λ are optimized to obtain the lowest free energy state. This process is applied for every curvature. To be more specific, for each curvature, we minimize the free energy per area with respect to both, thickness and lateral distance. For example, figure 6.6 presents the free energy per area as a function of the film thickness at three different curvatures $k = 0.01$, $k = 0.05$ and $k = 0.1$, for the perpendicular configurations at the chemical potential $\mu = (2.5 + \ln G)k_B T$. We show here only three different values of curvature just to demonstrate the optimization process. By fitting the free energy per area F/A to a polynomial,

which is a third order in the thickness ($f(x) = ax^3 + bx^2 + cx + d$), we get the minimum free energy and the optimal thickness of membranes for the individual curvature. Afterwards, we vary the curvature $1/R_m$ of free-standing membranes and calculate the free energy per area as a function of the center curvature $1/R_m$ of the middle surface.

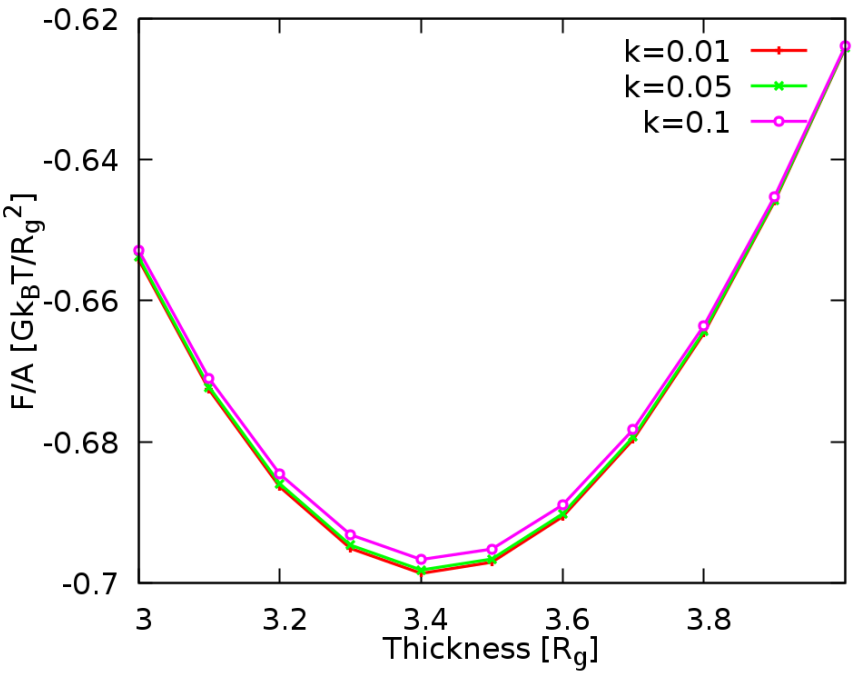

Figure 6.6: Free energy per area of the $C_\perp$ configurations as a function of the film thickness at different curvatures with the chemical potential $\mu = (2.5 + \ln G)\, k_B T$. In this figure we show three curvatures $k = 0.01$, $k = 0.05$ and $k = 0.1$ as an example.

Figure 6.7 shows the resulting density profiles for the parallel (panel a) and the perpendicular (panel b) configurations in a free-standing membrane system with a relatively large curvature ($R_m = 9Rg$). In panel c), we also show the density profile of the A-block through the center of cylinders in both, normal ($\mathbf{u_n}$) and tangential ($\mathbf{u_t}$) directions. Note that the density profiles along the tangential and normal directions with regard to the substrate surface only present very small difference between the perpendicular and parallel configurations. It indicates that the curvature does neither affect the position of the cylinder with regard to the plane of symmetry nor the segregation strength. Here we find that the optimum inter-cylinder spacing is $\lambda \sim 3.6R_g$ for either parallel or perpendicular configurations. It is slightly smaller than the bulk value, $\lambda_{bulk} \sim 3.7R_g$. The ratio, $\lambda/\lambda_{bulk} \sim 0.97$, is in good agreement with the SCFT calculations and experiments on flat substrates from a previous study [80]. It was found that in thin films the unit cell is stretched perpendicular to the plane of the films resulting in lateral distances smaller than those in the bulk [80, 82].

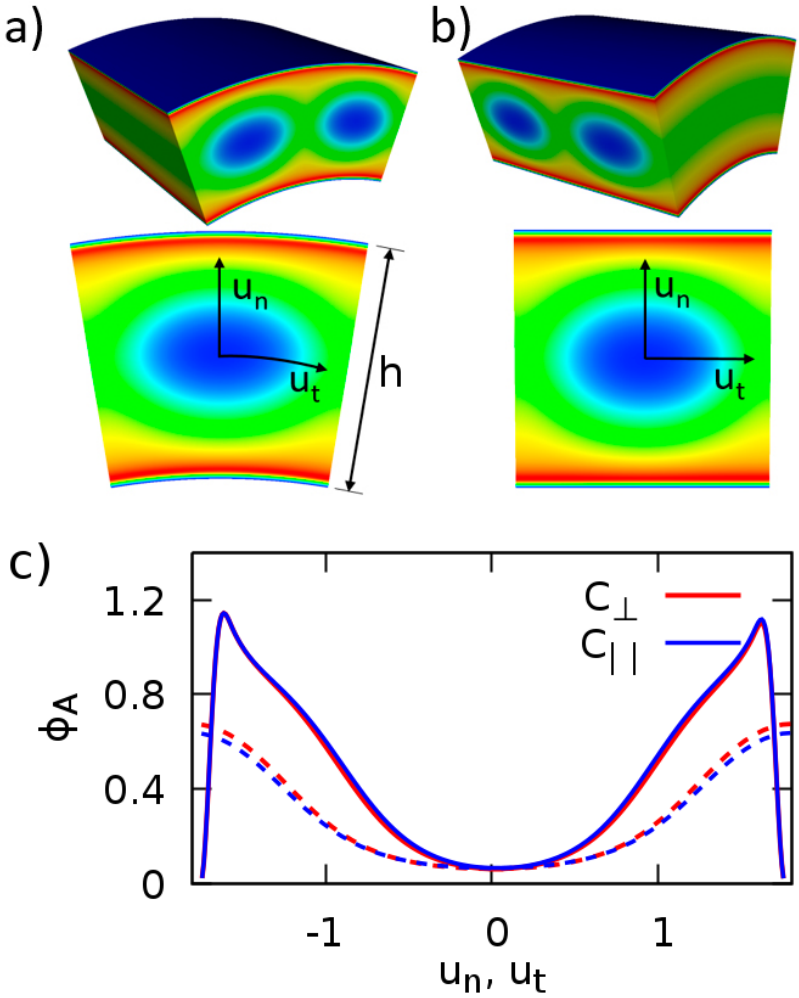

Figure 6.7: Density profiles of free-standing membranes obtained through the SCF calculation. Panel a) shows a parallel configuration and panel b) shows a perpendicular configuration. Here the value of the radius curvature is $R_m = 9R_g$. $\mathbf{u_n}$ and $\mathbf{u_t}$ are the unit vectors along the normal and tangential directions with respect to the substrate. The bottom panel c) show the density profile of the A-block through the center of the cylinders along the normal (two solid lines) and tangential (two dashed lines) directions with regard to the substrate.

Figure 6.8 presents the total density of the diblock copolymer membranes ($\phi_A + \phi_B$) through the center of cylinders along the direction normal to the substrate with the radius curvature $R_m = 9R_g$ and the film thickness $h = 3.5R_g$. It is noted that the total density is nearly constant within a distance of about $0.5R_g$ from the center of the membranes. However, the total density changes only slightly when we go further from the center of the membranes because the diblock copolymer melt studied here is compressible. Moreover, there is a bump close to the surfaces, i.e., the total density increases dramatically. This is because the surface interactions are quite strong, therefore more copolymers are attracted to the surfaces.

We also analyze the optimal thickness of the free-standing membranes as we know that the film thickness plays an important role in the result of mor-

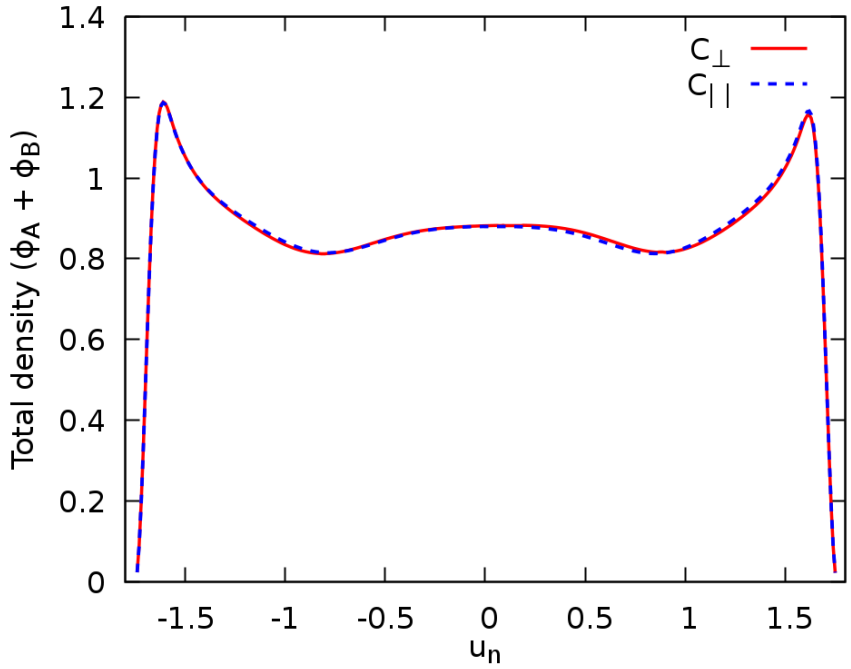

Figure 6.8: Total density profiles of free-standing membranes through the center of cylinders along the normal direction with regard to the substrate of the parallel and perpendicular configurations at the radius curvature $R_m = 9R_g$.

phologies [32, 80, 108, 109]. The value of the energetically favored thickness is similar for both the parallel and perpendicular configurations. It is $h \approx 3.4\,R_g$ for the chemical potential $\mu = (2.5 + \ln G)k_BT$ while it slightly increases up to $h \approx 3.5\,R_g$ for the chemical potential $\mu = (2.55 + \ln G)k_BT$. This increase of the thickness is reasonable since the number of diblock copolymers increases with the chemical potential. Note that while for the perpendicular configuration $C_\perp$ the thickness h slightly increases as the curvature increases, there is a stronger dependence for the parallel configuration $C_{||}$, where h decreases when the curvature increases. Moreover, the thickness h decreases more rapidly at large curvatures than that at small curvatures. This means that the perpendicular configuration is slightly stretched whereas the parallel configuration is slightly compressed compared to planar film, whose curvature vanishes $k = 0$. However, the change in the thickness with respect to the curvature is small compared to the thickness of flat films. Therefore, none of these features appear to be severely affected by the curvature within the wide range of curvatures explored here.

The behavior of the free energy per area as a function of the curvature for the perpendicular $C_\perp$ and parallel $C_{||}$ configurations is shown in figures 6.11 and 6.12 with the chemical potential $\mu = (2.5 + \ln G)k_BT$ and $\mu = (2.55 + \ln G)k_BT$, respectively. The data are treated with the corresponding free energy correction due to the discretization error. In order to obtain these free energy profiles, we determine the energy minimum of the individual curvature. At zero

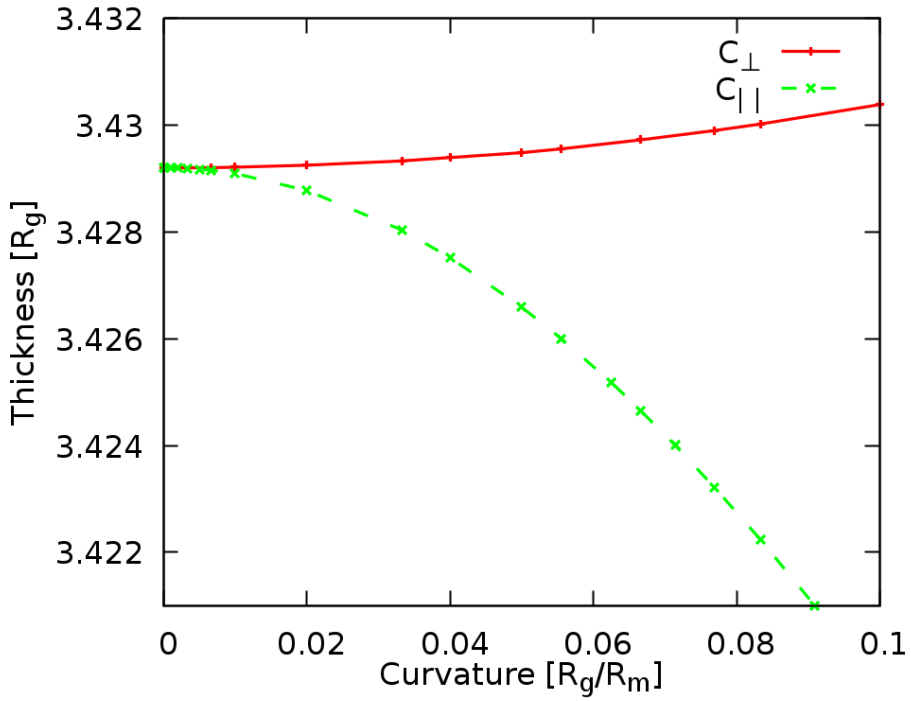

Figure 6.9: The minimum-energy thickness as a function of the curvature for the $C_{||}$ and $C_{\perp}$ configurations with the chemical potential $\mu = (2.5 + \ln G)k_B T$.

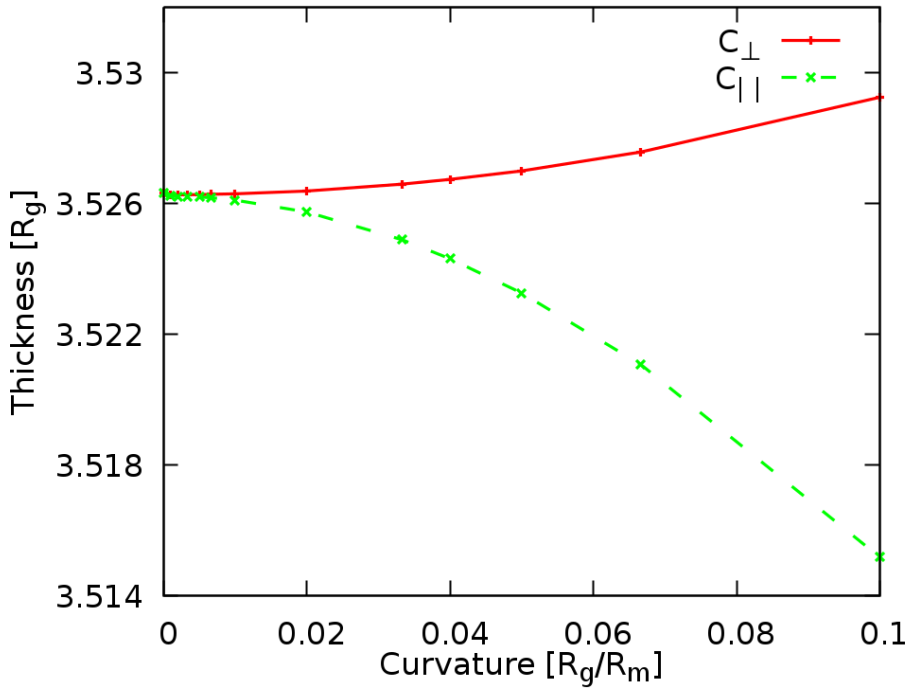

Figure 6.10: The minimum-energy thickness as a function of the curvature for the $C_{||}$ and $C_{\perp}$ configurations with the chemical potential $\mu = (2.55 + \ln G)k_B T$.

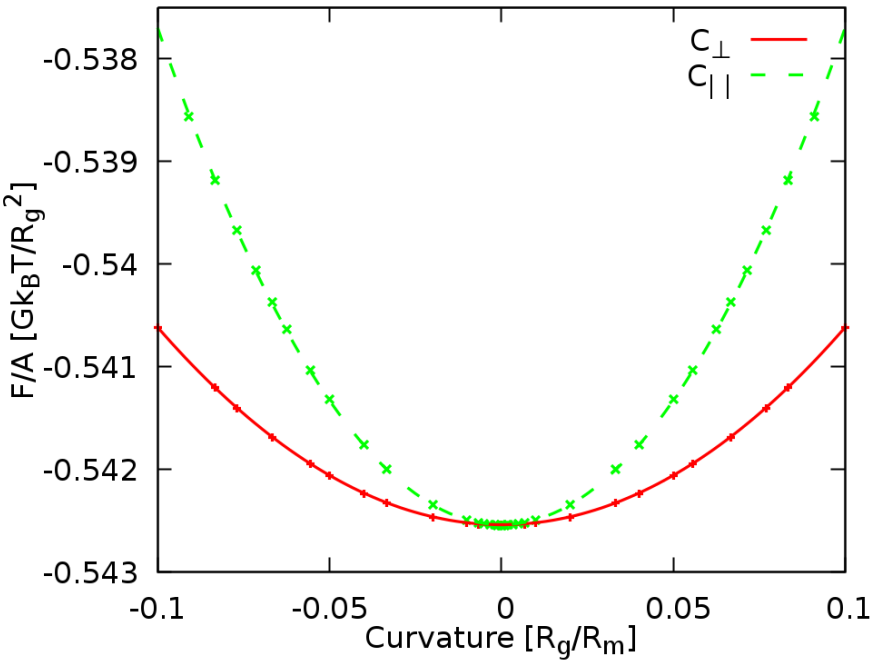

Figure 6.11: Free energy per area as a function of curvature for the parallel ($C_{||}$) and perpendicular ($C_{\perp}$) configurations with the chemical potential $\mu = (2.5 + \ln G)k_B T$.

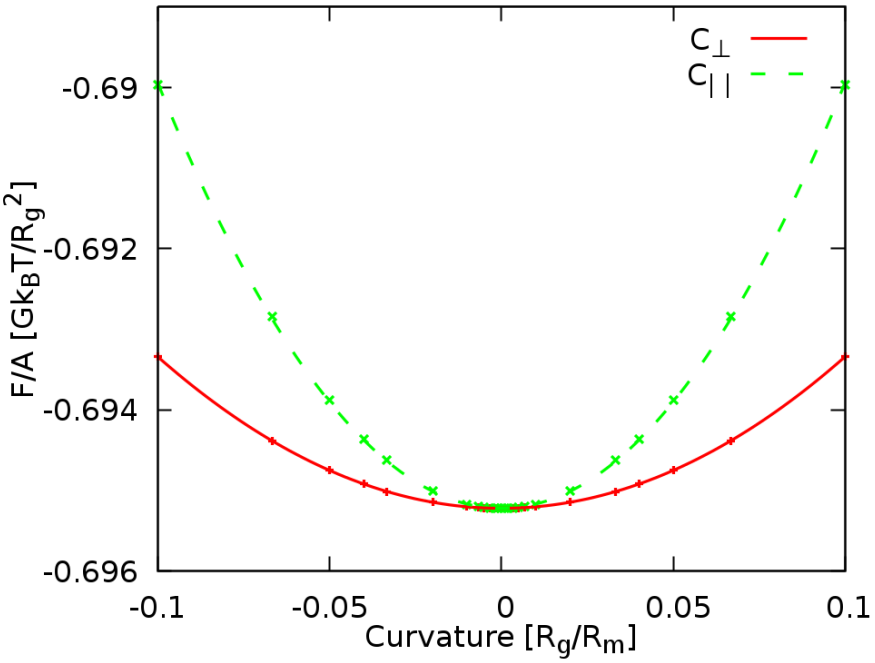

Figure 6.12: Free energy per area as a function of curvature for the parallel ($C_{||}$) and perpendicular ($C_{\perp}$) configurations with the chemical potential $\mu = (2.55 + \ln G)k_B T$.

curvature, diblock copolymer membranes are confined in the planar substrates. The free energy per area has lowest value at zero curvature. This implies that the diblock copolymer chains here are in the most relaxed state. As the curvature increases, the bending of the confined surfaces begins. It has an impact on the free energy as we observe in figures 6.11 and 6.12. The free energy per area increases as the curvature increases for either the perpendicular or parallel configurations. It grows faster in the parallel configuration since the free energy curve of the perpendicular configuration (the red curve) is flatter. The increase of the free energy per area is a result of either chain-stretching in the thicker films or chain-compression in the thinner films compared to the flat confinement. It also suggests that the presence of geometric constraints leads to the elastic deformation of the diblock copolymer patterns from the stable structures in the flat geometry.

We compute the free energy per area profiles to study the effect of the curvature of the substrate on the orientation of diblock copolymer free-standing membranes. We observe that the free energy per area of the perpendicular configuration is always lower than that of the parallel configuration at the same curvature. It implies that the perpendicular orientation is energetically favored. This effect is more pronounced at large curvature since the difference of the free energy per area increases with the curvature. This implies that the curvature acts as a guiding field for the orientation of diblock copolymer patterns [81, 110]. Our results are in a good agreement with the experimental results, where the membrane setup is close to ours [81]. They studied a monolayer of cylinder-forming of diblock copolymer PS-PEP. First, they thermally annealed the free-standing membranes at T=363K, above the glass transition temperature of PS block ($T_g \sim 330K$) and below the order-disorder transition temperature of the block copolymer ($T_{ODT} = 417K$). The annealing is kept until a prescribed orientational correlation length of $\sim$ 200nm is obtained [40]. Then they cooled it down to room temperature. Afterwards, they used atomic force microscopy (AFM) to view the structures of the free-standing membranes. The result is shown in figure 6.13, where the height and cylinder locations are measured simutaneously.

We can see the presence of defect structures which were formed during the annealing procedure. They cause the disruption in the order of patterns. The shape of membranes is a result of a competition between a strain field of defects, the bending energy associated with the curvature of membranes, and the membranes tension [40]. They also observed the coupling mechanism between the orientation of patterns and the local mean curvature of membranes. It is clearly seen that the wrinkles strongly tend to be oriented either parallel ($C_{||}$) or perpendicular ($C_{\perp}$) with respect to the underlying cylinders, though the different defects present in the membranes are competing to impose an out-of-plane deformation in order to relax their elastic distortions. Such a coupling mechanism is more clear from the histogram shown in figure 6.13. The data suggest that diblock copolymer membranes have preferential local orientation with respect to the director of the maximum principal curvature. It also suggests that the bending energy is anisotropic and coupled to the liquid crystal-

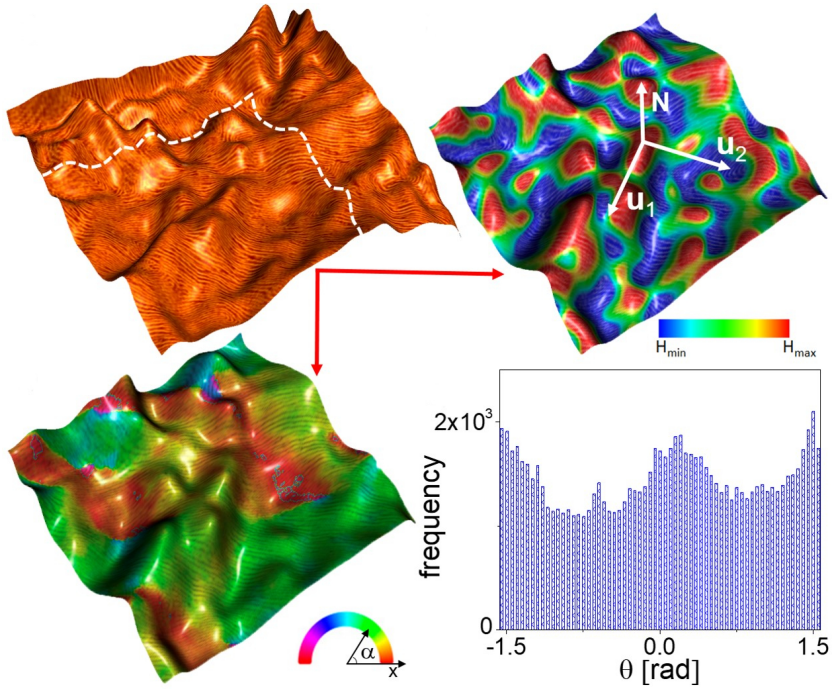

Figure 6.13: Panel a): AFM phase-height image of a free-standing thin film (image size: 2.6 μm × 2.6 μm). Panel b): Local mean curvature for the membranes shape. Here the vectors $\mathbf{u}_{1,2}$ indicate the directions of the principal curvatures and **N** is the normal vector to the membrane surface ($H_{max} = -H_{min} = 3.84 \times 10^{-3} nm^{-1}$). Panel c): Local orientation of the director field α of the pattern with regard to the x-axis. Panel d): Histogram showing the correlation between the underlying pattern and the local orientation of membrane wrinkles. This figure is adapted from the reference [81].

line order of the block copolymers. These results are in very good agreement with the predictions from our SCFT calculations.

Note that the development of a preferred orientation ($C_\perp$) indicates that the anisotropic elastic parameter in equation 6.10, $\kappa' > 0$.

The free energy expression F_{ani} in equation (6.10) not only describes the anisotropy of the elastic energy in nematic membranes, but also the coupling between the orientation of patterns and the curvature in the supported nematic films. Here, we write the expression of F_{ani} again for convenience:

$$F_{ani} = -\frac{\kappa'}{2}(k_1 - k_2)(2H - c_0')\cos(2\theta) - \frac{\kappa''}{2}(H^2 - K)\cos(4\theta)$$

In the case $\kappa'' > 0$, the second term prefers the parallel ($\theta = \pi/2$) and perpendicular ($\theta = 0$) orientations over intermediate orientations ($0 < \theta < \pi/2$). This provides an explanation for the experimental results of the free-standing membranes shown in figure 6.13 and later for the results of thin films in figure 6.22 (see in next section 6.5.2) [81].

We also investigate the bending constant κ of the diblock copolymer free-standing membranes. As noted earlier, the free energy per area can be described by the Helfrich formula $F_{HC} = \frac{\kappa_b}{2}(2H - c_0)^2 + \kappa_g K$. We apply this

to study the free-standing membranes here. We have the Gaussian curvature $K = 0$ due to the geometry of cylinderical surfaces and the $c_0 = 0$ due to the symmetry of the membranes. Therefore, the free energy per area grows almost quadratically with the curvature:

$$\frac{F}{A} = \frac{\kappa}{2R_m^2} \tag{6.22}$$

We can calculate the bending stiffness parameters for the $C_{||}$ and $C_{\perp}$ configurations using equation 6.22. By fitting the free energy per area to a quadratic order of the mean curvature, we extract the bending constant for the parallel ($\kappa_{||}$) and perpendicular ($\kappa_{\perp}$) configurations. For example, at the chemical potential $\mu = (2.5 + \ln G)k_BT$, the bending constants are

$$\begin{aligned} \kappa_{||} &= (0.968 \pm 0.002)Gk_BT \\ \kappa_{\perp} &= (0.395 \pm 0.002)Gk_BT \end{aligned}$$

On the other hand, when the chemical potential $\mu = (2.55 + \ln G)k_BT$, the bending constants slightly decreases for the perpendicular configuration and slightly increases for the parallel configuration. They are:

$$\begin{aligned} \kappa_{||} &= (1.056 \pm 0.002)Gk_BT \\ \kappa_{\perp} &= (0.376 \pm 0.002)Gk_BT \end{aligned}$$

Comparing this with equation (6.10) of the anisotropic energy F_{ani} and using the geometric properties of cylindrical surfaces $k_1 = \pm 1/R_m$, $k_2 = 0$, we can deduce the anisotropic elastic parameter $\kappa' = (\kappa_{||} - \kappa_{\perp})$. Such a calculation gives $\kappa' = 0.573Gk_BT$ and $\kappa' = 0.68Gk_BT$ for systems with the chemical potential $\mu = (2.5 + \ln G)k_BT$ and $\mu = (2.55 + \ln G)k_BT$, respectively. We note that here, the bending constants are given in the units of Gk_BT, though it is more useful to present them in units of k_BT. We use the experimental data from [81], to calculate the dimensionless Ginzburg constant $G = \frac{\rho_0}{N}R_g^3$. For this we use the molecular weight of diblock copolymer PS-PEP, $M = 17500\ g/mol$, and assume an average copolymer density of $0.861\ g/cm^3$ (at $T = 363K$). Therefore, the value of the Ginzburg constant is

$$G = \frac{\rho_0}{N}R_g^3 = \frac{0.861\ g/cm^3}{17500\ g} \cdot (6.02 \cdot 10^{23}) \cdot R_g^3 \tag{6.23}$$

where $(6.02 \cdot 10^{23})$ is the Avogadro constant, which denotes the number of molecules per mol. Furthermore, the lateral spacing between the cylinders is $\lambda = 3.6R_g$. Matching it with the corresponding experimental value 21 nm [80], we can determine the value of the radius of gyration as $R_g = 5.8 \cdot 10^{-7}cm$. Inserting this into the equation (6.23), we obtain the dimensionless Ginzburg constant:

$$\begin{aligned} G &= \frac{0.861}{17500} \frac{1}{(5.8^{-1} \cdot 10^7)^3 \cdot R_g^3} \cdot (6.02 \cdot 10^{23}) \cdot R_g^3 \\ &\approx 5.77 \end{aligned} \tag{6.24}$$

Therefore, the anisotropic parameter is

$$\begin{cases} \kappa' &= (\kappa_{||} - \kappa_{\perp}) = 0.573 G k_B T \approx 3.3\, k_B T, \qquad \mu = (2.5 + \ln G) k_B T \\ \kappa' &= (\kappa_{||} - \kappa_{\perp}) = 0.680 G k_B T \approx 4\, k_B T, \qquad \mu = (2.55 + \ln G) k_B T \end{cases}$$

These values correspond to $\kappa' \approx 1.4 \cdot 10^{-13}$ erg and $\kappa' \approx 1.6 \cdot 10^{-13}$ erg at room temperature, for the chemical potential $\mu = (2.5 + \ln G) k_B T$ and $\mu = (2.55 + \ln G) k_B T$, respectively. On the contrary, the total bending energy of the membranes has been estimated to be in the order of $\kappa_b \sim 10^{-9}$ erg, which is much higher due to the large contribution of the glassy PS block [40]. Hence, the influence of κ' on the membrane shapes is presumably negligible.

Furthermore, as suggested by the second term $(-\kappa''/2(H^2 - K)\cos(4\theta))$ in equation (6.10) of the anisotropic energy F_{ani}, both, $C_{\perp}$ and $C_{||}$ configurations, represent the local free energy minima with respect to variations of the angle θ between cylinders and the direction of the largest curvature. In order to examine the stability of the two extremum configurations $C_{\perp}$ ($\theta = 0$) and $C_{||}$ ($\theta = \pi/2$) in comparison to the intermediate configurations, we thus investigate the free energy per area of the θ-configuration at a given curvature by the SCFT, and then compare the free energies of the three orientations: $C_{\perp}$, $C_{||}$ and θ-configuration. Specifically, we keep the radius of the curvature $R_m = 50 R_g$ fixed (which corresponds to the curvature $k_1 = 0.02$), and then vary the values of the angle θ in the range $(0 : \pi/2)$. In order to calculate the free energy per area of the tilted configuration, we use the two setups with the boundary conditions as discussed in the section 6.4, one for the small values of θ close to 0 and the other for the value of θ close to $\pi/2$. We combine the results obtained from the two setups to get the free energy as a function of the entire range of the values of $\theta \in [0 : \pi/2]$. The free energy is also minimized with respect to the pattern distance and the thickness as it is done for the configurations $C_{\perp}$ and $C_{||}$. Here we only do the calculations with the chemical potential $\mu = (2.55 + \ln G) k_B T$. Figure 6.14 presents the free energy per area as a function of the tilt angle θ.

Note that the free energy per area of the titled orientation configuration first increases as the tilt angle increases from $\theta = 0$ (which corresponds to the perpendicular configuration), reaches the maximum and then decreases as the tilt angle approaches to $\theta = \pi/2$ (which corresponds to the parallel configuration). Since the range of the free energy per area F/A here is small, we have to be careful while determining the equilibrium state at a given tilt angle θ. We use different initial configurations to ensure that we get the real stable state. This result enforces for the bimodal explanation from the above formula of F_{ani} and also the histograms obtained from experiments, that the two configurations $C_{\perp}$ and $C_{||}$ are the local minima in the free energy landscape of the free-standing membranes. It is also consistent with Napoli's work [111], where they studied the alignment of nematic shells on a cylindrical substrate. They also found that the parallel and perpendicular orientations are two stable states with respect to the intermediate orientations.

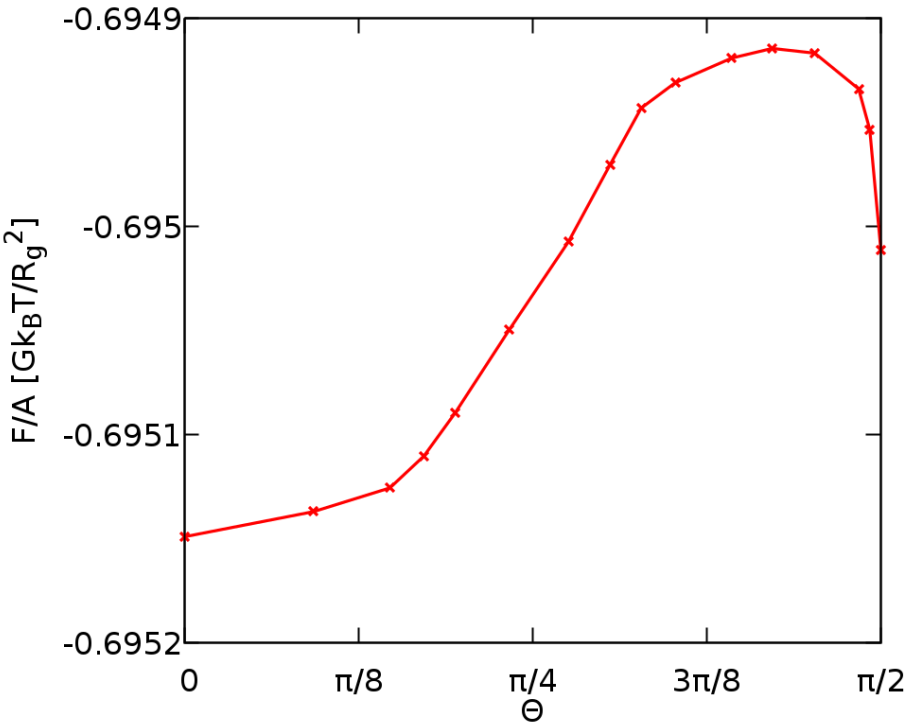

Figure 6.14: Free energy per area as a function of the tilt angle θ between the cylinders and the direction of the largest curvature at a given radius of curvature $R_m = 50\,R_g$. The chemical potential is $\mu = (2.55 + \ln G)k_BT$.

6.5.2 *Supported Thin Film*

The situation is different when looking at copolymers ordering in the curved supported films, where the curvatures are kept fixed and the energy differences of order k_BT do have a significant influence on the selection of the pattern orientations. When studying this case, the appropriate reference surface is the substrate which is kept fixed when minimizing the surface free energy. It is different from the free-standing membrane study since the up-down symmetry in membranes is no longer valid. We study block copolymers confined in two geometries. The first one, whose surface is inward (concave), has negative mean curvature $H < 0$ as illustrated in figure 6.15a. The second one, whose surface is outward (convex) has positive curvature $H > 0$ as presented in figure 6.15b. In this approach, the structure of thin films is adjusted with the distance from the substrates. In the SCF calculations, the free energy is thus minimized with respect to the pattern dimensions and the film thickness for the fixed substrate area and the curvature. Thereafter, the SCFT data are corrected for the discretization error.

Furthermore, surface interaction energies may be the same or different at the substrate and the air surface. As mentioned above, we consider both situations where the surface interactions are either symmetric to each block as for the free-standing membrane study or the surface interactions are asymmetric. For

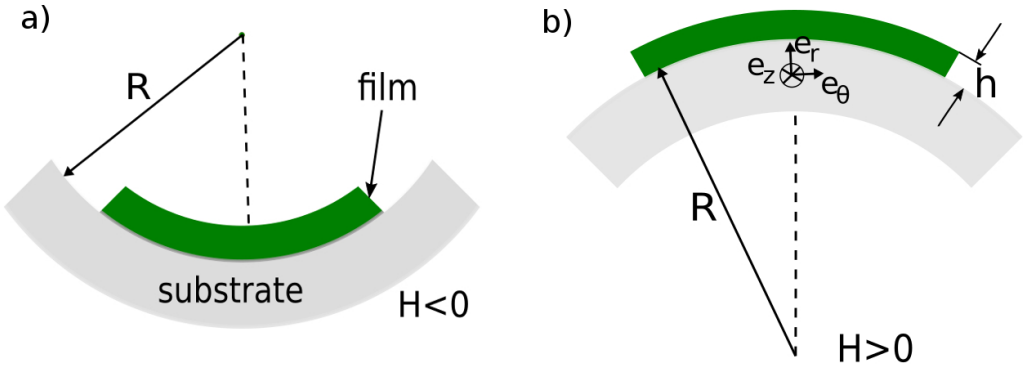

Figure 6.15: Scheme of the curved supported thin film: panel a) we call inward or concave film with a negative mean cuvature $H < 0$, panel b) we call outward or convex film with a positive mean curvature $H > 0$.

the symmetric surface interaction, we use the same surface interactions and the chemical potential $\mu = (2.5 + \ln G)k_BT$ as in the free-standing membranes. For asymmetric surface interactions, we study two cases: (I)- The affinity of the substrate to the A-block is stronger than the free surface, and (II)- The affinity of the free surface to the A-block is stronger than the substrate. The chemical potential is slightly increased up to $\mu = (2.55 + \ln G)k_BT$, otherwise the supported thin films with positive curvature are not stable or metastable.

6.5.2.1 *Supported thin films with symmetric surfaces*

As noted above, we use the same parameters like for the free-standing membranes. The strength of interaction between the substrate, free surface and each block are $\Lambda_A^a N = \Lambda_A^s N = -120$, and $\Lambda_B^a N = \Lambda_B^s N = -115$. These correspond to $\gamma_A^{s,a} N = -24\hat{\gamma}$ and $\gamma_B^{s,a} N = -23\hat{\gamma}$. The chemical potential of the thin films is set to $\mu = (2.5 + \ln G)k_BT$. We perform the SCFT calculations to obtain the minimum free energy of the two extremum orientation configurations, $C_\perp$ and $C_{||}$ similarly as we did for the free-standing membranes. To compare the free energy of the two orientation configurations, we calculate the difference of the free energy per area between the two configurations at the same curvature as below:

$$\frac{\Delta F}{A} = \frac{F_{||} - F_\perp}{A} \tag{6.25}$$

Figure 6.16 presents the difference of free energy per area of the two configurations as a function of the curvature. Note that the free energy difference $\Delta F/A$ is always positive in both the outward and the inward thin films and it increases as the curvature increases. Nevertheless, the free energy difference is small. It is in the order of $10^{-3}\ Gk_BT$ corresponding to $(10^{-3} : 10^{-2})\ k_BT$. This implies that the perpendicular configuration has lower free energy than the parallel one. In other words, the $C_\perp$ configuration is more stable than the $C_{||}$ one. This result is similar to that observed in the free-standing membrane study. This suggests that the curvature of the substrates imposes the local orientation of patterns.

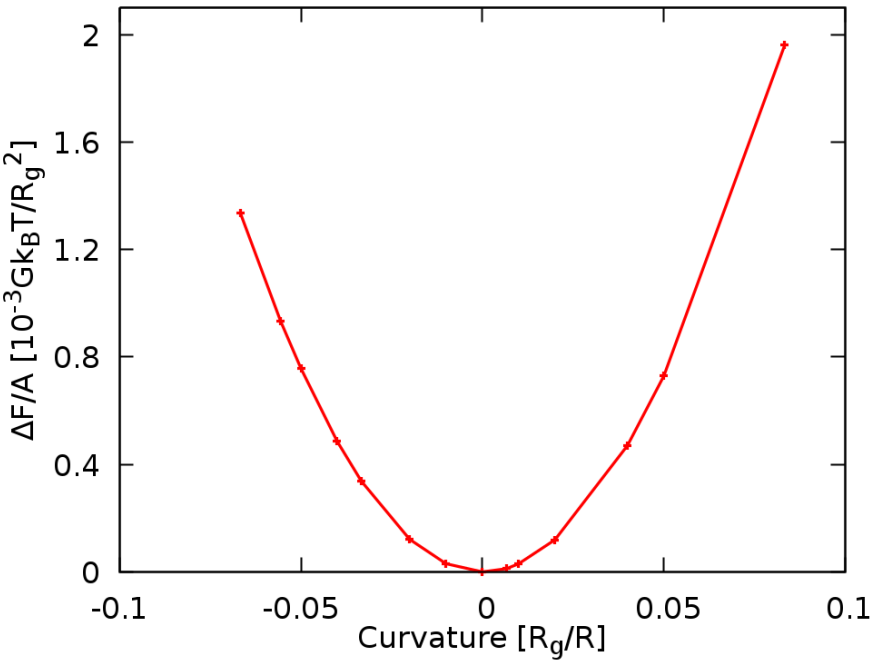

Figure 6.16: The difference of the free energy per area of the parallel and perpendicular configurations $\Delta F/A = (F_{||} - F_{\perp})/A$ as a function of the curvature, in the thin film with symmetric surfaces to each block A and B. The input parameters of the system are: $\Lambda_A^{s,a}N = -120$, $\Lambda_B^{s,a}N = -115$, and $\mu = (2.5 + \ln G)k_B T$.

We also analyze the behavior of the film thickness which is an important and interesting factor in block copolymer morphologies. Figure 6.17 shows the minimum-energy thickness of both, the perpendicular and parallel configurations of the thin films as a function of substrate curvature (when there is a symmetric surface interaction for each block). For the outward thin films with positive curvature ($H > 0$), the optimal thickness increases with the curvature for either configurations $C_{\perp}$ or $C_{||}$, implying thickening of the films. In contrast, for the inward thin films with negative curvature ($H < 0$), the optimal thickness decreases as the curvature increases irrespective of the orientation of the patterns. Besides, the values of the thickness of the parallel and the perpendicular configurations are almost the same at small curvature. However, they are different at higher curvatures, in which the perpendicular configuration film is slightly thicker than the parallel configuration film. These results are consistent with the behavior of the film thickness obtained in the free-standing membranes.

6.5.2.2 *Supported thin films with asymmetric surfaces*

For the first case (I) of surface interaction parameters in the curved supported thin films, where the free surface attracts the A-block stronger than the substrate, we use the symmetric conditions for the B-block at both surfaces with parameters $\gamma_B^a N = \gamma_B^s N = -30$. These parameters correspond to $\gamma_B^{a,s} N = -6\hat{\gamma}$.

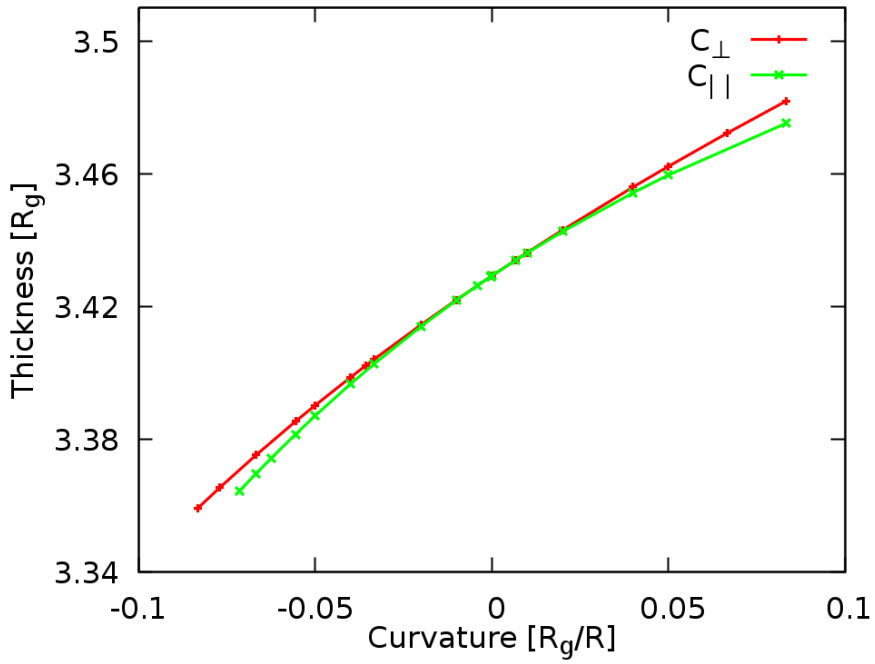

Figure 6.17: The optimum thickness of the parallel and perpendicular configurations in supported thin films with symmetric surfaces as a function of the curvature. The interaction parameters of the system are: $\Lambda_A^{s,a}N = -120$, $\Lambda_B^{s,a}N = -115$, and $\mu = (2.5 + \ln G)k_BT$.

The surface interactions for the A-block are asymmetric. They are chosen to be $\gamma_A^a N = -100$ and $\gamma_A^s N = -50$, corresponding to $\gamma_A^a N = -20\hat{\gamma}$ and $\gamma_A^s N = -10\hat{\gamma}$, at the free (air) surface and the substrate, respectively. We perform SCFT simulations to obtain the minimum free energy of the configurations in the both directions, parallel and perpendicular to the substrate of the thin films at different curvatures (similar to the previous studies). In order to understand the stability of the two configurations, we also compare their free energies.

From figure 6.18, it is observed that the free energy difference $\Delta F/A = (F_{||} - F_{\perp})/A$ is always positive for the thin films with negative curvature and it increases with the curvature. However, this behavior of $\Delta F/A$ is not the same for the thin films with positive mean curvature $H > 0$. In such systems, $\Delta F/A$ is negative at small curvatures ($H \lesssim 0.033$) and becomes positive at higher curvatures. Nonetheless, the difference of the free energy $\Delta F/A$ is small, and is in the order of $10^{-3}\, Gk_BT$ (equivalent to $\sim (10^{-3} : 10^{-2})\, k_BT$). As a result, we have to be careful when identifying the stable morphologies of the thin films. From the data we note that the perpendicular phase is not always stable, but at small positive curvatures there exists a small regime where the parallel configuration $C_{||}$ has lower free energy than the perpendicular configuration $C_{\perp}$. This regime is emphasized by cyan-shade in figure 6.18. Additionally, for the thin films with $H < 0$ the free energy difference is more sensitive to the curvature as it grows faster with the curvature.

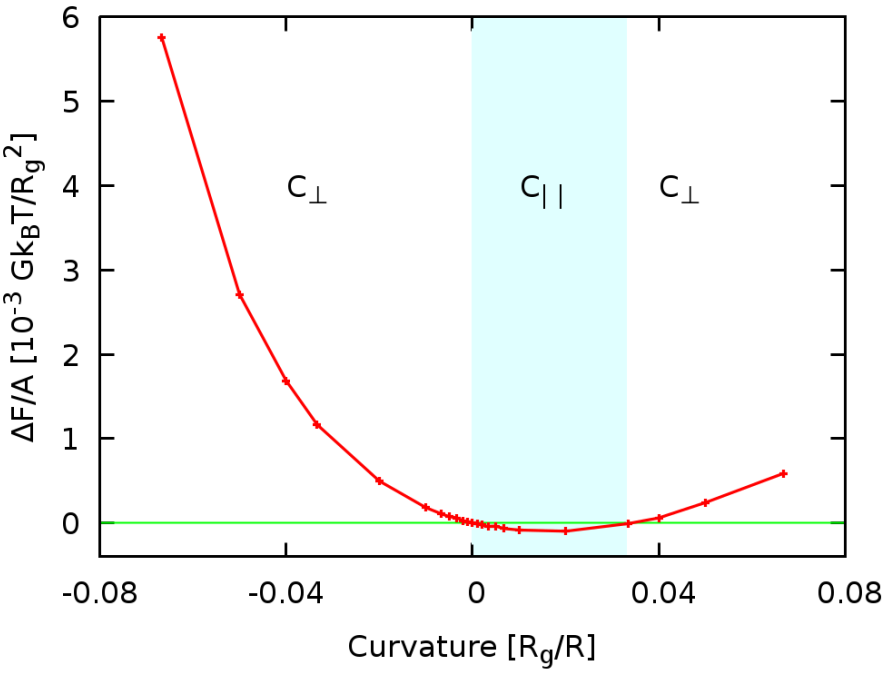

Figure 6.18: The difference of the free energy per area of the parallel $C_{||}$ and perpendicular $C_\perp$ orientation configurations $\Delta F/A = (F_{||} - F_\perp)/A$ for diblock copolymers in the curved supported thin films, where the surface interaction is the same for the B-block $\Lambda_B^s N = \Lambda_B^a N = -30$ but asymmetric for the A-block $\Lambda_A^s N = -50$, $\Lambda_A^a N = -100$. The chemical potential is fixed at $\mu = (2.55 + \ln G)k_B T$.

We also investigate the influence of the surface preference to the majority block (A) on the phase behavior of the supported thin films. We first make the asymmetry between the two surfaces to the A-block larger by increasing the affinity of the free surface to the A-block from $\Lambda_A^a N = -100$ up to $\Lambda_A^a N = -120$. It corresponds to $\Lambda_A^a N = -24\hat{\gamma}$. The other parameters are chosen as before, the symmetric conditions for the B-block $\Lambda_B^{s,a} N = -30$ and the chemical potential $\mu = (2.55 + \ln G)k_B T$. We also carefully determine the equilibrium state of the thin films in both the orientations $C_\perp$ and $C_{||}$. Afterwards, we compare their free energies by calculating the difference of free energy $\Delta F/A$ between the two configurations. The data are presented in figure 6.19.

The behavior of the free energy difference $\Delta F/A$ as a function of the curvature is similar to that reported in the figure 6.18. It is always positive for the negative curvature films and only at large curvatures for the positive curvature films. There is a small positive curvature regime ($H \lesssim 0.033$) highlighted by cyan-shade, in which $\Delta F/A < 0$ and it is more remarkably negative than that presented in the figure 6.18. At large curvatures, the difference of the free energy $\Delta F/A$ raises more steeply at negative curvature than at positive curvature.

After that, we reduce the degree of asymmetry between the free surface and the substrate to the A-block as well. We do that by increasing the strength of interaction at the substrate up to $\Lambda_A^s N = -70$, while keeping the other parameters the same, i.e., $\Lambda_B^{s,a} N = -30$ and $\mu = (2.55 + \ln G)k_B T$. A procedure,

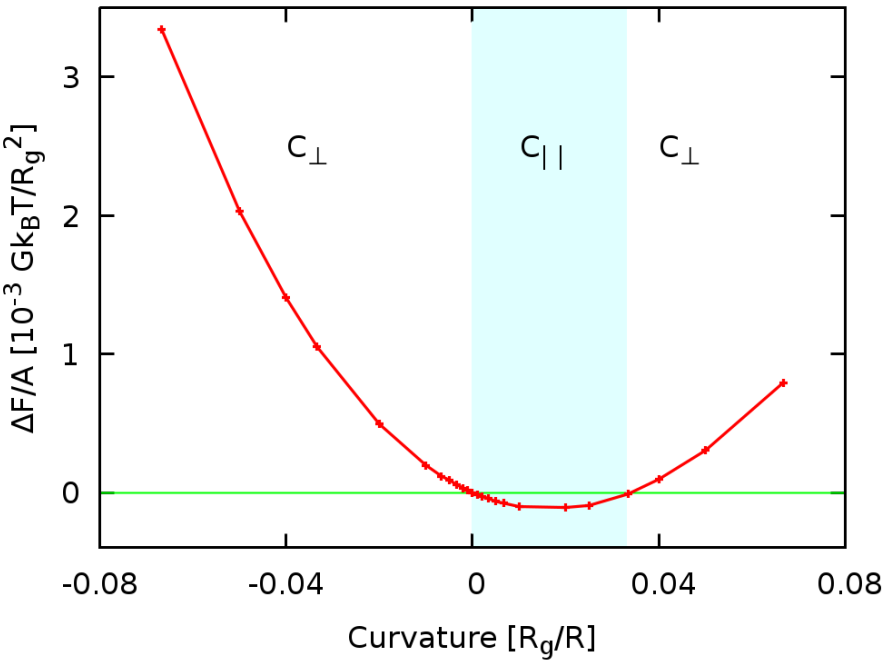

Figure 6.19: The difference of the free energy per area of the parallel $C_{||}$ and perpendicular $C_\perp$ orientation configurations $\Delta F/A = (F_{||} - F_\perp)/A$ for diblock copolymers in the curved supported thin films, where the surface interaction is the same for the B-block $\Lambda_B^s N = \Lambda_B^a N = -30$ but asymmetric for the A-block $\Lambda_A^s N = -50$, $\Lambda_A^a N = -120$. The chemical potential is fixed at $\mu = (2.55 + \ln G) k_B T$.

which is very similar to that presented in the previous sections, is employed to carry out SCFT calculations. We show the behavior of the difference of the free energy $\Delta F/A$ in figure 6.20. The results obtained here are very similar to that of the above mentioned asymmetric thin film systems. The perpendicular configuration is found to be stable at almost all the curvatures. This is because $\Delta F/A$ is found to be greater than zero for the entire regime except for the outward thin films with $H \lesssim 0.018$ (the region is emphasized by cyan-color). We also note that, when compared to the above asymmetric systems, the regime in which the parallel configuration is favored, becomes narrower, and the free energy difference $\Delta F/A$ is found to be less negative. If we continue to reduce the asymmetry between the two surfaces until they are symmetric, we will get back to the results obtained in section 6.5.2.1, in which the perpendicular configuration was always energetically preferred over the parallel configuration.

For the second case (II) in the supported thin films with asymmetric surface interactions, where the substrate attracts the A-block stronger than the air surface, we choose the parameters which are still symmetric for the B-block, $\Lambda_B^s N = \Lambda_B^a N = -30$, corresponding to $\Lambda_B^{a,s} N = -6\hat{\gamma}$. Whereas these interactions are asymmetric for the A-block $\Lambda_A^s N = -120$, $\Lambda_A^a N = -50$, corresponding to $\Lambda_A^s N = -24\hat{\gamma}$ and $\Lambda_A^a N = -10\hat{\gamma}$. The chemical potential is fixed at the same value as in the first case (I), i.e., $\mu = (2.55 + \ln G) k_B T$. We first find the minimum free energy of the two configurations $C_\perp$ and $C_{||}$. Then

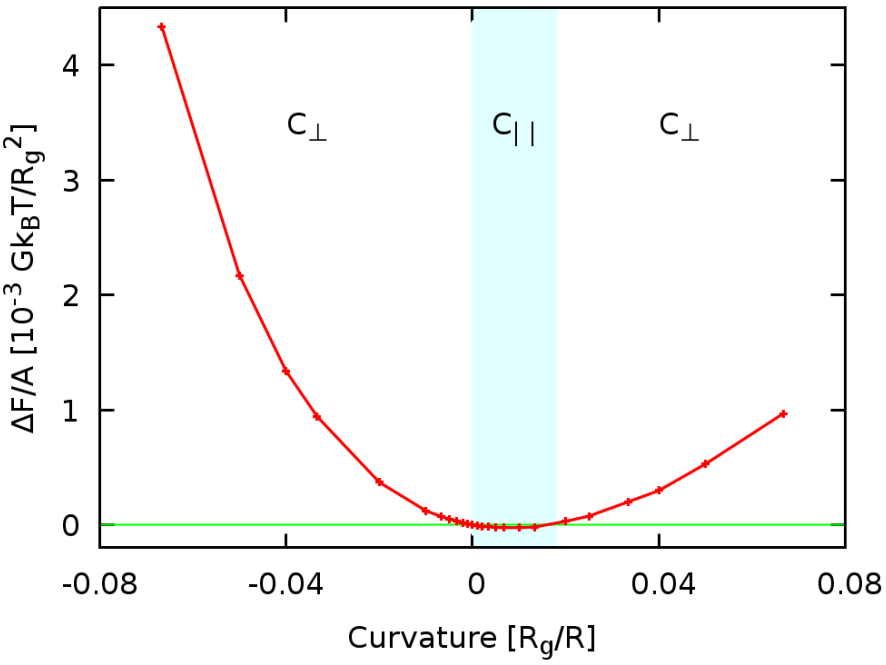

Figure 6.20: The difference of the free energy per area of the parallel $C_{||}$ and perpendicular $C_\perp$ orientation configurations $\Delta F/A = (F_{||} - F_\perp)/A$ for diblock copolymers in the curved supported thin films, where the surface interaction is the same for the B-block $\Lambda_B^s N = \Lambda_B^a N = -30$ but asymmetric for the A-block $\Lambda_A^s N = -70$, $\Lambda_A^a N = -100$. The chemical potential is kept at $\mu = (2.55 + \ln G)k_B T$.

we calculate the difference of free energy between them as a function of the mean curvature to analyze their relative stability to each other. The results are presented in figure 6.21.

Note that the free energy difference $\Delta F/A$ is always positive for the thin films with positive mean curvature $H > 0$ and it grows with the curvature. There is an alteration for the thin films with negative mean curvature $H < 0$: $\Delta F/A$ is negative at small curvatures ($H \lesssim 0.22$), then becomes positive at higher curvatures and increases as curvature increases. The difference of free energy here is also small as in the first case (I), it is in the order of $10^{-3}\ Gk_B T$. This behavior of $\Delta F/A$ suggests that the perpendicular configuration is always more stable for positive mean curvature films and only at high curvatures for the negative mean curvature films. However, at the small negative curvature regime, which is emphasized by a cyan-shade in figure 6.21, the parallel configuration is more stable. The results are similar to those for the choice of interaction parameters in the first case (I).

In both cases (I) and (II) of asymmetry in the surface interaction, the perpendicular configuration is more favorable at large curvatures (either positive or negative curvatures). However, at small curvatures, there exists a small regime with positive or negative mean curvature depending on which surface (free surface or substrate) has a stronger affinity to the A-block, where parallel configurations have lower free energy. These results are compatible with equation

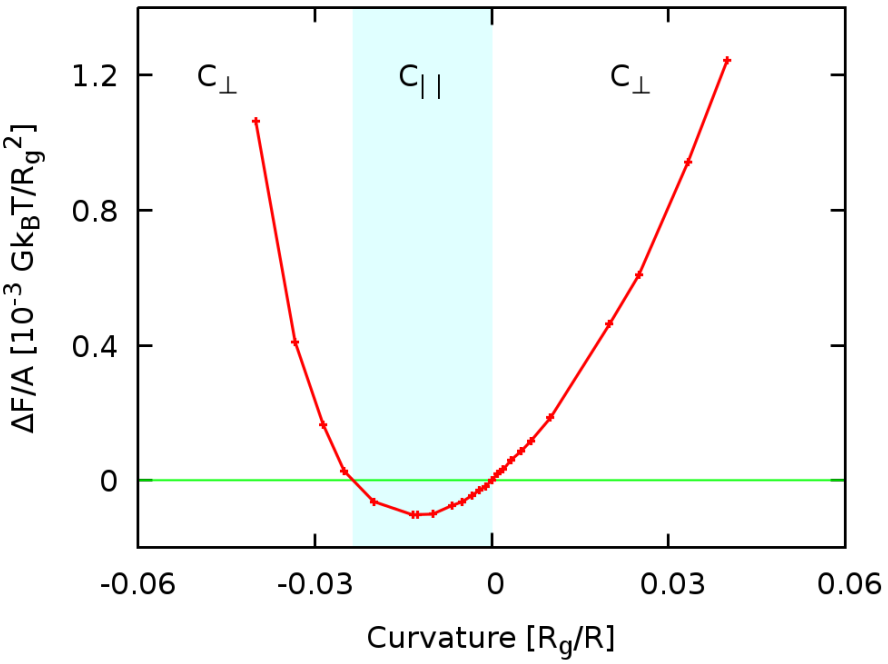

Figure 6.21: The difference of the free energy per area of the parallel $C_{||}$ and perpendicular $C_\perp$ orientation configurations $\Delta F/A = (F_{||} - F_\perp)/A$ for diblock copolymers in the curved supported thin films, where the surface interaction is symmetric for the B-block $\Lambda_B^s N = \Lambda_B^a N = -30$ but asymmetric for the A-block $\Lambda_A^s N = -120$, $\Lambda_A^a N = -50$. The chemical potential of the thin films is $\mu = (2.55 + \ln G)k_B T$.

(6.10) (for $\kappa' > 0$ and non-vanishing c_0' in the thin film system) and are also in good agreement with the experimental observations [81]. Indeed, figure 6.22b and figure 6.23 (which will be discussed more detail later) suggest that the locally preferred orientation switches or reorients from the perpendicular to the parallel direction in a region around the inflection point of the surface profile (green shaded areas in figure 6.22b). As a consequence, this switch of the preferential configuration induces defects in that region. Hence curvature can be used not only to orient patterns, but also combining with surface preference to generate defects at specific regions in space.

Now, we compare our SCFT results with the experimental results of the curved supported thin films conducted by Professor Vega's group. The systems in the experimental studies are very close to our SCFT studies.

As discussed above, in the experiment of diblock copolymer membranes, wrinkles are preferentially observed in the directions either parallel or perpendicular to the underlying cylinders. It is also noted that overall the perpendicular orientation is more favorable. Vega et al. obtained similar results related to the correlation between the orientation of the patterns and the geometry of the confinement for the thin films as well. The results are displayed in figures 6.22 and 6.23.

In such an experiment, they studied the diblock copolymer PS-PEP thin films. The films were annealed during different times at the temperature T=373K.

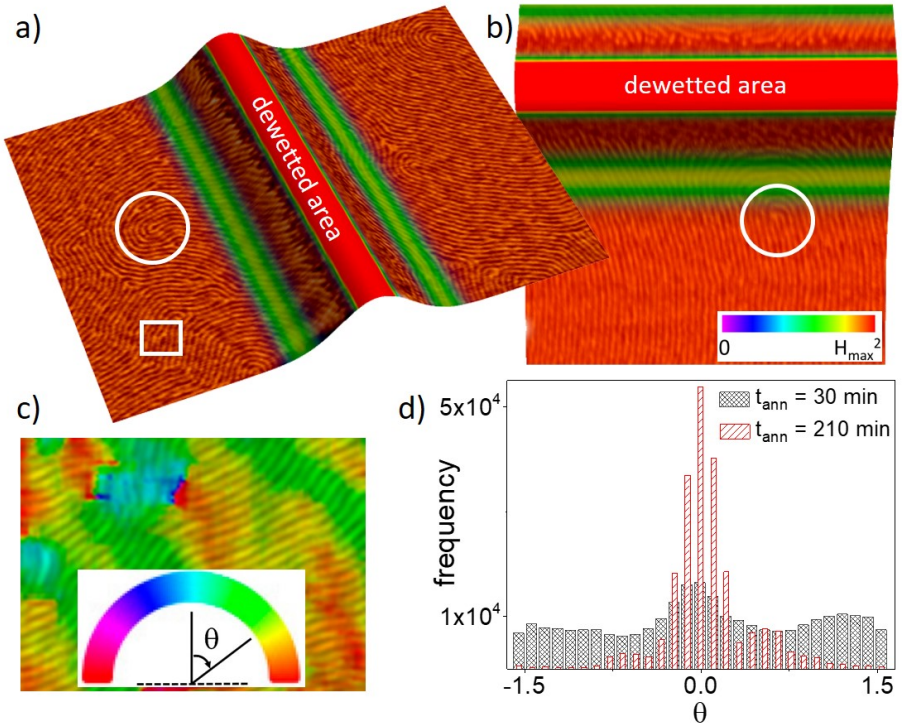

Figure 6.22: Panels a) and b) are 3D AFM phase-height images of the block copolymer thin film on a curved substrate after annealing at T=373K. They show the pattern configuration after different times of thermal annealing, 90 min and 3.5 h, respectively. Height scale: 80 nm from crest to valley, $H^2_{max} = 6.25\mu m^{-2}$). The presence of a dislocation and +1/2 disclinations has been emphasized with a rectangle and circles, respectively. Bottom panels: c) Local orientation of the smectic pattern (color map indicated at the bottom). d) Histograms showing the distribution of local orientations at the two different annealing times [81].

To image the configurations of the thin films, they employed AFM. During annealing, the thin films order via the annihilation of disclination and dislocation defects. In figure 6.22a (short time of annealing, 90 min), the thin films have a high density of defects. Additionally, the thin films located at the region with high curvature corresponding to the crest of the substrate become unstable and dewet. As the annealing time increases up to 3.5 h, there is a markedly increasing translational order in the systems, as shown in figure 6.22b. In addition, the histograms in figure 6.22d show that the distribution of local cylinder orientations θ at early annealing time (30 min) is bimodal, with two characteristic peaks separated by $\sim \pi/2$. These peaks correspond to two modes, the perpendicular and parallel configurations. During the first stage of coarsening, the parallel and perpendicular configurations compete with each other. After longer annealing times (3.5 h), the systems develop a preferential orientation through the annihilation of topological defects. In this, the orientation $C_\perp$ dominates. It can be clearly seen from the histogram, which becomes sharply peaked at the perpendicular orientation $\theta = 0$. This obseration confirms that the anisotropic elastic parameter $\kappa' > 0$ as we discussed above in our SCFT results. Note that the perpendicular orientation $C_\perp$ of PS cylinders provides

further evidence to the observation that the curvature of substrates acts as an effective guiding field for the pattern orientation.

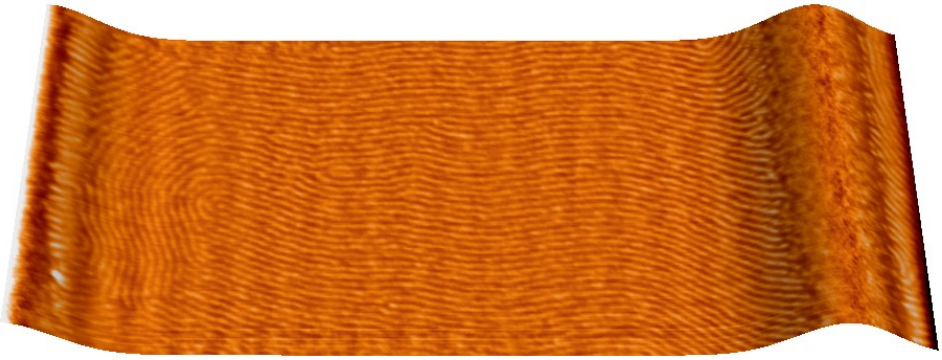

Figure 6.23: 3D AFM phase-height images of the block copolymer thin film lying on a curved substrate after 3.5 h of thermal annealing at T=373K. (image size: 2.5 μm x 1.0 μm). This figure is adapted from reference [81].

Furthermore, Vega et al. also observed that at the small curvature region (emphasized in green in figure 6.22b) and the region at the very left side of the thin films in figure 6.23, the diblock copolymer patterns switch the orientation from perpendicular to parallel. We can see that the parallel configuration is more common in that region. In addition, there are topological defects in that region as well. For example, a $+1/2$ disclination is emphasized by a white circle in figure6.22b. These experimental results support our SCFT results discussed above, in which we found that there is a narrow regime corresponding to the small curvature region where the parallel orientation is found to be more stable. This suggests that the curvature not only guides the alignment of texture but also causes the defects in a certain region.

There are other experimental and theoretical studies where it was investigated how the topography of the substrate affects the orientation of patterns, such as, corrugated substrates with sinusoidal [41, 112–114] and pre-patterned with square-wave in the substrate [29]. For example, Man et al. [113] employed SCFT to investigate how the substrate corrugation induces the in-plane alignment of block copolymers in a 3-dimensional system. However, they studied the formation of the lamellar phase, not the cylinder-forming phase as in this thesis. They found that the topography and preference toward to the blocks of the substrates together generate a synergy. This synergy dictates the preferential perpendicular lamellar phase. They compared the free energy of the two configurations $L_\perp$ and $L_{||}$. It was found that the free energy difference $\Delta F = F_{||} - F_\perp > 0$ is positive and increases as the corrugation amplitude increases (corresponding to the curvature increasing in our study).
Another example is the experimental work of Vega and co-workers [41]. They studied the dynamics of the ordering of cylinder-forming diblock copolymer PS-PEP deposited on a curved substrate. They proposed a coupling mechanism between the mean curvature of the substrate and the alignment of the diblock copolymers. They found that the texture can couple with the geometry of the substrate to break the azimuthal symmetry. They also suggested that the

parallel and the perpendicular orientations may involve different out-of-plane bending constants, leading to different free energies. However, the curvature does not influence the lattice constant of either the parallel or perpendicular configurations. These results are consistent with the results we obtain, in which the lateral distance is the same in either orientations. They also observed that the topological defects were annihilated and the diblock copolymers become perpendicularly oriented with regard to the substrate after thermally annealing long enough, and this orientation is a stable state.

One important issue to be considered from a technological perspective is whether the dewetting can be prevented while the geometric constraint can keep sufficient strength as a guiding field to form ordered patterns. This motivated us to examine the stability of the thin films by analyzing the behavior of the free energy per area when varying the curvature.

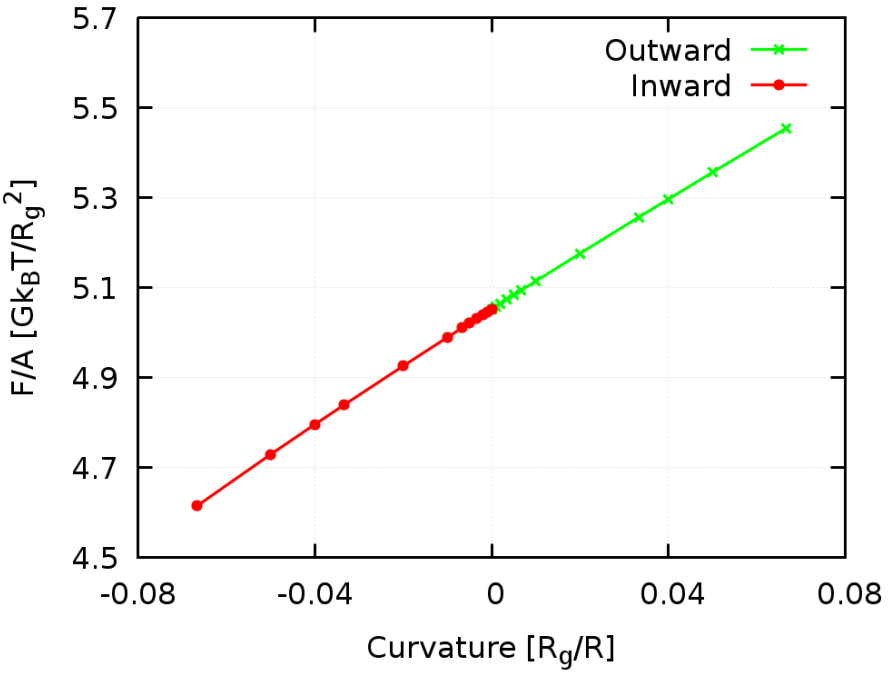

Figure 6.24: Free energy per area as a function of the curvature for the perpendicular configuration $C_\perp$ in the thin films, where the free surface attracts the A-block stronger than the substrate. The interaction parameters are $\Lambda_A^s N = -50$, $\Lambda_A^a N = -100$ and $\Lambda_B^{s,a} N = -30$.

Figures 6.24 and 6.25 show the behavior of the free energy as a function of the mean curvature for the perpendicular configurations $C_\perp$ in the two cases of asymmetric surfaces. For the outward films, for which the mean curvature $H \geqslant 0$, the free energy increases as the curvature increases. This indicates that the thin films are likely to become unstable and dewet from the substrate. It is also in good agreement with the experimental data shown in the figure 6.22, where at the crest of the substrate the thin films dewet. Conversely, for the inward films, for which the mean curvature is negative $H < 0$, the free energy decreases as the curvature increases. It suggests that the films remain

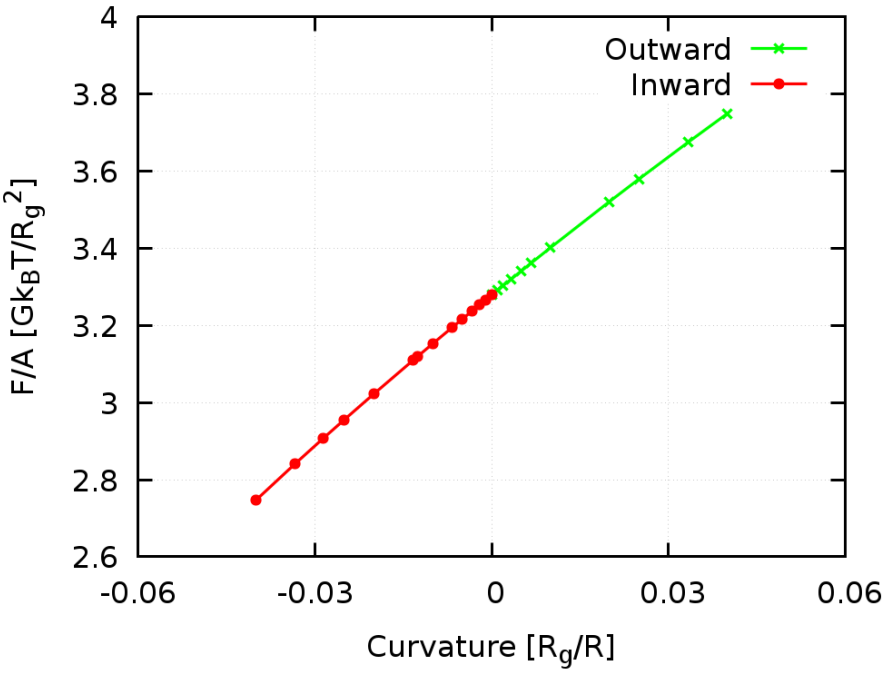

Figure 6.25: Free energy per area as a function of the curvature for the perpendicular configuration $C_\perp$ in the thin films, where the substrate attracts the A-block stronger than the free surface. The interaction parameters are $\Lambda_A^s N = -120$, $\Lambda_A^a N = -50$ and $\Lambda_B^{s,a} N = -30$.

stable. In the experiments (figure 6.22), it can be observed that the thin films dewet at the region with the highest curvature, where $H_{max} R_g \sim 0.015$ [81]. These results are in excellent agreement with our SCFT calculations discussed above. Furthermore, in the recent experiments on curved substrates, Park and Tsarkova [114] studied PS-b-PB diblock copolymer films confined in a corrugated substrate. They investigated the structure development of the thin films. They also reported that the thin films dewet at the crest region corresponding to the films with positive mean curvature $H > 0$ in our study.

Another important feature of diblock copolymers in the curved supported thin films is the film thickness. We present the behavior of the thickness as a function of the curvature for the perpendicular configuration in the films in figure 6.26 where the free surface attracts the A-block stronger that the substrate, and in figure 6.27 where the substrate attracts the A-block stronger than the free surface. It is observed that the films become thinner as the curvature increases for the outward films, whose the mean curvature is positive $H > 0$. On the contrary, the films thicken as the curvature increases for the inward films, whose mean curvature is negative $H < 0$. Our results are in a good agreement with experimental results of Park and Tsarkova [114]. They also found that the films thicken for $H < 0$ due to the flow of the diblock copolymer melt into the region with negative curvature during thermally annealing, where they called the grooves. This behavior does not depend on the initial thickness as well.

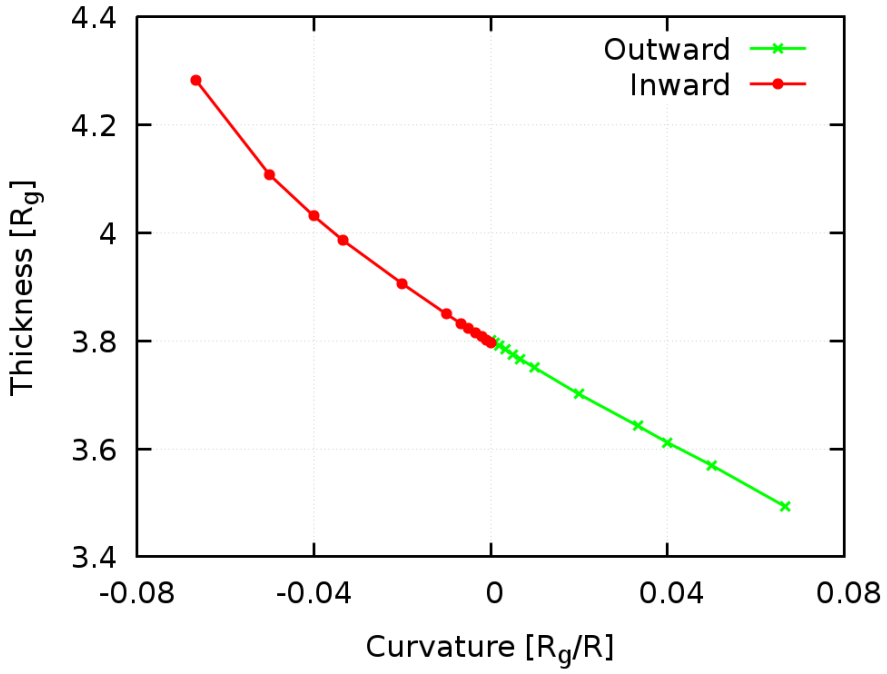

Figure 6.26: The minimum-energy thickness as a function of the curvature for the perpendicular configuration $C_\perp$ in the thin films, where the free surface attracts the A-block stronger than the substrate. The interaction parameters are $\Lambda_A^s N = -50$, $\Lambda_A^a N = -100$ and $\Lambda_B^{s,a} N = -30$.

6.6 CONCLUSIONS

In conclusion, we have shown that the confined geometry plays a fundamental role in the structure formation of diblock copolymer films through symmetry considerations, SCFT calculations and comparing with experimental results from our collaboration group. In particular, the curvature can be employed as a guiding field to produce well-ordered patterns. The SCFT calculations provide a rough estimate of the equilibrium configuration and the bending constant for curved systems. We find that the perpendicular configuration $C_\perp$ is always energetically favorable over the parallel configuration $C_{||}$ in the free-standing membranes. This is due to the anisotropic elasticity of the diblock copolymer phase on curved substrate. More interestingly, the behavior is different in the curved supported thin films. In the latter systems, the perpendicular configuration is still more stable at high curvatures; however, at the small curvature regime the parallel configuration becomes more stable. This switch of preferred configuration causes the appearence of topological defects in that region. We also use SCFT to investigate the free energy of the tilted configurations in which the angle between the director of the cylinder and the direction of the largest curvature is $\theta \in (0 : \pi/2)$. This gives us the evidence that both configurations, $C_\perp$ and $C_{||}$, represent local free energy minima with respect to the θ-configuration as described in the formula of F_{ani}. Furthermore, our study predicts dewetting in the regions with high local positive

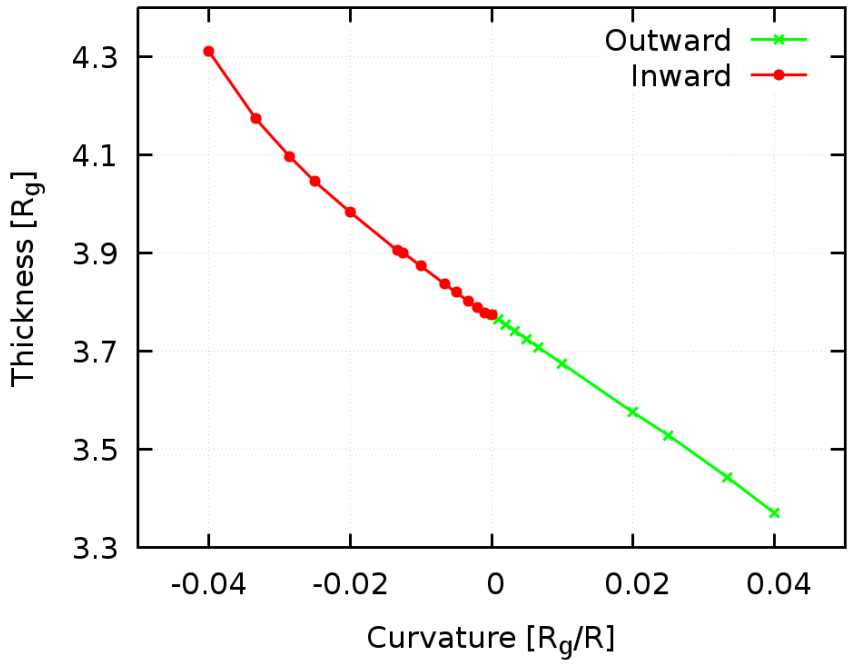

Figure 6.27: The minimum-energy thickness as a function of the curvature for the perpendicular configuration $C_\perp$ in the thin films, where the substrate attracts the A-block stronger than the free surface. The interaction parameters are $\Lambda_A^s N = -120$, $\Lambda_A^a N = -50$ and $\Lambda_B^{s,a} N = -30$.

mean curvature $H > 0$. From a technological perspective, our results suggest up a novel strategy for directing the self-assembly of thin layer of block copolymers with a desired structure through an appropriate control over the geometric properties and surface interactions. It should be possible to prevent dewetting while keeping a geometric field with sufficient strength to guide the order of the patterns.

7

CONCLUSION AND PERSPECTIVE

In this thesis, we have applied self-consistent field theory (SCFT) to different thin film systems to explore the self-assembly of diblock copolymers. In chapter 4, we analyzed the stability of the multiple layers of cylinder-forming of diblock copolymers confined between two flat surfaces. The SCFT was employed to determine the optimum thickness of the films. The calculations were performed in the grand canonical essemble to let the number of copolymers adjust to the film thickness. We minimized the free energy with respect to the film thickness and the characteristic wave length. Thus we determined the optimum thickness and the lateral spacing distance of each number of layers of cylinders in thin films. The results indicate the important role of the film thickness in the morphologies of diblock copolymers. The global equilibrium state of the thin films is the one where the monolayer of cylinders coexists with the islands of thick multilayer films. Furthermore, we analyzed the coupling mechanism between the bottom and the upper layers as well. The addition of the second layer slightly changed the structure of the first layer, and this interaction provides a mechanism on how the aligned first layer helps to order the second layer. This mechanism offers a possible way to propagate the order in thick block copolymer films and to control the orientation of the nanostructures [80]. Indeed, our experimental partners (Vega et al.) find that the coupling mechanism drives the complete annihilation of topological defects, disclinations, and improve global orientation of thin films during the annealing process. The SCFT results are in excellent agreement with the experimental data obtained by Professor Vega's group [80].

Furthermore, we also studied the orientational phase transition from the $C_{||}$ monolayer of parallel cylinder to the $C_{\perp}$ perpendicular cylinder configurations in chapter 5. Such a phase transition is controlled by the surface field and the mismatch between the natural size of monolayer of cylinders and the film thickness. We obtain this phase transition, $C_{||} \rightarrow C_{\perp}$, as the thickness reduces below the periodicity of monolayer in the thin films with symmetric surface interactions. The thin films become unstable when the films are very thin. This is a result of increase in the free energy per area with decrease in the film thickness. The SCFT results are qualitatively consistent but not exactly quantitative with the experimental data obtained by Abate et al.[78]. In addition to the symmetric surfaces, we also studied the case in which the strength of preferential attraction of each surface to block copolymers are asymmetric. Depending on the surface interactions and the thin film thickness, the lamellar phase (L) and perforated lamellar phase (PL) can be found at equilibrium. These phases appear when the film thickness is about half the natural size of the monolayer of cylinders. The globally stable state of the films can change from the $C_{||}$ to PL or L, depending on the degree of asymmetry between the two surfaces. Our results indicate that both the film thickness and the surface

fields can either orient the structures or stabilize the deviation structure from the bulk, such as PL and L.

Finally in chapter 6, we extended the method to the block copolymers confined between the two curved substrates (the two coaxial cylindrical surfaces). We consider two types of model systems: the free-standing block copolymer membranes and the block copolymer thin films deposited onto curved supported substrates. First, we derived a general expression for the elastic energy of anisotropic nematic membranes. Then we employed SCFT to examine the elastic properties of the free-standing membranes and curved supported thin films. We fitted the SCFT free energy up to a quadratic order on the mean curvature to extract the bending constant of the free-standing membranes. Thus we can establish a relationship between the morphologies of block copolymer membranes, the thin film and its shape, i.e., its local cuvature. We find that there is a strong coupling between the local orientation of the block copolymer patterns and the geometry of substrates. Specifically, the $C_{\perp}$ perpendicular configuration is always stable in the free-standing membranes. However in the curved supported thin films, the $C_{\perp}$ is only stable at the high curvatures and the $C_{||}$ is stable at the small curvatures. As a result, there is a transition from the perpendicular to parallel orientation in supported thin films at small curvatures that is absent in the free-standing membranes. The results indicate that the curvature acts as a guiding field for the patterns in thin films. Therefore, the use of geometry of patterned substrates is a proposed solution to align block copolymer patterns and as a consequence to enforce the long range order [81]. Moreover, we also found that the thin films with positive mean curvature likely become unstable and dewet from the substrate at high curvatures, while the films with negative mean curvature thicken with the curvature. These results are in good agreement with experiments [81, 114].

This thesis focuses on the diblock copolymers. We can apply our simulations to predict the phase behaviour of ABA triblock copolymers or other architectures, which remain largely unexplored. These copolymers have potential applications because of their architecture. For example, the triblock copolymers are found to provide improved mechanical properties relative to diblock copolymers. It is due to the triblock architecture, which allows the chain bridging between discrete A-block domains [115, 116].

All the SCF calculations in this thesis were carried out in Euclidean geometry with periodic boundary conditions. We can extend the method to non-Euclidean geometries. Such geometries present a considerable challenge, such as how to deal with an unit cell and boundary conditions. For example, if we have a hexagonal array of cylinders perpendicularly oriented with regard to the spherical surface, we need use some non-trivial periodic boundaries. Obviously, we can solve the problem on the whole sphere [117]; however, it is expensive. The study in non-Euclidean geometry is interesting and provides us a new strategy using the geometry to produce well-ordered nanostructures of the patterns.

Furthermore, the kinetics of phase evolution is essential for understanding the pattern formation processes in structured fluid copolymers. For example,

it provides a description of the phase transitions, the development and annihilation of defects during the phase transition between the different phases. We only investigated the static phase behavior of diblock copolymers in this thesis, we can simulate the dynamical evolution of the diblock copolymer films by means of Dynamic Density Functional Theory, or dynamical self-consistent field theory (DSCFT) methods [118].

Part III

APPENDIX

A

SHIFTED FREE ENERGY

We present here the shift of free energy ΔF as a function of the discretization Δz for different strengths of surface interaction in the curved supported thin films, which were studied in chapter 6.

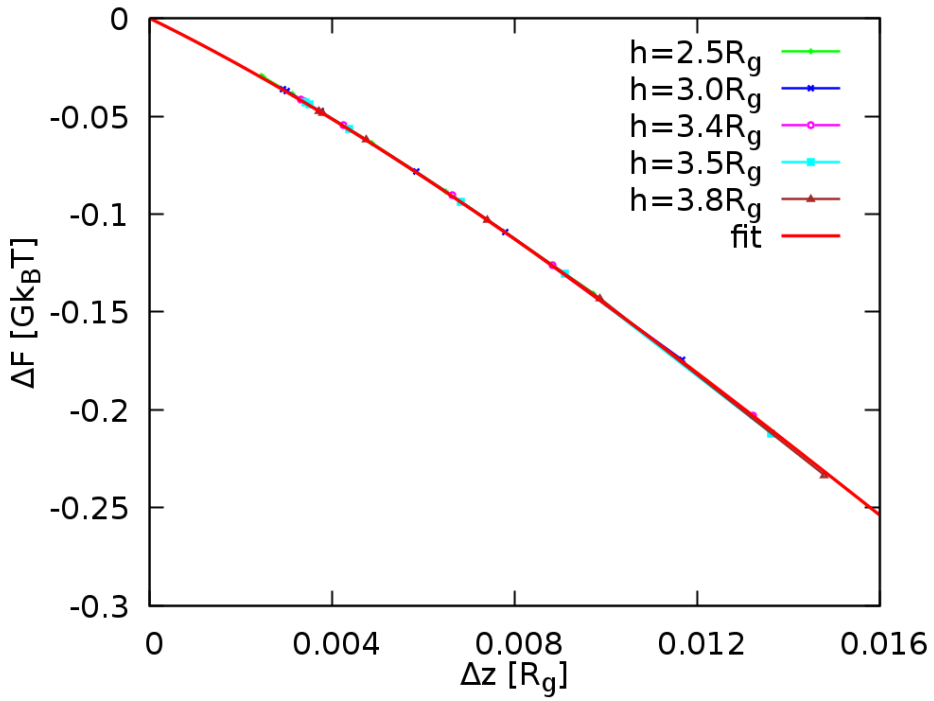

Figure A.1: Shifted energy ΔF as a function of discretization Δz for different film thicknesses h with surface interactions $\Lambda_A N = -125$, $\Lambda_B N = -120$ at one surface and $\Lambda_A N = -115$, $\Lambda_B N = -110$ at the other surface. The chemical potential $\mu = (2.5 + \ln G) k_B T$. The solid line corresponds to the fit function $\Delta F(\Delta z) = -12.68\,\Delta z - 269\,\Delta z^2 - 2788\,\Delta z^3$.

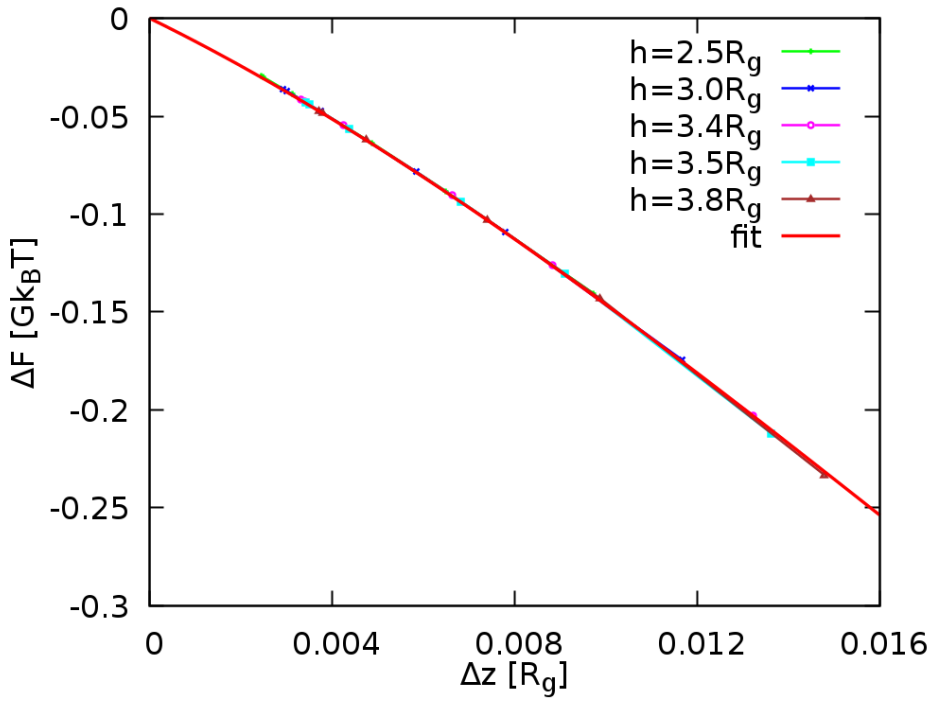

Figure A.2: Shifted energy ΔF as a function of discretization Δz for different film thicknesses h with surface interactions $\Lambda_A N = -120$, $\Lambda_B N = -115$ at one surface and $\Lambda_A N = -100$, $\Lambda_B N = -95$ at the other surface. The chemical potential $\mu = (2.5 + \ln G) k_B T$. The solid line corresponds to the fit function $\Delta F(\Delta z) = -11.41\,\Delta z - 395\,\Delta z^2 + 7304\,\Delta z^3$.

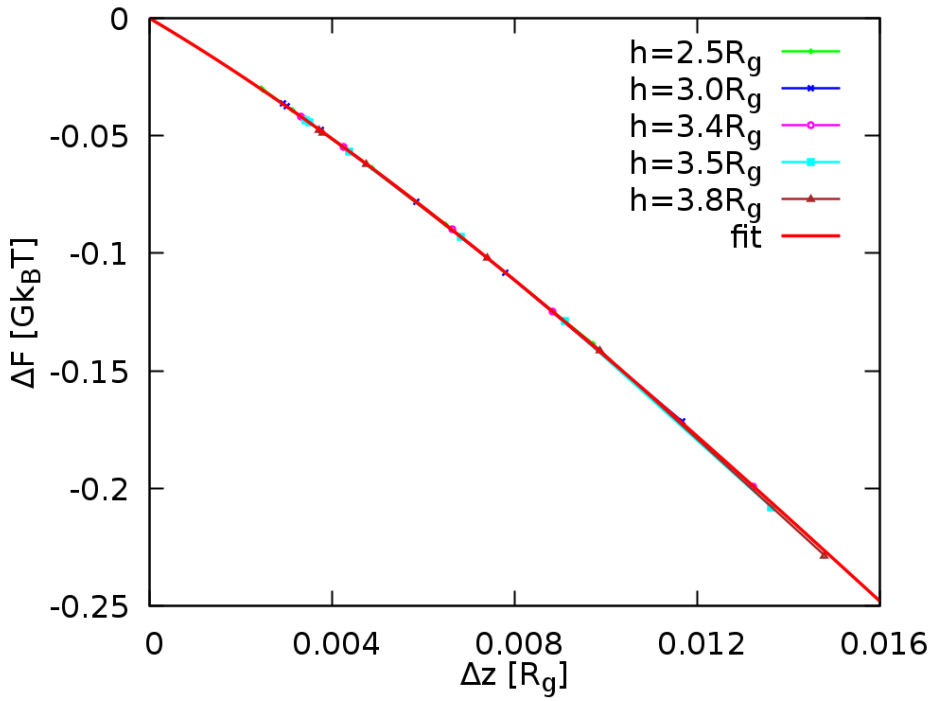

Figure A.3: Shifted energy ΔF as a function of discretization Δz for different film thicknesses h with surface interactions $\Lambda_A N = -120$, $\Lambda_B N = -115$ at one surface and $\Lambda_A N = -90$, $\Lambda_B N = -85$ at the other surface. The chemical potential $\mu = (2.5 + \ln G) k_B T$. The solid line corresponds to the fit function $\Delta F(\Delta z) = -11.5\,\Delta z - 358\,\Delta z^2 + 6740\,\Delta z^3$.

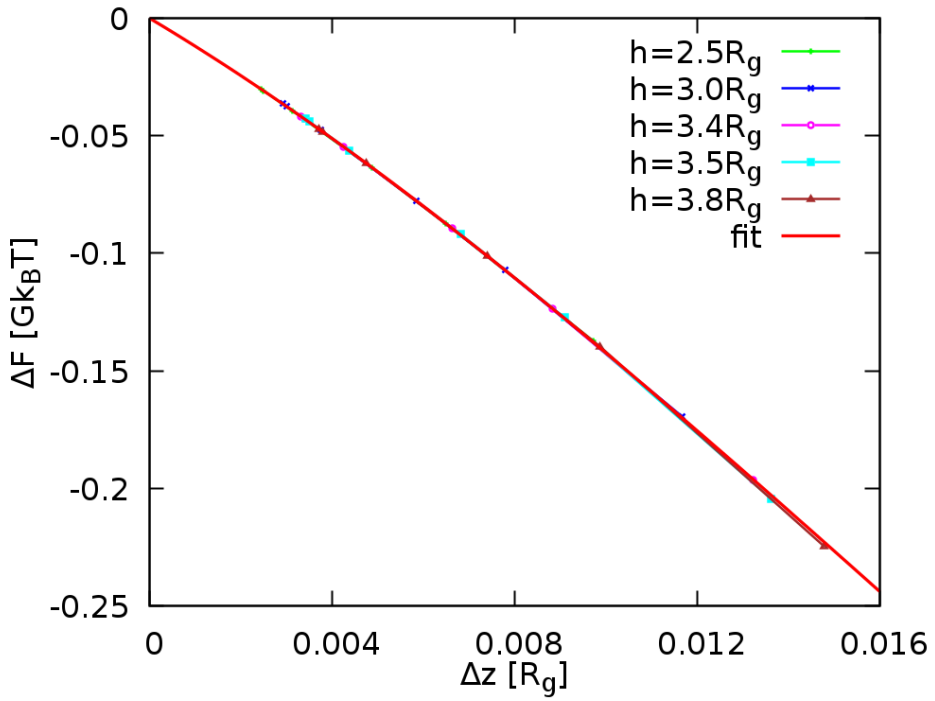

Figure A.4: Shifted energy ΔF as a function of discretization Δz for different film thicknesses h with surface interactions $\Lambda_A N = -120$, $\Lambda_B N = -115$ at one surface and $\Lambda_A N = -80$, $\Lambda_B N = -75$ at the other surface. The chemical potential $\mu = (2.5 + \ln G) k_B T$. The solid line corresponds to the fit function $\Delta F(\Delta z) = -11.57\,\Delta z - 330\,\Delta z^2 + 6255\,\Delta z^3$.

B

EFFECTIVE SELF-CONSISTENT FIELD THEORY FOR THIN FILMS

We develop an effective self-consistent field theory for two dimensional thin films. By applying some approximations, we separate the two dimensional problem into two one dimensional problems.

B.1 THIN FILM IN TWO DIMENSIONS (X,Y)

We consider AB diblock copolymers in thin films as described in chapter 2. The main task is finding the solutions of the modified diffusion equation:

$$\frac{\partial q(x,y,s)}{\partial s} = \nabla^2 q(x,y,s) - \omega_\alpha(x,y) q(x,y,s) \tag{B.1}$$

Here, α can be the A or B block. In order to separate the variables, x and y, in the propagators, we make an ansatz:

$$\begin{aligned} q(x,y,s) &= q_x(x,s)\, q_y(y,s) && \text{(B.2)} \\ q^\dagger(x,y,s) &= q_x^\dagger(x,s)\, q_y^\dagger(y,s) && \text{(B.3)} \end{aligned}$$

and use the approximation that the system is homogeneous in $x-$direction and the total density $\phi(x,y)$ can be separated

$$\begin{aligned} m(x,y) &= \phi_A(x,y) - \phi_B(x,y) \approx \bar{m}(y) && \text{(B.4)} \\ \phi(x,y) &= \phi_A(x,y) + \phi_B(x,y) \approx 1 + \bar{\phi}_1(x) + \bar{\phi}_2(y) && \text{(B.5)} \end{aligned}$$

with

$$\begin{aligned} \bar{m}(y) &= \frac{1}{L_x}\int dx\, m(x,y) && \text{(B.6)} \\ \bar{\phi}_1(x) &= \frac{1}{L_y}\int dy\ (-1+\phi(x,y)) \\ &= -1 + \frac{V}{L_y Q}\int dy \int_0^1 ds\, q(x,y,s)\, q^\dagger(x,y,1-s) \\ &= -1 + \frac{L_x}{Q_x}\int_0^1 ds\, q_x(x,s)\, q_x^\dagger(x,1-s) && \text{(B.7)} \\ \bar{\phi}_2(y) &= \frac{1}{L_x}\int dx\ (-1+\phi(x,y)) \\ &= -1 + \frac{V}{L_x Q}\int dx \int_0^1 ds\, q(x,y,s)\, q^\dagger(x,y,1-s) \\ &= -1 + \frac{L_y}{Q_y}\int_0^1 ds\, q_y(y,s)\, q_y^\dagger(y,1-s) && \text{(B.8)} \end{aligned}$$

Here, we assume that Q_x and Q_y are independent of s

$$Q_x = \int dx\, q_x(x,s)\, q_x^\dagger(x,1-s) \tag{B.9}$$

$$Q_y = \int dy\, q_y(y,s)\, q_y^\dagger(y,1-s) \tag{B.10}$$

Inserting equations (B.2) and (B.3) into the modified diffusion equations (equations 2.27), we get separated diffusion equations for x-, and y-direction. For the x-direction, we get:

$$\frac{\partial q_x(x,s)}{\partial s} = \frac{\partial^2 q_x(x,s)}{\partial x^2} - \omega_\alpha(x,s)\, q_x(x,s) \tag{B.11}$$

$$\frac{\partial q_x^\dagger(x,1-s)}{\partial s} = \frac{\partial^2 q_x^\dagger(x,1-s)}{\partial x^2} - \omega_\alpha(x,s) q_x^\dagger(x,1-s) \tag{B.12}$$

$$\omega_\alpha(x,s) = N\kappa\,\bar{\phi}_1(x) \tag{B.13}$$

For the y-direction, we get:

$$\frac{\partial q_y(y,s)}{\partial s} = \frac{\partial^2 q_y(y,s)}{\partial y^2} - \omega_\alpha(y,s)\, q_y(y,s) \tag{B.14}$$

$$\frac{\partial q_y^\dagger(y,1-s)}{\partial s} = \frac{\partial^2 q_y^\dagger(y,1-s)}{\partial y^2} - \omega_\alpha^\dagger(y,s)\, q_y^\dagger(y,1-s) \tag{B.15}$$

$$\omega_\alpha(y,s) = \begin{cases} \omega_A(y,s) = \frac{-N\chi}{2}\,\bar{m}(y) + N\kappa\,\bar{\phi}_2(y) & \text{for } 0 < s < f \\ \omega_B(y,s) = \frac{N\chi}{2}\,\bar{m}(y) + N\kappa\,\bar{\phi}_2(y) & \text{for } f < s < 1 \end{cases} \tag{B.16}$$

We solve the equations (B.11) and (B.12) in x-direction numerically and by the ground state dominance (GSD) approximation as well.
The propagator can be written as

$$q_x(x,s) = \sum_{k=0}^{\infty} q_k\, X_k(x)\, e^{-\lambda_k s} \tag{B.17}$$

where $q_k = \int dx\, X_k(x)$, $(k = 0, 1, 2, \cdots)$. The functions $X_k(x)$ are orthogonal, and satisfy the following equation

$$\int dx\, X_j(x)\, X_k(x) = \delta_{jk} \tag{B.18}$$

With the ground state approximation, the propagators become

$$q_x(x,s) \approx q_0\, X_0(x)\, e^{-\lambda_0 s} \tag{B.19}$$

$$q_x^\dagger(x,1-s) \approx q_0\, X_0(x)\, e^{-\lambda_0(1-s)} \tag{B.20}$$

λ_0 is the lowest energy of the system. We consider both canonical and grand canonical ensembles.

B.1.1 *Canonical ensemble*

Inserting the ground state approximation into the expression of $\bar{\phi}_{1(x)}$ in equation B.7, gives us:

$$\begin{aligned}\bar{\phi}_1(x) &= -1 + \frac{L_x}{Q_x}\int_0^1 ds\, q_x(x,s)\, q_x^\dagger(x,1-s) \\ &= -1 + \frac{L_x}{\int_0^{L_x} dx\, q_x(x,s)\, q_x^\dagger(x,1-s)}\int_0^1 ds\, q_x(x,s)\, q_x^\dagger(x,1-s) \\ &= -1 + a\, X_0^2(x) \end{aligned} \tag{B.21}$$

where $a^{-1} = \frac{1}{L_x}\int_0^{L_x} dx\, X_0^2(x)$ $(a \geqslant 1)$. Then by substituting this result into equation B.13, we obtain the field as:

$$\omega_\alpha(x,s) = N\,\kappa(-1 + a\, X_0^2(x)) \tag{B.22}$$

Finally, the modified diffusion equation takes the form:

$$X_0''(x) - N\,\kappa(-1 + a\, X_0^2(x))\, X_0(x) = -\lambda_0\, X_0(x) \tag{B.23}$$

We can choose $\lambda_0 = 0$, then eq. (B.23) becomes:

$$X_0''(x) - N\,\kappa\, a\, X_0^3(x) + N\,\kappa X_0(x) = 0 \tag{B.24}$$

We define:

$$U(X_0) = -\frac{N\,\kappa\, a}{4}X_0^4 + \frac{N\,\kappa}{2}X_0^2 \tag{B.25}$$

Then:

$$\frac{1}{2}X_0'^2(x) + U(X_0) = C \tag{B.26}$$

where C is a constant and $X_0(x)$ satisfies the following boundary conditions:

$$\begin{aligned} X_0'(L_x/2) &= 0 \\ X_0(L_x/2) &= X_0^{max}, \quad X_0^{max} \in [0, \sqrt{a^{-1}}] \\ X_0(0) &= X_0(L_x) = 0 \end{aligned} \tag{B.27}$$

Using these conditions, we find the expression for constant C in equation B.26

$$U(X_0^{max}) = -\frac{N\,\kappa\, a}{4}(X_0^{max})^4 + \frac{N\,\kappa}{2}(X_0^{max})^2 \tag{B.28}$$

$$\implies C = U(X_0^{max}) = -\frac{N\,\kappa\, a}{4}(X_0^{max})^4 + \frac{N\,\kappa}{2}(X_0^{max})^2 \tag{B.29}$$

We solve equation (B.26) by Mathematica. Here, we choose $a = 1$ without loss of generality.
The following figures show the comparision of the results obtained from the numerical and ground state dominance methods. They match quite well.

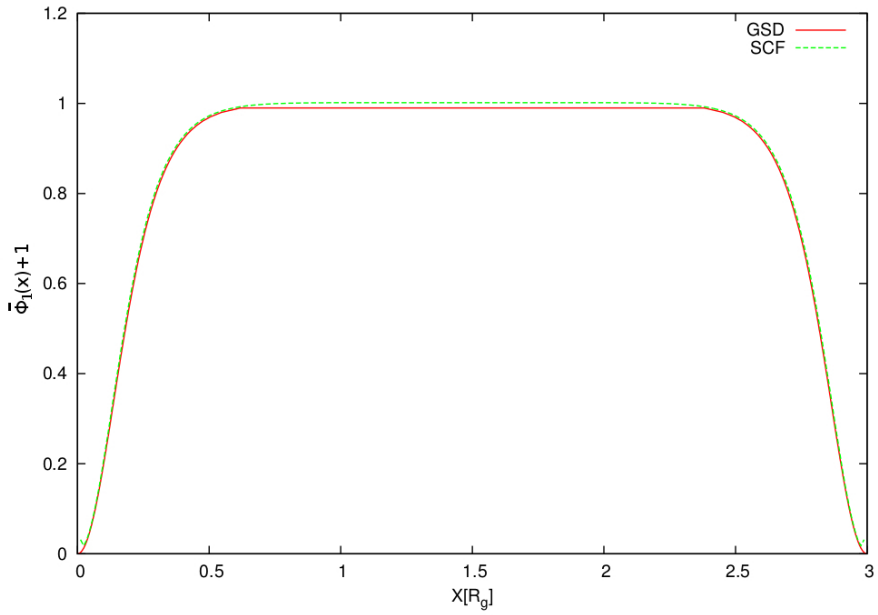

A

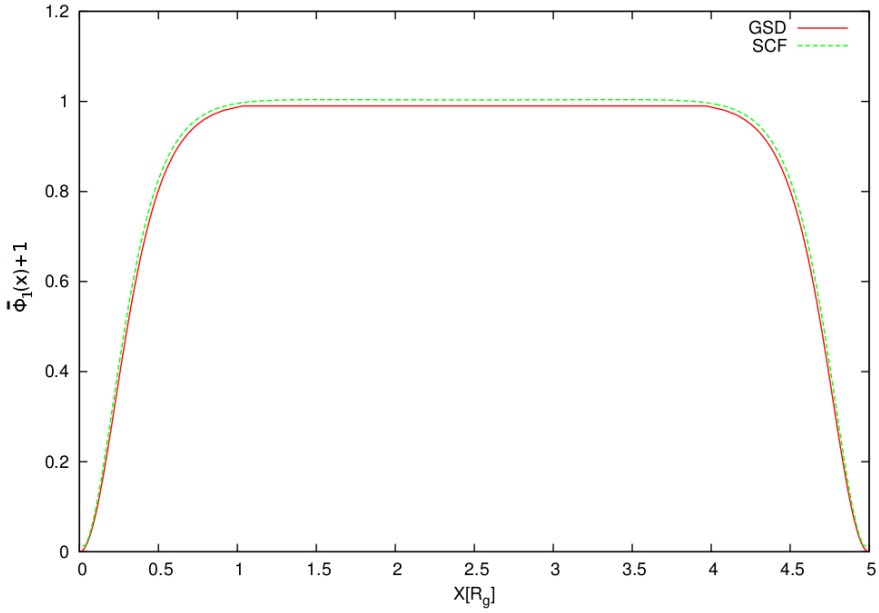

B

Figure B.1: Canonical ensemble with $N = 32$. $(\bar{\phi}_1(x) + 1)$ as a function of X-the thin film length in x−direction in units of the unperturbed radius gyration R_g ($\bar{\phi}_1(x)$ defined in eq. (B.7) for SCF and in eq. (B.21) for GSD). The thin film length in A) $L_x = 3$ and B) $L_x = 5$.

B.1.2 *Grand canonical ensemble*

We proceed the same way as above.

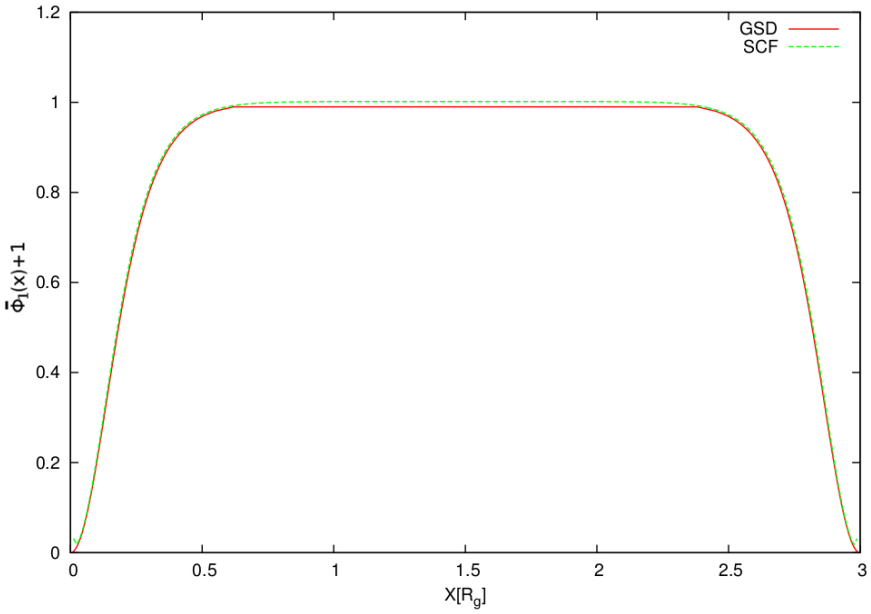

A

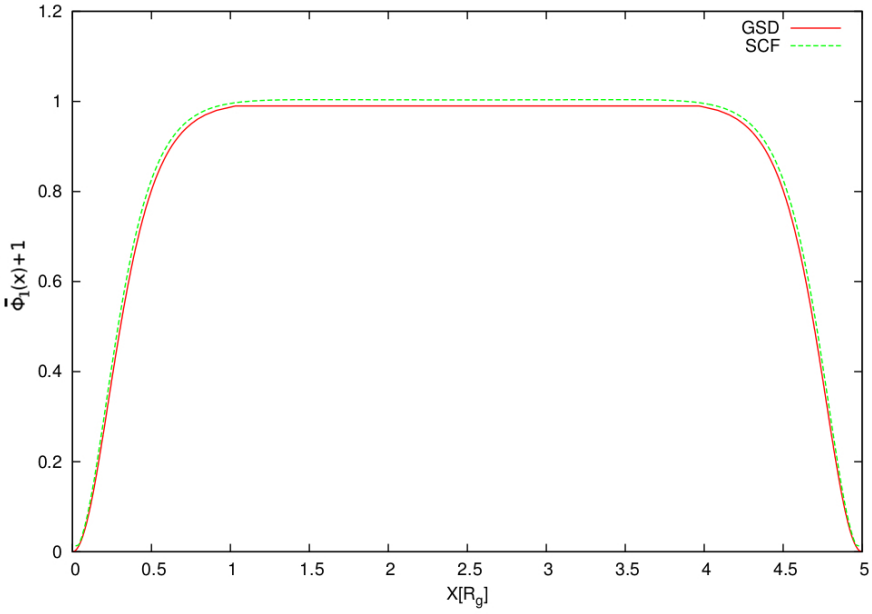

B

Figure B.2: Canonical ensemble with $N = 64$. $(\bar{\phi}_1(x) + 1)$ as a function of X-the thin film length in x−direction in units of the unperturbed radius gyration R_g ($\bar{\phi}_1(x)$ defined in eq. (B.7) for SCF and in eq. (B.21) for GSD). The thin film length in A) $L_x = 3$ and B) $L_x = 5$.

$$\begin{aligned}
\bar{\phi}_1(x) &= \frac{1}{L_y}\int dy[-1+\phi(x,y)] \\
&= -1+\frac{zN}{\phi_0 L_y}\int dy \int_0^1 ds\, q_x(x,s)\, q_x^\dagger(x,1-s)\, q_y(y,s)\, q_y^\dagger(y,1-s) \\
&= -1+\frac{zNQ_y}{\phi_0 L_y}\int_0^1 ds\, q_x(x,s)\, q_x^\dagger(x,1-s) \\
&= -1+z_1'\int_0^1 ds\, q_x(x,s)\, q_x^\dagger(x,1-s) \qquad \text{(B.30)}
\end{aligned}$$

where we denote

$$Q_y = \int dy\, q_y(y,s)\, q_y^\dagger(y,1-s) \tag{B.31}$$

$$z_1' = \frac{z N Q_y}{\phi_0 L_y} \tag{B.32}$$

$$\begin{aligned}\bar{\phi}_2(y) &= \frac{1}{L_x}\int dx\, [-1+\phi(x,y)] \\ &= -1 + z_2' \int_0^1 ds\, q_y(y,s)\, q_y^\dagger(y,1-s) \qquad \text{(B.33)} \\ Q_x &= \int dx\, q_x(x,s)\, q_x^\dagger(x,1-s), \quad z_2' = \frac{z N Q_x}{\phi_0 L_x} \qquad \text{(B.34)}\end{aligned}$$

For x-direction

$$\frac{\partial q_x(x,s)}{\partial s} = \frac{\partial^2 q_x(x,s)}{\partial x^2} - N\kappa\, \bar{\phi}_1(x)\, q_x(x,s) \tag{B.35}$$

Using ground state dominance $q_x(x,s) \approx q_0\, X_0(x)\, e^{-\lambda_0 s}$ (choose $\lambda_0 = 0$), we obtain:

$$\begin{aligned}\bar{\phi}_1(x) &= -1 + z_1' \int_0^1 ds\, q_x(x,s)\, q_x^\dagger(x,1-s) \\ &= -1 + z_1'\, q_0^2\, X_0^2(x) \qquad \text{(B.36)}\end{aligned}$$

$$X_0''(x) - N\kappa(-1 + z_1'\, q_0^2\, X_0^2(x))\, X_0(x) = 0 \tag{B.37}$$

$$X_0''(x) - N\kappa z_1' q_0^2\, X_0^3(x) + N\kappa X_0(x) = 0 \tag{B.38}$$

where $q_0 = \int_0^{L_x} dx\, X_0(x)$, and we choose $z_1' = 1$ (the same in numerical calculation).
We define:

$$U(X_0) = -\frac{N\kappa\, q_0^2}{4} X_0^4 + \frac{N\kappa}{2} X_0^2 \tag{B.39}$$

Then:

$$\frac{1}{2} X_0'^2(x) + U(X_0) = \text{const} \tag{B.40}$$

where $X_0(x)$ satisfies the following conditions:

$$\begin{aligned}X_0'(L_x/2) &= 0 \\ X_0(L_x/2) &= X_0^{max}, \quad X_0^{max} \in \left[0, \sqrt{\frac{1}{q_0^2}}\right] \\ X_0(0) &= X_0(L_x) = 0 \qquad \text{(B.41)}\end{aligned}$$

Without losing generality, we here chose $q_0^2 = 1$

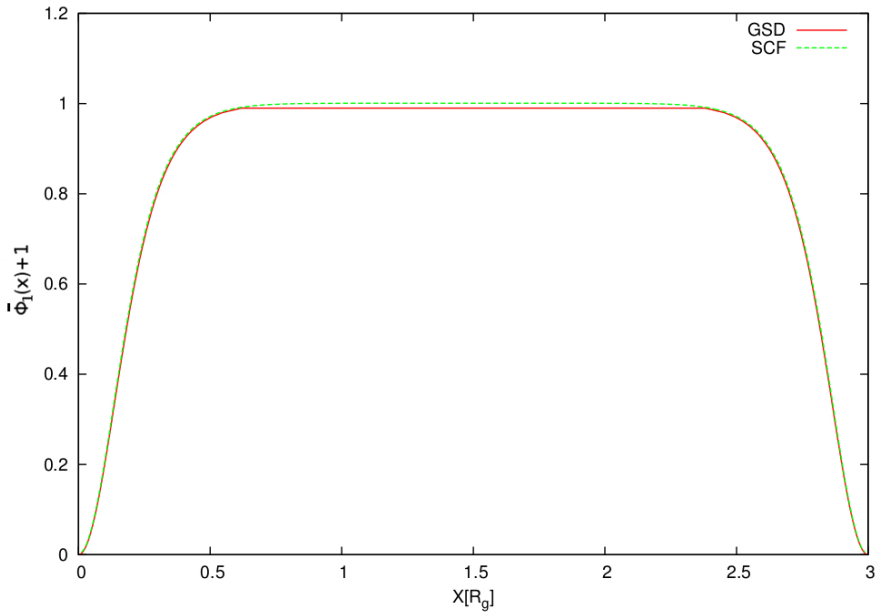

A

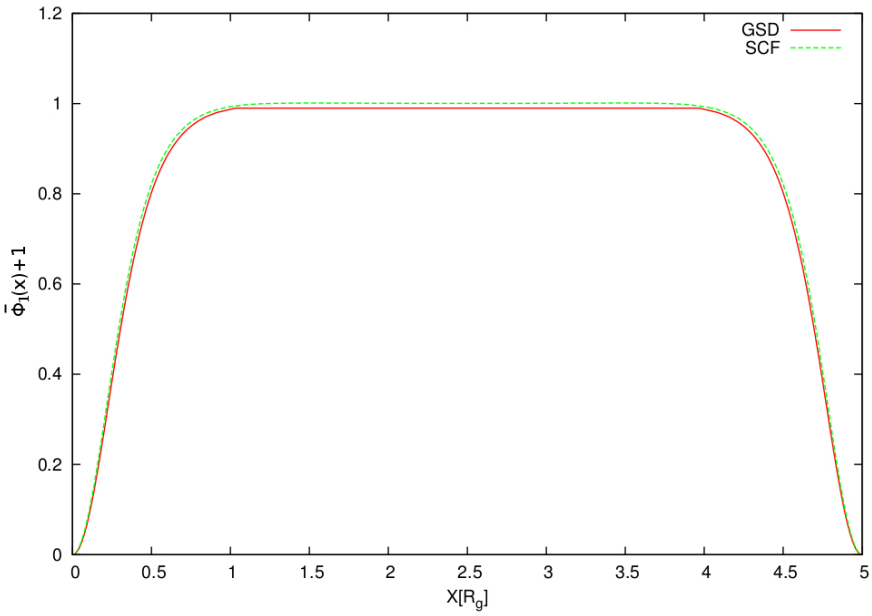

B

Figure B.3: Grand canonical ensemble with $N = 32$. $(\bar{\phi}_1(x) + 1)$ as a function of X-the thin film length in x−direction in units of the unperturbed radius gyration R_g. $(\bar{\phi}_1(x)$ defined in eq. (B.30) for SCF and in eq. (B.36) for GSD). The thin film length in A) $L_x = 3$ and B) $L_x = 5$.

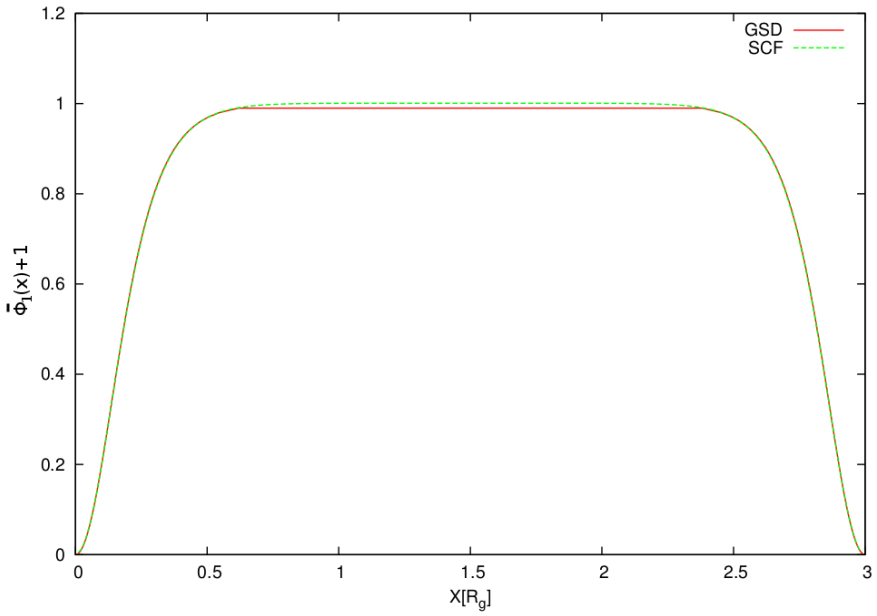

A

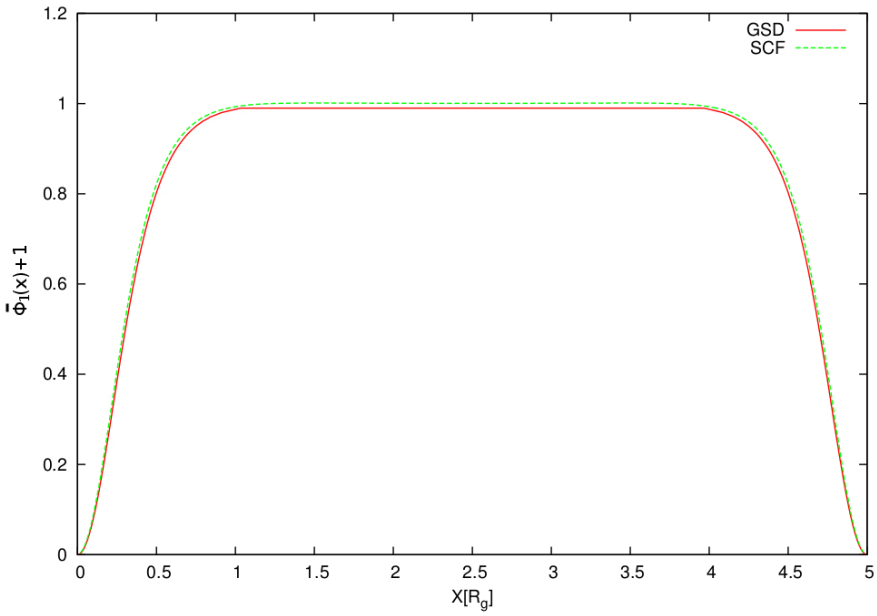

B

Figure B.4: Grand canonical ensemble with $N = 64$. $(\bar{\phi}_1(x) + 1)$ as a function of X-the thin film length in x−direction in units of the unperturbed radius gyration R_g. $(\bar{\phi}_1(x)$ defined in eq. (B.30) for SCF and in eq. (B.36) for GSD). The thin film length in A) $L_x = 3$ and B) $L_x = 5$.

BIBLIOGRAPHY

[1] L. A. Tsarkova, G. J. A. Sevink and G. Krausch. 'Nanopattern evolution in block copolymer films: experiment, simulation and challenges'. In: *Adv. Polym. Sci.* 27 (2010), pp. 33–73.

[2] Y. S. Jung and C. A. Ross. 'Orientation-controlled self-assembled nanolithography using a polystyrene-polydimethylsiloxane block copolymer'. In: *Nano Letters* 7 (2007), pp. 2046–2050.

[3] J. N. L. Albert and T. H. Epps. 'Self-assembly of block copolymer thin films'. In: *Materials Today* 6 (2010), pp. 24–33.

[4] S. Park, L. Tsarkova, S. Hiltl, S. Roitsch, J. Mayer and A. Böker. 'Guiding block copolymers into sequenced patterns via inverted terrace formation'. In: *Macromolecules* 45 (2012), pp. 2494–2501.

[5] F. S. Bates, M. A. Hillmyer, T. P. Lodge, C. M. Bates, K. T. Delaney and G. H. Fredrickson. 'Multiblock polymers: Panacea or pandora's box'. In: *Science* 336 (2012), pp. 434–440.

[6] A. P. Marencic and R. A. Register. 'Controlling order in block copolymer thin films for nanopatterning applications'. In: *Annu. Rev. Chem. Bimol. Eng.* 1 (2010), pp. 277–297.

[7] I. W. Hamley. 'Nanostructure fabrication using block copolymers'. In: *Nanotechnology* 14 (2003), R39–R54.

[8] A-V Ruzzette and L. Leibler. 'Block copolymers in tomorrow's plastics'. In: *Nature Materials* 4 (2005), pp. 19–31.

[9] S. B. Darling. 'Directing the self-assembly of block copolymers'. In: *Prog. Polym. Sci.* 32 (2007), pp. 1152–1204.

[10] P.-G. de Gennes. *Scaling Concepts in Polymer Physics*. Cornell University Press, Ithaca and London, 1979.

[11] M. Park, C. Harrison, P. M. Chaikin, R. A. Register and D. H. Adamson. 'Block copolymer lithography: Periodic arrays of $\sim 10^{11}$ holes in 1 square centimeter'. In: *Science* 276 (1997), pp. 1401–1404.

[12] R. A. Segalman. 'Patterning with block copolymer thin films'. In: *Mater. Sci. Eng., R* 48 (2005), pp. 191–226.

[13] K. Shin, K. A. Leach, J. T. Goldbach, D. H. Kim, J. Y. Jho, M. Touminen, C. J. Hawker and T. P. Russell. 'A simple route to metal nanodots and nanoporous metal films'. In: *Nano Letters* 2 (2002), pp. 933–936.

[14] V. Pelletier, K. Asakawa, M. Wu, D. H. Adamson, R. A. Register and P. M. Chaikin. 'Aluminum nanowire polarizing grids: Fabrication and analysis'. In: *Appl. Phys. Lett* 88 (2006), p. 211114.

[15] Y.-R. Hong, K. Asakawa, D. H. Adamson, P. M. Chaikin and R. M. Register. 'Silicon nanowire grid polarizer for very deep ultraviolet fabricated from a shear-aligned diblock copolymer template'. In: *Opt. Lett.* 32 (2007), pp. 3125–3127.

[16] J. Y. Cheng, C. A. Ross, V. Z. H. Chan, E. L. Thomas, R. G. H. Lammertink and G. J. Vancso. 'Formation of a cobalt magnetic dot array via block copolymer lithography'. In: *Adv. Mater.* 13 (2001), pp. 1174–1178.

[17] B. J. Kim, G. H. Fredrickson and E. J. Kramer. 'Effect of polymer ligand molecular weight on polymer-coated nanoparticle location in block copolymer'. In: *Macromolecules* 41 (2008), pp. 436–447.

[18] M. Müller, K. Katsov and M. Schick. 'New mechanism of membrane fusion'. In: *J. Chem. Phys.* 116 (2002), pp. 2342–2345.

[19] G. Liu and J. Zhao. 'Guided alignment and positioning of single DNA molecules by a structured contact line on a block copolymer surface'. In: *Langmuir* 22 (2006), pp. 2923–2926.

[20] G. H. Fredrickson. *The Equilibrium Theory of Inhomogeneous Polymers*. Oxford University Press, New York, 2006.

[21] M. W. Matsen and F. S. Bates. 'Origins of complex self-assembly in block copolymers'. In: *Macromolecules* 29 (1996), pp. 7641–7644.

[22] F. Schmid. 'Self-consistent-field theories for complex fluids'. In: *J. Phys.: Condens. Matter* 10 (1998), pp. 8105–8138.

[23] G. H. Fredrickson, V. Ganesan and F. Drolet. 'Field-theoretic computer simulation methods for polymers and complex fluids'. In: *Macromolecules* 35 (2002), pp. 16–39.

[24] M. W. Matsen. 'Effect of architecture on the phase behavior of AB-type block copolymer melts'. In: *Macromolecules* 45 (2012), pp. 2161–2165.

[25] F. S. Bates, M. F. Schulz, A. K. Khandpur, S. Förster, K. Rosedale J. H.and Almdal and K. Mortensen. 'Fluctuations, Conformational asymmetry and block copolymer phase behaviour'. In: *Faraday Discuss* 98 (1994), pp. 7–18.

[26] M. I. Kim, T. Wakada, S. Akasaka, S. Nishitsuji, K. Saijo, H. Hasegawa, K. Ito and M. Takenaka. 'Stability of the Fddd phase in diblock copolymer melts'. In: *Macromolecules* 41 (2008), pp. 7667–7670.

[27] M. I. Kim, T. Wakada, S. Akasaka, S. Nishitsuji, K. Saijo, H. Hasegawa, K. Ito and M. Takenaka. 'Determination of the Fddd phase boundary in plostyrene-block-polyisoprene diblock copolymer melts'. In: *Macromolecules* 42 (2009), pp. 5266–5271.

[28] M. W. Matsen. 'The standard Gaussian model for block copolymer melts'. In: *J. Phys.: Condens. Matter* 14 (2002), R21–R47.

[29] J. Y. Cheng, C. A. Ross, E. L. Thomas, H. I. Smith and G. J. Vancso. 'Templated self-assembly of block copolymers: Effect of substrate topography'. In: *Adv. Mater.* 15 (2003), pp. 1599–1602.

[30] S. O. Kim, H. H. Solak, M. P. Stoykovich, N. J. Ferrier, J. J. de Pablo and P. F. Nealey. 'Epitaxial self-assembly of block copolymers on lithographically defined nanopatterned substrates'. In: *Nature* 424 (2003), pp. 411–414.

[31] F. S. Bates and G. H. Fredrickson. 'Block copolymer-designer soft materials'. In: *Physics Today* 52 (1999), pp. 32–38.

[32] A. Knoll, A. Horvat, K. S. Lyakhova, G. Krausch, G. J. A. Sevink, A. V. Zvelindovsky and R. Magerle. 'Phase behavior in thin film of cylinder-forming block copolymers'. In: *Phys. Rev. Lett.* 89 (2002), pp. 0355011–0355014.

[33] A. Knoll and R. Magerle. 'Phase behavior in thin films of cylinder-forming ABA block copolymers: Experiments'. In: *J. Chem. Phys.* 120 (2004), pp. 1105–1116.

[34] A. Horvat, K. S. Lyakhova, G. J. A. Sevink, A. V. Zvelindovsky and R. Magerle. 'Phase behavior of thin films of cylinder-forming ABA block copolymers: Mesoscale modeling'. In: *J. Chem. Phys.* 120 (2004), pp. 1117–1126.

[35] C. Harrison, D. H. Adamson, Z. Cheng, J. M. Sebastian, S. Sethuraman, D. A. Huse, R. A. Register and P. M. Chaikin. 'Mechanisms of ordering in striped patterns'. In: *Science* 290 (2000), pp. 1558–1560.

[36] D. R. Nelson. *Defects and geometry in condensed matter physics*. Cambridge University Press, Cambridge, 2002.

[37] R. A. Register. 'On the straight and narrow'. In: *Nature* 424 (2003), pp. 378–379.

[38] D. A. Vega and L. R. Gómez. 'Spinodal-assisted nucleation during symmetry-breaking phase transitions'. In: *Phys. Rev. E* 79 (2009), p. 0516707.

[39] C. Harrison, Z. Cheng, S. Sethuraman, D. A. Huse, P. M. Chaikin, D. A. Vega, J. M. Sebastian, R. A. Register and D. H. Adamson. 'Dynamics of pattern coarsening in a two-dimensional semetic system'. In: *Phys. Rev. E.* 66 (2002), pp. 011706–.

[40] E. A. Matsumoto, D. A. Vega, A. D. Pezzutti, N. A. García, P. M. Chaikin and R. A. Register. 'Wrinkles and splay conspire to give positive disclinations negative curvature'. In: *PNAS* 112 (2015), pp. 12639–12644.

[41] D. A. Vega, L. R. Gómez, A. D. Pezzutti, F. Pardo, P. M. Chaikin and R. A. Register. 'Coupling between mean curvature and textures in block copolymer thin films deposited on curved substrates'. In: *Soft Matter* 9 (2013), pp. 9385–9391.

[42] D. E. Angelescu, J. H. Waller, D. H. Adamson, P. Deshpande, S. Y. Chou, R. A. Register and P. M. Chaikin. 'Macroscopic orientiation of block coplolymer cylinders in single-layer films by shearing'. In: *Adv. Mater.* 16 (2004), pp. 1736–1740.

[43] D. E. Angelescu, J. H. Waller, R. A. Register and P. M. Chaikin. 'Shear-induced alignment in thin films of spherical nanodomains'. In: *Adv. Mater.* 17 (2005), pp. 1878–1881.

[44] R. L. Davis, B. T. Michal, P. M. Chaikin and R. A. Register. 'Progression of alignment in thin films of cylinder-forming block copolymers upon shearing'. In: *Macromolecules* 48 (2015), pp. 5339–5347.

[45] K. Amundson, E. Helfand, X. Quan and S. D. Smith. 'Alignment of lamellar block-copolymer microstructure in an electric field: Alignment kinetics'. In: *Macromolecules* 26 (1993), pp. 2698–2703.

[46] T. L. Morkved, M. Lu, A. M. Urbas, E. E. Ehrichs, H. M. Jaeger, P. Mansky and T. P. Russell. 'Local control of microdomain orientation in diblock copolymer thin films with electric fields'. In: *Science* 273 (1996), pp. 931–933.

[47] P. Mansky, J. DeRouchey, T. P. Russell, J. Mays, M. Pitsikalis, T. Morkved and H. Jaeger. 'Large-area domain alignment in block copolymer thin films using electric fields'. In: *Macromolecules* 31 (1998), pp. 4399–4401.

[48] B. C. Berry, A. W. Bosse, J. F. Douglas, R. L. Jones and A. Karim. 'Orientational order in block copolymer films zone annealed below the order-disorder transition temperature'. In: *Nano Lett.* 7.9 (2007), pp. 2789–2794.

[49] K. G. Yager, N. J. Fredin, X. Zhang, B. C. Berry, A. Karim and R. L. Jones. 'Evolution of block-copolymer order through a moving thermal zone'. In: *Soft Matter* 6.1 (2010), pp. 92–99.

[50] C. Bollinne, B. Cuenot S. Nysten and A. M. Jonas. 'Spinodal-like dewetting of thermodynamically-stable thin polymer films'. In: *Eur. Phys. J. E* 12 (2003), pp. 389–396.

[51] S. F. Edwards. 'The statistical mechanics of polymers with excluded volume'. In: *Proc. Phys. Soc.* 85 (1965), pp. 613–624.

[52] E. Helfand. 'Theory of inhomogeneous polymers: Fundamentals of the Gaussian random-walk model'. In: *J. Chem. Phys.* 62 (1975), pp. 999–1005.

[53] E. Helfand. 'Block copolymer theory. III. Statistical mechanics of the microdomain structure'. In: *Macromolecules* 8 (1975), pp. 552–556.

[54] M. W. Matsen. 'Self-consistent field theory and its applications'. In: *G. Gompper, M. Schick (Eds.), Soft Matter* 1 (2006), pp. 87–178.

[55] D. T. Wu, G. H. Fredrickson, J. P. Carton, A. Ajdari and L. Leibler. 'Distribution of chain ends at the surface of a polymer melt: Compensation effects and surface tension'. In: *J. Polym. Sci. Polym. Phys.* 33 (1995), pp. 2373–2389.

[56] T. L. Chantawansri, A. W. Bosse, A. Hexemer, H. D. Ceniceros, C. J. García-Cervera, E. J. Kramer and G. H. Fredrickson. 'Self-consistent field theory simulations of block copolymer assembly on a sphere'. In: *Phys. Rev. E* 75 (2007), pp. 031802–.

[57] M. W. Matsen and M. Schick. 'Stable and unstable phases of diblock copolymer melt'. In: *Phys. Rev. Lett.* 72 (1994), pp. 2660–2663.

[58] M. Müller and F. Schmid. 'Incorporating fluctuations and dynamics in self-consistent field theories for polymer blends'. In: *Advances in Polymer Science* 185 (2005), pp. 1–58.

[59] M. A. Moore. 'Theory of the polymer coil-globule transition'. In: *J. Phys. A: Math. Gen.* 10 (1977), pp. 305–314.

[60] A. N. Semenov. 'Contribution to the theory of microphase layering in block-copolymer melts'. In: *Sov. Phys. JETP* 61 (1985), pp. 733–742.

[61] L. Leibler. 'Theory of microphase separation in block copolymers'. In: *Macromolecules* 13 (1980), pp. 1602–1617.

[62] L. I. Schiff. *Quantum Mechanics*. McGraw-Hill, New York, 1968.

[63] M. W. Matsen. 'Fast and accurate SCFT calculations for periodic block-copolymer morphologies using the spectral method with Anderson mixing'. In: *Eur. Phys. J. E* 30 (2009), pp. 361–369.

[64] P. Stasiak and M. W. Matsen. 'Efficiency of pseudo-spectral algorithms with Anderson mixing for the SCFT of periodic block-copolymer phases'. In: *Eur. Phys. J. E* 34 (2011), pp. 110–118.

[65] W. T. Vetterling B. P. Flannery W. H. Press S. A. Teukolsky. *Numerical Recipes 3rd Edition*. Cambridge University Press, New York, 2007.

[66] F. Schmid and M. Müller. 'Quantitative comparision of self-consistent field theories for polymers near interfaces with Monte Carlo simulations'. In: *Macromolecules* 28 (1995), pp. 8639–8645.

[67] D. G. Anderson. 'Iterative procedures for nonlinear integral equations'. In: *J. Assoc. Comput. Mach* 12 (1965), pp. 547–560.

[68] R. B. Thompson, K. Ø. Rasmussen and T. Lookman. 'Improved convergence in block copolymer self-consistent field theory by Anderson mixing'. In: *J, Chem. Phys.* 120 (2004), pp. 31–34.

[69] H. Kim, S. Park and W. D. Hinsberg. 'Block copolymer based nanostructures: Materials, processes and application to electronics'. In: *Chem. Rev.* 110 (2010), pp. 146–177.

[70] G. Singh, K. G. Yager, B. Berry, H. Kim and A. Karim. 'Dynamic thermal field-induced gradient soft-shear for high oriented block copolymer thin films'. In: *ACS Nano* 6 (2012), pp. 10335–103442.

[71] L. J. Guo. 'Nanoimprint lithography: Methods and material requirements'. In: *Adv. Mater.* 19 (2007), pp. 495–513.

[72] C. Tang, E. M. Lennon, G. H. Fredrickson, E. J. Kramer and C. J. Hawker. 'Evolution of block copolymer lithography to highly ordered square arrays'. In: *Science* 322 (2008), pp. 429–432.

[73] Q. Pike, F. A. Detcheverry, M. Müller and J. J. de Pablo. 'Theoretically informed coarse grain simulations of polymeric systems'. In: *J. Chem. Phys.* 131 (2009), p. 084903.

[74] F. A. Detcheverry, G. Liu, P. F. Nealey and J. J. de Pablo. 'Interpolation in the Directed Assembly of Block Copolymers on Nanopatterned Substrates: Simulation and Experiments'. In: *Macromolecules* 43 (2010), pp. 3446–3454.

[75] S. V. Lishchuk. 'Self-consistent field theory simulation of block copolymer films adsorbed on surfaces of azimuthally symmetric particles'. In: *J. Phys. A; Math. Theor.* 42 (2009), p. 465401.

[76] K. G. A. Tavakkoli, S. M. Nicaise, K. R. Gadelrab, A. Alexander-Katz, C. A. Ross and K. K. Berggren. 'Multilayer block copolymer meshes by orthogonal self-assembly'. In: *Nature Communication* 7 (2016), pp. 10518–10528.

[77] J. N. Israelachvili. *Intermolecular and Surface Forces*. Academic Press, New York, 1992.

[78] A. A. Abate, G. T. Vu, M. Piqueras, L. R. Gómez, M. C. del Barrio, F. Schmid and D. A. Vega. 'Block copolymer thin film instabilities induced by supercritical carbon dioxide'. In: *Preparation* ().

[79] L. Meli, J. Q. Pham, K. P. Johnston and P. F. Green. 'Polystyrene thin films in CO2'. In: *Phys. Rev. E* 69 (2004), pp. 51601–51608.

[80] A. A. Abate, G. T. Vu, A. D. Pezzutti, N. A. García, R. L. Davis, F. Schmid, R. A. Register and D. A. Vega. 'Shear-aligned block copolymer monolayers as seeds to control the orientational order in cylinder-forming block copolymer thin films'. In: *Macromolecules* 49 (2016), pp. 7588–7596.

[81] G. T. Vu, A. A. Abate, L. R. Gómez, A. D. Pezzutti, R. A. Register, D. A. Vega and F. Schmid. 'Curvature as a guiding field for patterns in thin block copolymer films'. In: *Phys. Rev. Lett.* 121 (2018), p. 087801.

[82] A. Knoll, L. Tsarkova and G. Krausch. 'Nanoscaling of microdomain spacings in thin films of cylinder-forming block copolymers'. In: *Nano Letters* 7 (2007), pp. 843–846.

[83] A. Rahman, P. W. Majewski, G. Doerk, C. T. Black and K. G. Yager. 'Non-native three-dimensional block copolymer morphologies'. In: *Nature Communications* 7 (2016), p. 13988.

[84] K. S. Lyakhova, G. J. A. Sevink, A. V. Zvelindovsky, A. Horvat and R. Magerle. 'Role of dissimilar interfaces in thin films of cylinder-forming block copolymers'. In: *J. Chem. Phys.* 120 (2004), pp. 1127–1137.

[85] Y. Yang, Y. J. Choi, S. O. Kim and J. U. Kim. 'Directed self-assembly of cylinder-forming diblock copolymers on sparse chemical patterns'. In: *Soft Matter* 11 (2015), pp. 4496–4506.

[86] Y. Yang, F. Qiu, H. Zhang and Y. Yang. 'Cylindrical phase of diblock copolymers confined in thin films. A real-space self-consistent field theory study'. In: *Polymer* 47 (2006), pp. 2205–2216.

[87] K. G. A. Tavakkoli, K. W. Gotrik, A. F. Hannon, A. Alexander-Katz, C. A. Ross and K. K. Berggren. 'Templating three-dimensional self-assembled structures in bilayer block copolymer films'. In: *Science* 336 (2012), pp. 1294–1298.

[88] L. A. Tsarkova, A. Knoll, G. Krausch and R. Magerle. 'Substrate-induced phase transitions in thin films of cylinder-forming diblock copolymer melts'. In: *Macromolocules* 39 (2006), pp. 3608–3615.

[89] C. T. Black, C. Forrey and K. G. Yager. 'Thickness-dependence of block copolymer coarsening kinetics'. In: *Soft Matter* 13 (2017), pp. 3275–3283.

[90] R. Dimova, U. Seifert, B. Pouligny, S. Förster and H.-G. Döbereiner. 'Hyperviscous diblock copolymer vesicles'. In: *Eur. Phys. J. E* 7 (2002), pp. 241–250.

[91] A. Knoll, K. S. Lyakhova, A. Horvat, G. Krausch, G. J. A. Sevink, A. V. Zvelindovsky and R. Magerle. 'Direct imaging and mesoscale modelling of phase transitions in a nanostructured fluid'. In: *Nature Materials* 3 (2004), pp. 886–891.

[92] M Heckmann and B. Drossel. 'Cylindrical phase of block copolymers in thin films'. In: *Macromolecules* 41 (2008), pp. 7679–7686.

[93] W. Li, M. Liu, F Qui and A.-C. Shi. 'Phase diagram of diblock copolymers confined in thin films'. In: *J. Phys. Chem. B* 117 (2013), pp. 5280–5288.

[94] M. W. Matsen and R. B. Thompson. 'Equilibrium behavior of symmetric ABA triblock copolymer melts'. In: *J. Chem. Phys.* 111 (1999), pp. 7139–7146.

[95] D. A. Hajduk, Takenouchi H., M. A. Hillmyer, F. S. Bates, M. E. Vigild and K. Almdal. 'Stability of the perforated layer (PL) phase in diblock copolymer melts'. In: *Macromolecules* 30 (1997), pp. 3788–3795.

[96] S. Qi and Z.-G. Wang. 'On the nature of the perforated layer phase in undiluted diblock copolymers'. In: *Macromolecules* 30 (1997), pp. 4491–4497.

[97] M. S. Spector, J. V. Selinger, A. Singh, J. M. Rodriguez, R. R. Price and J. M. Schnur. 'Controlling the morphology of chiral lipid tubules'. In: *Langmuir* 14 (1998), pp. 3493–3500.

[98] J. V. Selinger, M. S. Spector and J. M. Schnur. 'Theory of self-assembled tubules and helical ribbons'. In: *J. Phys. Chem. B* 105 (2001), pp. 7157–7169.

[99] W. Helfrich. 'Elastic properties of lipid bilayers: Theory and possible experiments'. In: *Z. Naturforsch.* 28C (1973), pp. 693–703.

[100] P. B. Canham. 'The minimum energy of bending as a possible explanation of the biconcave shape of the human red blood cell'. In: *Journal of Theoretical Biology* 26 (1970), pp. 61–81.

[101] S. A. Safran and T. Tlusty. 'Curvature elasticity models of microemulsions'. In: *Ber. Bunsenges. Phys. Chem.* 100 (1996), pp. 252–263.

[102] D. C. Morse. 'Entropy and fluctuations of monolayers, membranes, and microemulsions'. In: *Cur. Opin. Colloid Interface Sci.* 2 (1997), pp. 365–372.

[103] G. Gompper and D. M. Kroll. 'Membranes with fluctuating topology: Monte Carlo simulations'. In: *Phys. Rev. Lett.* 81 (1998), pp. 2284–2287.

[104] T. Powers and P. Nelson. 'Fluctuating membranes with tilt order'. In: *J. Phys. II* 5 (1995), pp. 1671–1678.

[105] P. Biscari and E. M. Terentjev. 'Nematic membranes: Shape instabilities of closed achiral vesicles'. In: *Phys. Rev. E* 73 (2006), pp. 0517061–0517066.

[106] R. Oda, I. Huc, M. Schmutz, S. J. Candau and F. C. MacKintosh. 'Tuning bilayer twist using chiral counterions'. In: *Nature* 399 (1999), pp. 566–569.

[107] C.-M Chen. 'Theory for the bending anisotropy of lipid membranes and tubule formation'. In: *Phys. Rev. E* 59 (1999), pp. 6192–6195.

[108] M. J. Fasolka, P. Banerjee, A. M. Mayes, G. Pickett and A. C. Balazs. 'Morphology of ultrathin supported diblock copolymer films: theory and experiment'. In: *Macromolecules* 33 (2000), pp. 5702–5712.

[109] M. J. Fasolka and A. M. Mayes. 'Block copolymer thin films: Physics and applications'. In: *Annu. Rev. Mater. Res.* 31 (2001), pp. 323–355.

[110] C. D. Santangelo, V. Vitelli, R. D. Kamien and D. R. Nelson. 'Geometric theory of columnar phases on curved substrates'. In: *Phys. Rev. Lett.* 99 (2007), pp. 017801–.

[111] G. Napoli and L. Vergori. 'Extrinsic curvature effects on nematic shells'. In: *Phys. Rev. Lett.* 108 (2012), pp. 207803–.

[112] K. Aissou, J. Shaver, G. Fleury, G. Pécastaings, C. Brochon, C. Navarro, S. Grauby, J.-M. Rampnoux, S. Dilhaire and G. Hadziioannou. 'Nanoscale block copolymer ordering induced by visible interferometric micropatterning: A route towards large scale block copolymer 2D crystals'. In: *Adv. Mater.* 25 (2013), pp. 213–217.

[113] X. Man, P. Zhou, J. Tang, D. Yan and D. Andelman. 'Defect-free perpendicular diblock copolymer films: The synergy effect of surface topography and chemistry'. In: *Macromolecules* 49 (2016), pp. 8241–8248.

[114] S. Park and L. A. Tsarkova. 'Surface roughness-mediated ordering in block copolymer films toward spatially controlled patterns'. In: *Macromolecules* 50 (2017), pp. 6840–6848.

[115] F. Drolet and G. H. Fredrickson. 'Optimizing chain bridging in complex block copolymers'. In: *Macromolecules* 34 (2001), pp. 5317–5324.

[116] C. M. Bates and F. S. Bates. '50th Anniversary perspective: Block polymers - pure potential'. In: *Macromolecules* 50 (2017), pp. 3–22.

[117] B. Vorselaars, J. U. Kim, G. H. Chantawansri T. L. Fredrickson and M. W. Matsen. 'Self-consistent field theory for diblock copolymers grafted to a sphere'. In: *Soft Matter* 7 (2011), pp. 5128–5137.

[118] J. G. E. M. Fraaije, B. A. C. van Vlimmeren, N. M. Maurits, M. Postma, O. A. Evers, P. Hoffmann C. Altevogt and G. Goldbeck-Wood. 'The dynamic mean-field density functional method and its application to mesoscopic dynamics of quenched block copolymer melts'. In: *J. Chem. Phys.* 106 (1997), pp. 4260–4269.